DISTRIBUTED MIMO RADAR SIGNAL PROCESSING

A THESIS SUBMITTED TO

THE GRADUATE SCHOOL OF ENGINEERING AND SCIENCE

OF BILKENT UNIVERSITY

IN PARTIAL FULFILLMENT OF THE REQUIREMENTS FOR

THE DEGREE OF

MASTER OF SCIENCE

IN

ELECTRICAL AND ELECTRONICS ENGINEERING

By

Mahmut Kemal Ercan

July 2022

DISTRIBUTED MIMO RADAR SIGNAL PROCESSING
By Mahmut Kemal Ercan
July 2022

We certify that we have read this thesis and that in our opinion it is fully adequate, in scope and in quality, as a thesis for the degree of Master of Science.

Orhan Arıkan (Advisor)

Sinan Gezici (Co-Advisor)

Vakur Behçet Ertürk

Ali Özgür Yılmaz

Approved for the Graduate School of Engineering and Science:

Orhan Arıkan
Director of the Graduate School

ABSTRACT

DISTRIBUTED MIMO RADAR SIGNAL PROCESSING

Mahmut Kemal Ercan
M.S. in Electrical and Electronics Engineering
Advisor: Orhan Arıkan
Co-Advisor: Sinan Gezici
July 2022

Radar systems are remote sensing tools that generate electromagnetic waves and extract information by receiving altered versions of these waves. Nowadays, many radar types are being used in specific areas such as weather prediction, automobiles, and the military. One type of radar employed in military applications is called the multistatic radar system. Multistatic radar systems consist of multiple transmitters and receivers widely separated from each other. Although multistatic radar systems have not been invented recently, one type of multistatic radar has recently taken the attention of the literature, the multiple input multiple output (MIMO) radar system. In this thesis, we analyze the performance of some techniques presented in the MIMO radar literature, make improvements, and propose new methods.

First, we review the literature for MIMO radar waveform generation. Then, we propose a parameter estimation technique for multiple target cases using the polyphased-piecewise linear frequency modulated (PPLFM) waveform. Secondly, we propose a detection algorithm in which each receiver preprocesses received signals and extracts bistatic range and Doppler for each transmitter. A grid of points in the region of interest (ROI) is generated, and by using a weighting function, a weight for each plot is calculated, and detection is performed via thresholding. Third, we propose a policy-iteration-based position and velocity estimation algorithm. We define a cost function using bistatic range and Doppler measurements for the proposed estimation algorithm. To perform estimation in the presence of multiple targets, we conduct data association by weighting the bistatic measurements. Fourth, a tracking algorithm that uses the Generalized Multi Bernoulli Filter is proposed. Lastly, we investigate the alternative MIMO antenna structures and analyze the detection and tracking performance of the Electromagnetic

Vector Sensor (EMVS). At the end of the thesis, it is demonstrated that the performance of the proposed algorithms is promising. Additionally, we show that the detection and tracking performance of the EMVS-based MIMO radar system is better than the performance of the MIMO radar system with dipole antennas.

Keywords: Multistatic radar, MIMO radar, detection, estimation.

ÖZET

AYRIK KONUŞLANDIRILMIŞ ÇGÇÇ RADAR SİNYAL İŞLEME

Mahmut Kemal Ercan
Elektrik ve Elektronik Mühendisliği, Yüksek Lisans
Tez Danışmanı: Orhan Arıkan
İkinci Tez Danışmanı: Sinan Gezici
Temmuz 2022

Radar sistemleri, elektromanyetik dalgalar üreten ve bu dalgaların değişmiş hallerini alarak bilgi çıkaran uzaktan algılama araçlarıdır. Günümüzde hava tahmini, otomobiller ve askeriye gibi belirli alanlarda birçok radar türü kullanılmaktadır. Askeri uygulamalarda kullanılan bir radar türü, multistatik radar sistemi olarak adlandırılır. Multistatik radar sistemleri, birbirinden geniş ölçüde ayrılmış birden fazla verici ve alıcıdan oluşur. Multistatik radar sistemleri son zamanlarda icat edilmemiş olsa da bir tür multistatik radar olan çoklu girdi çoklu çıktı (ÇGÇÇ) radar sistemleri son zamanlarda literatürün dikkatini çekmiştir. Bu tezde literatürde yer alan bazı tekniklerin performansları analiz edilerek iyileştirmeler yapılmış ve yeni yöntemler önerilmiştir.

İlk olarak, ÇGÇÇ radar dalga formu üretimi için literatürü incelenmiştir. Daha sonra, çokevreli parçalı doğrusal frekans modülasyonlu (ÇPDFM) dalga formunu kullanarak çoklu hedef durumlar için bir parametre tahmin tekniği önermekteyiz. İkinci olarak, hedef tespiti için her alıcının alınan sinyalleri önceden işlediği ve her verici için bistatic menzil ve Doppler bilgisini çıkardığı bir algoritma önermekteyiz. İlgili bölgede bir noktalar ızgarası oluşturulur ve bir ağırlıklandırma işlevi kullanılarak her bir çizim için bir ağırlık hesaplanır ve tespit, eşikleme ile gerçekleştirilir. Üçüncü olarak, politika yineleme tabanlı bir konum ve hız tahmin algoritması önermekteyiz. Önerilen tahmin algoritması için bistatik aralığı ve Doppler ölçümünü kullanarak bir maliyet fonksiyonu tanımlıdık. Tahmini birden fazla hedefin varlığında gerçekleştirmek için, bistatik ölçümleri ağırlıklandırarak veri ilişkilendirmesi yapan bir teknik önermekteyiz.

Dördüncüsü, Genelleştirilmiş Çoklu Bernoulli Filtresini kullanan bir izleme algoritması önermekteyiz. Son olarak, alternatif ÇGÇÇ anten yapılarını incelemekteyiz ve Elektromanyetik Vektör Sensörünün (EMVS) algılama ve izleme performansını analiz etmekteyiz. Tezin sonunda, önerilen algoritmaların performansının umut verici olduğu gösterilmiştir. Ayrıca, EMVS tabanlı ÇGÇÇ radar sisteminin algılama ve izleme performansının, dipol antenli ÇGÇÇ radar sisteminin performansından daha iyi olduğu gösterilmektedir.

Anahtar sözcükler: Multistatik radar, ÇGÇÇ radar, sezim, kestirim.

Acknowledgement

First, I would like to express my gratitude to my advisor Prof. Orhan Arikan for his guidance. He was always available for me whenever I wanted to meet and never turn me back even if I was asking too many questions. I also want to thank my co-advisor, Prof. Sinan Gezici. Even though we could not meet very frequently, I thank him for the support and fatherhood he has given me.

I also want to thank to my friends Ufkun, Yavuz, Kadir, Taner abi, Mustafa, Mert (a.k.a Haşin), Çağlar, Salih, Osman, Şeker, Cüneyd, Fatih, and all of my friends whose names I can't even mention. Thank you for being there for me in my good and bad days. Each one of you is like a brother to me.

Finally, I would like to express my deepest gratitude to my mom, my dad, and my lovely sister *Şükran*. I want to thank my mom, who was awake until late-night every day, for helping me with my homework when I was a child. Thank you for your endless love and patience. My dad is a great father who has always encouraged me to pursue my dream of becoming an engineer. Thank you for letting me live my life as I want in the best way. My sister, who past away so early, I will never forget the times we have been together. Even in the corridors of the hospital, the echoes of your laughter are still in my head. I will miss you so much.

To my beloved sister *Şükran*

Contents

List of Figures

List of Tables

List of Abbreviations

AF Ambiguity Function. xxii

AWGN Additive White Gaussian Noise. xxii

CPHD Cardinalized Probability Hypothesis Density. xxii

CRB Cramer-Rao Bound. xxii

CW Continuous Waveform. xxii

DOA Direction-of-Arrival. xxii

DOD Direction-of-Departure. xxii

EMVA Electromagnetic Vector Antenna. xxii

EMVS Electromagnetic Vector Sensor. xxii

GLMB Generalized Labelled Multi-Bernoulli. xxii

LFM Linear Frequency Modulation. xxii

LMB Labeled Multi-Bernoulli. xxii

MIMO multiple-input and multiple-output. xxii

MLFMA Multi Level Multi Fast Multipole Algorithm. xxii

MS Multistatic. xxii

MSE Mean Square Error. xxii

PHD Probability Hypothesis Density. xxii

PLFM Piecewise Linear Frequency Modulation. xxii

PPLFM Polyphase-coded Piecewise Linear Frequency Modulation. xxii

PRF Pulse Repetition Frequency. xxii

RCS Radar Cross Section. xxii

RFS Random Finite Set. xxii

ROI Region of Interest. xxii

RPA Receive Polarization Angle. xxii

SIAR Synthetic Impulse and Aperture Radar. xxii

SNR Signal to Noise Ratio. xxii

TPA Transmit Polarization Angle. xxii

ULA Uniform Linear Array. xxii

XMF Extended Matched Filter. xxii

Chapter 1

Introduction

In monostatic radar systems, the transmitter and receiver are colocated, and most of the time, use the same antenna. The structure is relatively simple compared to other radar systems. However, considering today's technology, most of the military targets are designed to have low monostatic radar cross section (visibility). For example, a recently developed F35 aircraft has less monostatic radar visibility than a bird. The low monostatic radar visibility is the result of scattering the reflecting signals away from the angle of incidence so that the back-scattered power is reduced. To detect and track targets with low visibility, the radar systems have large and active antennas, highly complex signal processing algorithms, high peak power transmitter. To detect targets with low back scattering, the transmitter and the receiver should not be colocated. Such radar systems are called bistatic radar systems. To increase the performance of the bistatic radar systems, multistatic radar systems can be used.

Multistatic radar systems are radar systems that are placed in at least three different locations. The selection of these locations should be performed to provide a large baseline for the targets in detection zone. When the radars' positions are so far apart to create a quasi-different bistatic angle on the target, the scatter signals reaching the receivers become discordant. In other words, the signal power decreases considerably. Therefore, coherent signal processing is not possible among the receivers. Important details on this subject can be found in Chapter 11 of [3]. When the multistatic radar system combines the obtained detections incoherently, the SNR level increase is lower than that obtained via the coherent integration. The expected SNR gain in incoherent integration is investigated in detail in the literature [4], [5], [6].

Multistatic radar systems can be composed of transmitter and receiver units consisting of phased array antennas with beam scanning capability or network radar systems, each of which uses a phased array antenna. Radar systems in this second alternative structure can detect and track the target by capturing the target scattering signals originating from the signals emitted by other radars in the network and transmit the relevant information to the control center beyond the monostatic detection and target tracking information they produce. Within the scope of this thesis, we will name these systems as multistatic monostatic radar systems, in short, MS-MS radar systems.

Radar units in MS-MS radar systems have two basic functions. The first one is that MS-MS radar systems must provide all the requirements of monostatic networked radar systems. Monostatic radars in the network structure should be able to detect and track targets using the signals they send and share the detection and tracking information they produce with the control center. In addition, they should be able to track common targets and target handover by using the information from the control center. The second one is that they must be able to work with other radars in the network as a bistatic radar system. This requirement requires a capability beyond the capability of the receiver units in bistatic radar systems. In bistatic radar systems, the receiver only tries to catch the pulses emitted in the beam of a transmitter. Radars in MS-MS radar systems must be capable of catching pulses emitted from the beams of all other radars. If there are N radars in the MS-MS system, each radar should be designed to capture pulses in the other (N-1) radar beams. This situation requires that each radar has at least N receiver stages and signal processing units.

A considerable problem of MS-MS radar systems is that as the number of radars in the network increases, the required hardware load can reach unacceptable levels. The reason is that each receiver must arrange its beam pattern and try to catch any reflected signal of any transmitter from a target. For this reason, instead of chasing pulses on the beams of all other radar systems in the network, the radars in the MS-MS radar systems perform pulse chasing on the beams at which the probability of detection and tracking is high. This arrangement can be made by considering the radars' positions and the current beams' directions. This arrangement provides a significant hardware gain. A receiver chasing the pulse of a transmitter is shown in Fig. 1.1.

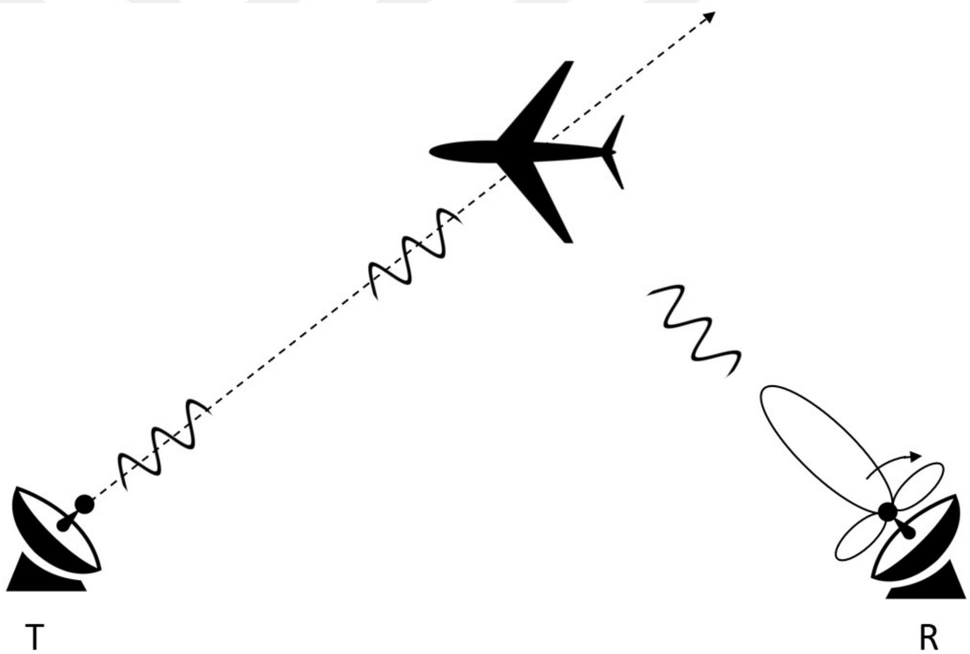

Figure 1.1: In a multistatic radar system that uses narrowbeam transmitters, receiver should use pulse chasing to receive echos of potential targets in the direction of the transmitter beam.

Radars in the MS-MS radar system typically scan with agile beams by keeping their phased array antennas in a fixed position to perform pulse chasing to the beams of other radars. When MS-MS radar systems operate with stationary antennas, they can only, in some cases, track a subset of beams produced by other radars. The MS-MS control center has to decide which radars to perform pulse tracking on each beam generated. This decision is transmitted to the relevant radars, and it is crucial for the success of the system to ensure that the necessary action is taken on time. When the radars in the MS-MS radar system direct their active beams as if they were pseudo-random, it becomes challenging to confuse the MS-MS system. This feature is among the essential benefits of MS-MS radar systems. Therefore, MS-MS systems are very complex, and the monostatic properties do not adequately provide an advantage. For that reason, a less complex multistatic radar system can be used, MIMO radar systems.

Multiple Input Multiple Output or simply MIMO radar is a relatively new technique among multistatic radar systems. MIMO radar systems consist of several transmitters and receivers. Each transmitter generates an orthogonal signal to the other transmitters, and each receiver collects and distinguishes each signal. There are two types of MIMO radar systems. These are the MIMO radar systems with colocated antennas and MIMO radar systems with widely separated antennas. MIMO radar with colocated antennas is similar to phased array radar. The only difference is that in MIMO radar, transmitted waveforms of each antenna element are uncorrelated, while in phased array antenna, transmitted waveforms are highly correlated. MIMO radar with colocated antennas is usually used instead of phased array radar to increase angular resolution and parameter estimation performance, [7, 8, 9, 10]. Also, it provides flexibility for beampattern design [11].

MIMO radars with widely separated antennas consist of geographically distributed transmitters and receivers structure like other multistatic radar systems. The developments on MIMO radars with the transmitters and receivers being positioned far from each other are presented in [12]. MIMO radars can use angularly varying RCS of the targets by combining the results of the noncoherently processed signals and provide spatial diversity gain in target detection, target position and Doppler velocity estimation stages. It is observed from RCS analysis of stealth fighter jets in [13] that scattering from radar targets typically has an angular variation of -10 dBsm to 45 dBsm, and can vary significantly even at small changes of angles [14]. The angular scattering observed from such targets causes independent directionally independent signals to be received. In other words, the ratio of the correlation of the scattering signals obtained at two different angles to the geometric average of the energies of the signals is around zero. MIMO radar systems are principally designed to increase performance using this variation in target scatter. From that point, MIMO radar with widely separated antennas will be referred as MIMO radar.

MIMO radar systems consist of active transmitters and passive receivers. In multistatic radar systems consisting of active radars, each radar system transmits its detection data to a central processing unit, and the data collected in this center are processed and final decisions are made [15, 16, 17, 18].

The presence of a large number of transmitters in MIMO radar systems provides an important degree of freedom compared to single transmitter systems [19] since the maximum degrees of freedom of a Distributed MIMO radar system is the number of bistatic pairs, which is the number of transmitters times the number of receivers. Using this increase in degrees of freedom, flexible time-energy resource utilization modes [20], better angular resolution [21, 22], and better parameter estimation can be made [23]. MIMO systems with long-spaced antennas improve the performance of the radar using angular variation of RCS [23] and improve the detection performance and spatial resolution of slow targets by observing targets from various directions [24]. Studies on the selection of receiver and transmitter locations in MIMO radar systems are available in the literature [15, 25].

In the literature of MIMO radar systems, waveforms that are designed for MIMO radar systems are commonly studied for stationary target case (in zero Doppler environment) [26, 27, 28, 29], they are designed as Doppler fragile for which signal processing schemes are highly complex [30, 31]. Doppler fragile waveforms are sensitive to Doppler effect. In other words, the output power of the matched filter decreases considerably in the presense of Doppler. Hence, a matched filtering must be performed for each Doppler bin in order to receive proper signal from the corresponding delay and Doppler, which creates highly computational complexity.

Additionally, most of the waveforms are designed for MIMO radar systems with colocated antennas. As a result, the papers study their design in range-angle domain [32, 33]. On the other hand, there are some studies on Doppler-tolerant waveform designs for MIMO radar applications [34, 35]. However, the number of targets is assumed to be one in these works. As a result, the Doppler-tolerant waveforms must be also designed for multiple target case.

The target detection in MIMO radar sytems is the main focus of the literature [12, 36, 23, 37]. However, systems that are designed in the literature are most commonly focus on spatial integration of the signal. In other words, instead of matched filtering for range bins, the system creates a grid of points and performs matched filtering for the delay corresponding to that grid point. This brings high computational complexity. As a result, the computational complexity should be reduced in order to be used in real-life applications.

The target localization in MIMO radar system is a hot topic in the literature. In [38, 39, 40, 41, 42], the localization is performed by bistatic range measurements that are modelled with zero-mean Gaussian error. However, in practice, the range measurements are obtained in range bins. Hence, a suitable model for real-life applications could be to add quantization error to the bistatic range measurements instead of zero mean Gaussian error.

An important feature of a radar system is the tracking performance. In literature, target trackers based on Joint Probabilistic Data Association [43], Multiple Hypotheses Tracking [44], and Random Finite Set [45, 46] are examples of multiple target trackers with multiple sensors. Along with these, the target trackers for MIMO radar systems that use PHD [47] and Bernoulli filter [48], are available in the literature.

In this thesis, we extend the MIMO radar design concepts that are presented in [34, 35] for multiple target case. The system performs data association to ignore the ghost targets. For target detection, we use these plots. In other words, instead of applying matched filter for each grid point, we perform matched filter once and create plot for corresponding range bin. After obtaining bistatic ranges for each bistatic pair, we perform detection by integrating this information. For target position and velocity estimation, we have designed a policy-iteration-based novel position and velocity estimation method. The technique depends on minimizing a cost function which we define as the difference between bistatic range and Doppler measurements and the resulting values for the position and velocity estimation. We also study multiple target case by developing a technique for data association. The data association is performed by calculating and thresholding a weight value that changes according to the bistatic range difference between the initial estimation point and measurement. Additionally, we model the bistatic range measurement error as quantization error to have more realistic results.

The organization of the thesis is as follows: Chapter 2 gives the theoretical background of bistatic and multistatic radar systems. In chapter 3, literature review is made and the current problems and solutions on MIMO radar systems in the literature are given. In chapter 4, we have proposed several novel techniques to be used in a MIMO radar system. In chapter 5, the simulation results of the proposed methods are given and effects of the parameters and limitations are analyzed. Finally, the contribution of this thesis to the literature is concluded in chapter 6.

Chapter 2

Bistatic Radar and Multistatic Radar Systems

2.1 Introduction

In this chapter, we explain the concept of bistatic radar systems and present the geometry of bistatic radar systems. After that, we review the current technology and limitations encountered in multistatic radar systems.

In Section 2.2, we review the concept of bistatic radar, in particular, the advantages and disadvantages of a bistatic radar system. In Section 2.3, the geometry of bistatic radar is studied, which reviews and defines the fundamental parameters of bistatic radar.

Section 2.3 consists of four subsections. In Section 2.3.1, we define the bistatic range, which is the summation of the range between transmitter and target and the range between the target and receiver. A bistatic range creates an ellipse where the bistatic range of any point on that ellipse equals the specified bistatic range. Additionally, we derive the transmitter and receiver ranges using the bistatic range and receiver angle. In section 2.3.2, we define bistatic Doppler, which is related to the summation of the target's relative speed to the transmitter and the receiver. In Section 2.3.3, the bistatic range resolution is defined as the area between the bistatic ellipses between two specified ranges. In Section 2.3.4, we present the definition of bistatic Doppler resolution. We also discuss the parameters affecting the bistatic Doppler resolution.

In Section 2.4, we discuss a method to detect a target in bistatic radar systems with a narrow receiver beam called pulse chasing. This technique aims to receive the reflection from any target in the direction of the transmitted pulse. The advantages and difficulties of this technique is discussed. Finally, we review multistatic radar systems in Section 2.5. The challenges of performing pulse chasing in a multistatic radar system is discussed.

2.2 Bistatic Radar Systems

In monostatic radar systems, the receiver and transmitter are in the same position and typically use the same antenna. On the other hand, bistatic radar system consists of a transmitter (T) and a receiver (R) placed at a distance from each other. In the two-dimensional structure shown in Fig. 2.1, the target's range and lateral angle can be easily matched with a radar-centered polar coordinate system for monostatic radar. In the bistatic case, an elliptical system must be used.

Bistatic radar systems have two important basic geometric characteristics, [1]. The first one is the distance between receiver and transmitter, and the second one is transmitter, target, and receiver triangulation. Although the distance between transmitter and receiver is typically constant, there are also applications where it varies. However, the target position typically changes during the triangulation. This variation can be followed by the bistatic angle difference $\frac{|\theta_t-\theta_r|}{2}$ or the change of the triangulation factor, which is also known as F factor:

$$F = \cos\left(\frac{|\theta_t - \theta_r|}{2}\right) . \tag{2.1}$$

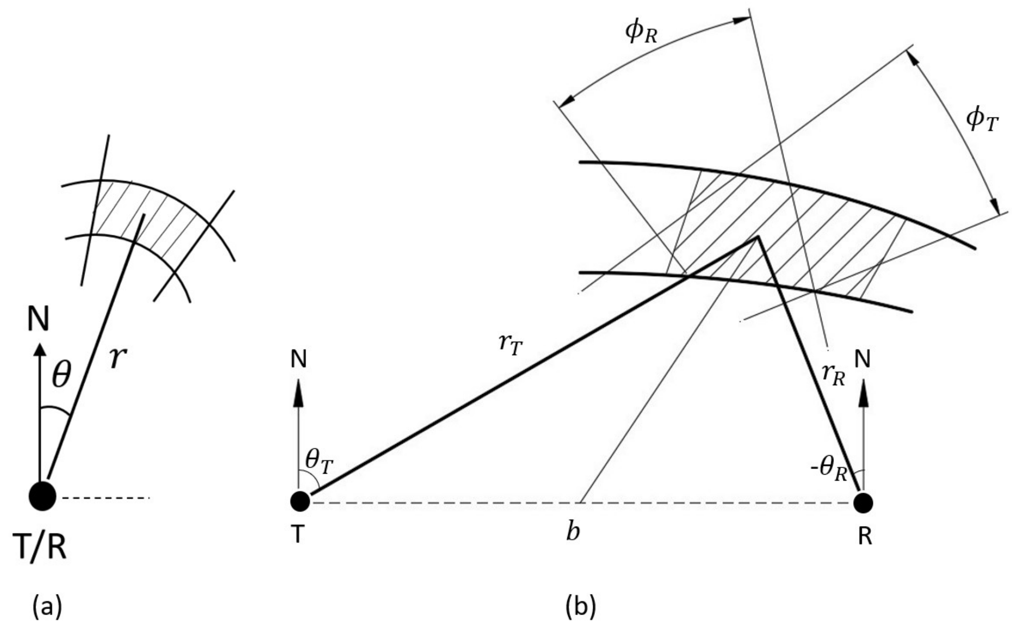

Figure 2.1: (a) the polar system for a given Monostatic radar, and (b) elliptical system for a given bistatic radar, [1]

The values of the F factor indicate three different target regions [1]:

1. $0.1 \leq F \leq 0.9$: Defines the broadside region. Within this zone, the basic characteristics of the bistatic radar apply. It is the region where it is possible to detect the targets from the signals emitted by the targets with reduced RCS.

2. $F < 0.1$: Defines the baseline region. This area is the area between the transmitter and receiver antennas. It is the region where range and Doppler resolution is less and where there is direct signal interference. Although the highest target scatter signal is received in this region, target detection becomes difficult under direct signal mixture.

3. $0.9 < F$: Defines the lateral region. An approximately monostatic radar-like situation prevails in this region. Back-scattering from the targets is effective and it is the region where targets with reduced RCS are difficult to detect.

There are many advantages of bistatic radar systems over monostatic radar systems. These advantages are mainly owing to the separation of transmitter and receiver and triangulation, [1]. By separation of transmitter and receiver, it is possible to use continuous waveform (CW). In this way, range requirements can be met by using signals with less power. Since there is no change of duties between the transmitter and receiver, the need for switching between transmitter and receiver is eliminated. Transmitter and receiver antennas can be designed according to different criteria and produced independently. The requirements for the suppression of clutter is less restrictive. The dynamic range of the signal is narrower. Portability is more possible with the use of moving receivers. Safer operation is possible because the locations of the receivers that do not emit energy cannot be determined easily.

Besides, there are advantages achieved from triangulation. Distance and angle resolution can be increased by using spatial and temporal filtering. The flexibility in the radar waveforms and other parameters increases the performance the radar can reach. Owing to high pulse repetition frequency (PRF) without creating range ambiguity, the detection performance of moving targets can be increased in the presence of clutter by increasing the unambiguous Doppler. The signals from the side lobe can be suppressed by using different side lobe structures in the transmitter and receiver. The effect of a powerful, unidirectional jammer with pulse imitation property at a long distance can be significantly reduced at the receiver.

Even though bistatic and multistatic radar systems has advantages over monostatic radar systems, there are some difficulties of multistatic radar systems. Some difficulties arise as a result of separation of the transmitter and receiver. First difficulty is time synchronization of transmitter and receiver. When the transmitter operates in which operational mode, when and at what frequency it broadcasts, and the phase of the signals it sends must be shared. Second, transmitter and receiver must know the location of each other, and receiver must know the angle of view of the transmitter. Third, The resolution cell and PRF are affected. PRF is required to be chosen such that only one pulse passes through the area scanned by the receiver during the pulse chasing. Lastly, both sides should have the necessary logistical and operational support.

Additionally, triangulation created some difficulties as well. For example, The decrease in the ratio between the power of the reflection from a target, and clutter and the noise signal can be faced. Similarly, false alarms can be caused by the intersection of the main beams and side lobes and the decrease in performance in detection, positioning, and Doppler velocity estimation due to the low Doppler resolution in the area between the antennas. Choosing the locations of transmitter and receiver is also critical. As shown in Fig. 2.1, the size of the radar cell vary according to the position of the target and the performance of the radar is affected accordingly. Reduced coverage area. Typically the expected 360° coverage area is not reached. Observing a decrease in RCS on average. Increased probability of terrain masking when observing low flying targets. The intersections of the transmitter and receiver beams requires pulse chasing. During three dimensional coverage, very difficult beam control is required. The required synchronized operation reduces the flexibility of the operational modes. Increasing complexity of hardware required to process the signals provided by the beams of the receiver.

The most critical difficulty is the decrease in RCS on average. In order to overcome this problem, many bistatic receivers must be used. This means that to have a good performance on total, multistatic radar systems are appealing. To understand the advantages and difficulties explained above, bistatic radar geometry should be examined.

2.3 Geometry of Bistatic Radar

Since the transmitter and receiver are separated, the geometry has two centers. This creates an elliptical structure at which the focuses are the positions of transmitter and receiver.

2.3.1 Bistatic Range

In bistatic radar systems, the iso-delay curves for the signal coming from the target, that is, the curves where the delay created by the target does not change when the target is moved, are ellipses whose focus is on the transmitter and receiver. These ellipses are the result of the triangulation. The bistatic range is the summation of the distance from transmitter to target, and from target to receiver, which will be denoted as ρ. This summation formula is also called as equation of triangulation:

$$\rho = r_t + r_r \tag{2.2}$$

The effective one-way delay on these curves is $(r_t + r_r)/2c$, that is, the arithmetic average of the delays to the foci. In the 3D case, the co-lag surfaces are ellipsoids with the same foci. However, for an isotropic target, the isotropic curves are those in which the $1/(r_t^2 r_r^2)$ does not change. The effective unidirectional power distance on these curves is $\sqrt{r_t r_r}$, that is, the geometric mean of the distance to the foci. Isometric curves are called Cassini ovals.

As shown in Fig. 2.1, The range of target to transmitter can be calculated using the Pythagoras theorem for all triangles, [49]:

$$r_t^2 = r_r^2 + b^2 + 2r_r b \cos(\phi_r). \tag{2.3}$$

By using the equation of triangulation, The range of target for receiver and transmitter can be derived. First, let us derive the equation for distance between the receiver and the target. From (2.3):

$$(\rho - r_R)^2 = r_R^2 + b^2 + 2r_R b \cos(\phi_R),$$

$$\rho^2 - 2\rho r_R + r_R^2 = r_R^2 + b^2 + 2r_R b \cos(\phi_R),$$

$$\rho^2 - 2\rho r_R = b^2 + 2r_R b \cos(\phi_R),$$

$$\rho^2 - b^2 = 2\rho r_R + 2r_R b \cos(\phi_R),$$

Putting the things multiplied with $2r_R$ in parenthesis

$$\rho^2 - b^2 = 2r_R(\rho + b\cos(\phi_R)),$$

$$2r_R = \frac{\rho^2 - b^2}{\rho + b\cos(\phi_R)},$$

The resulting equation for r_R is given as

$$r_R = \frac{\rho^2 - b^2}{2(\rho + b\cos\phi_R)}, \tag{2.4}$$

The range between the transmitter and the target can be calculated similarly:

$$r_T^2 = (\rho - r_T)^2 + b^2 + 2(\rho - r_T)b\cos(\phi_R),$$

$$r_T^2 = \rho^2 - 2\rho r_T + r_T^2 + b^2 + 2\rho b\cos(\phi_R) + 2r_T b\cos(\phi_R),$$

$$2\rho r_T + 2r_T b\cos(\phi_R) = \rho^2 + b^2 + 2\rho b\cos(\phi_R),$$

$$2r_T(\rho + 2b\cos(\phi_R)) = \rho^2 + b^2 + 2\rho b\cos(\phi_R),$$

$$r_T = \frac{\rho^2 + b^2 + 2\rho b\cos\phi_R}{2(\rho + b\cos\phi_R)}. \tag{2.5}$$

As it is seen, the range of target for transmitter and the receiver can be determined only by bistatic range, base distance, and the receiver angle. Note that these formulas can be derived for the transmitter angle. However, we focus on the cases where the performance of the receiver.

2.3.2 Bistatic Doppler

The Doppler is a function of triangulation function and is the projection to the unit vector directed perpendicular to the ellipse, [1]:

$$f_d = f_0 D\cos\delta, \tag{2.6}$$

where $f_0 = 2v/\lambda$ is the maximum Doppler shift created by the velocity of the target, v, the wavelength of the transmitted waveform, λ, the angular difference between the velocity direction ψ and the direction perpendicular to the iso-bistatic range, which is called Doppler velocity angle, $\delta = \psi - \frac{\theta_t+\theta_r}{2}$, and the loss factor $D = \sqrt{(1-F^2)}$.

Note that both loss factor and Doppler velocity angle are defined by the transmitter and receiver angles. The reason for this is that the bistatic Doppler is actually the summation of Doppler effect for the transmitter and the receiver. Considering this, for example, for the loss factor, Doppler is equal to zero when the target is between the transmitter and receiver. The reason for this is that the Doppler for the transmitter is minus the Doppler for the receiver. Hence, when these Dopplers are summed, the result, which is bistatic Doppler, becomes zero.

Additionally, Doppler velocity angle is another criteria which affects the bistatic Doppler. The bistatic Doppler is the summation of the target's relative speed to the transmitter and the receiver. In other words, bistatic Doppler can also be considered as the derivative of the bistatic range:

$$f_d = -\frac{1}{\lambda}\frac{d}{dt}(r_T + r_R)$$

Interpreting this formula, iso-Doppler lines becomes perpendicular lines to bistatic range ellipsoids which are hyperboles. Doppler velocity angle is the angular difference between the direction of the target and the hyperbole that the target is on. If the direction of the target is the same direction with the hyperbole, the Doppler is maximized.

2.3.3 Bistatic Range Resolution

As shown in Fig. 2.2, bistatic range resolution can be defined as the minimum distance between two points on two ellipses, [49]:

$$\Delta\rho = \frac{c}{2B_w \cos(\beta/2)}. \tag{2.7}$$

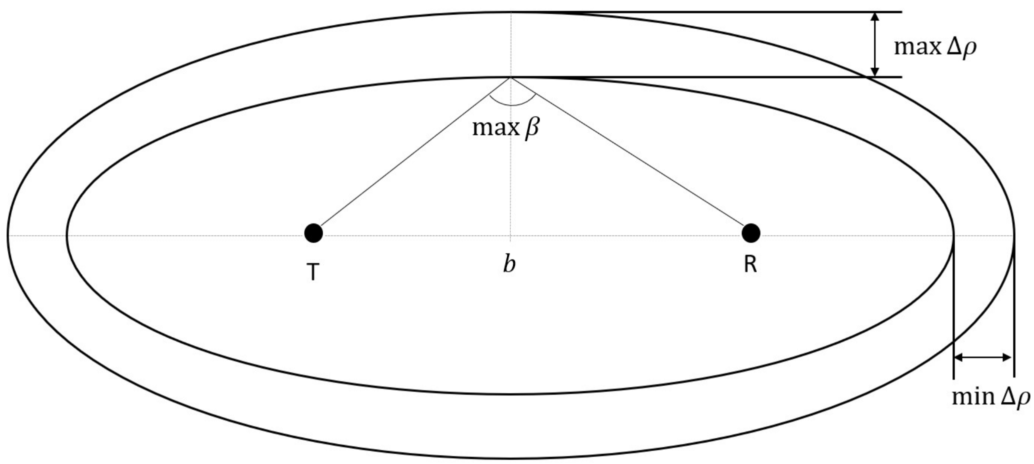

Figure 2.2: Maximum and minimum range window for bistatic range resolution $\Delta\rho$ and maximum value of β on a given scenario.

In this equation, c is the velocity of light and B_w is the bandwidth of the transmitted signal. Apart from this definition, bistatic range resolution can also be defined as the area that has been determined by the beamwidth of the radars, ϕ_t, ϕ_r, and the pulse length, $\Delta\rho = \frac{c}{B_w}$, [1]:

$$A = \frac{\Delta\rho}{2D}\frac{\rho\phi_e}{2D}, \tag{2.8}$$

where $\phi_e = \frac{1}{\sqrt{\left(\frac{\rho}{8r_t\phi_t}\right)^2 + \left(\frac{\rho}{8r_r\phi_r}\right)^2}}$

Considering this definition, it is seen that the bistatic range resolution is directly proportional to the bistatic range and inversely proportional to the loss factor. To examine the effect of bistatic range on bistatic range resolution, assume that a bistatic range ellipsoid is created close to the base line and a bistatic range ellipsoid far from the base line. To measure bistatic resolution for these to bistatic range, an additional ellipsoid is created with bistatic range $\Delta\rho$ larger than the actual bistatic range. The area between the two ellipsoid gives the bistatic range cell, or resolution. As it is seen, the area for greater bistatic range is larger, hence the bistatic range resolution.

2.3.4 Bistatic Doppler Resolution

Bistatic Doppler resolution can be defined as the minimum bistatic velocity difference to be distinguished, [49]:

$$\Delta V_b = \frac{\lambda}{2T_{\text{coh}} \cos(\beta/2)}, \tag{2.9}$$

where T_{coh} is the coherent processing interval. The origin of the formula is the radar's capability of differentiating between velocities of two targets. By the definition, for any f_{d_1} and f_{d_2} which are a pair of Doppler frequency that can be resolved by the receiver:

$$|f_{d_1} - f_{d_2}| \geq 1/T_{\text{coh}}. \tag{2.10}$$

For any f_{d_1} and f_{d_2} that has the minimum difference, which results in $|f_{d_1} - f_{d_2}| = 1/T_{\text{coh}}$, defines the Doppler resolution. Let us examine (2.9). For any target position on the base line, where $\beta = 180°$, the Doppler resolution is infinite. This is caused by the geometry of the bistatic radar. Since it is not possible to detect bistatic Doppler shift, it is not possible to distinguish the Doppler shifts. Hence, the bistatic Doppler resolution is infinite on the base line. On the other hand, for the points on the far field or the points on the direction of the base line but not between the transmitter and the receiver, β goes to zero. In that case, the bistatic radar will act like a monostatic radar and the bistatic Doppler resolution will be $\Delta V_b = \frac{\lambda}{2T_{\text{coh}}}$, which equals to radial velocity resolution of a monostatic radar.

2.4 Pulse Chasing

Transmitter-Target-Receiver bistatic target detection is made by using the pulse chasing technique. As it is mentioned, triangulation geometry is created by the transmitter, target and receiver positions. To detect the target, the receiver tries to catch the signals scattered from the targets in the volume illuminated by the transmitter beam in the air. Since the pulse propagates in one direction, the scattered signal can come from any direction the pulse passes through. Hence, the receiver must change its beam direction and width continuously. This beam changing process on the receiver side is called pulse chasing.

The point that should be considered when applying the pulse chasing technique is that the receiver beam must be placed to completely receive the reflected pulse from any target in the pulse direction. Ideally, therefore, the receiver should widen and narrow its beam and change its direction so that it can receive the impulse to be reflected from a target within its sector and range from beginning to end.

Another way of performing pulse chasing is to use more than one beam. In this alternative, which is the highest performance pulse capture technique, a series of overlapping single pulse beam groups at 3dB points are synthesized by the receiver so that they are positioned on the emitter beam. The first beam is in a stationary position until the time delay of the point on that beam's edge. The second beam is aligned near the first beam, and the receiver of the second beam operates until the probable signal is scattered from the edge of the beam. The alignment of the beams is performed by the receiver such that the beamwidths are as narrow as possible. Reflection signals reaching the receiver from each single pulse beam group are reduced independently to the subband and processed with pulse Doppler signal processing units. Instead of using a receiver and signal processing equipment to receive each beam, it is possible to use only two receivers and signal processing units for hardware acquisition. In this case, one receiver and signal processing unit can sequentially process odd-numbered beams and the other even-numbers. One should consider that the hardware requirements for performing pulse chasing using more than one beam increase remarkably and requires significant coordination. For that reason, In our study, pulse chasing with one beam is studied.

The geometry of pulse chasing has shown in Fig. 2.3. While creating this geometry, the main goal is to receive the entire pulse from any target in the transmitted pulse direction. For this, the possible target location should be inside the receiver beam as long as the pulse duration. For this purpose, the front and

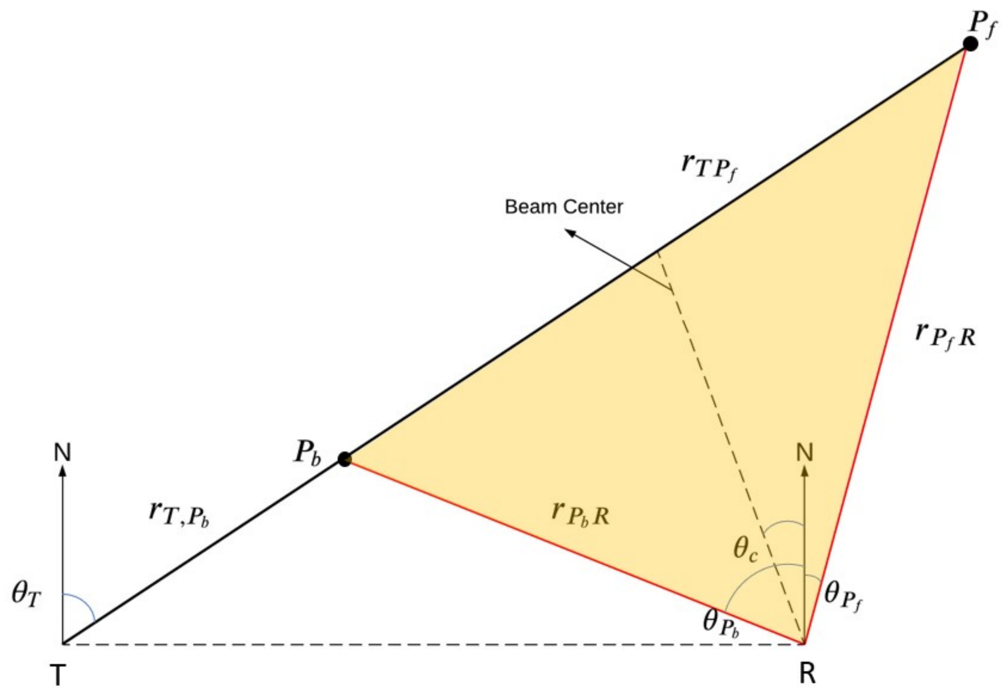

Figure 2.3: Pulse chasing of bistatic radar with narrowbeam receiver whose The front view point $\boldsymbol{P_f}$ and back view point $\boldsymbol{P_b}$ are shown.

back view angles of the beam are named as $\theta_{\boldsymbol{P_f}}$ and $\theta_{\boldsymbol{P_b}}$. Using these angles, the variation of the beam structure with respect to time can be determined. Here, the first looking time to the point $\boldsymbol{P_b}$ is the bistatic range of that point, which is transmitter-$\boldsymbol{P_b}$-receiver triangulation, and can be calculated as

$$\rho = r_{t\boldsymbol{P_b}} + r_{\boldsymbol{P_b}r}, \tag{2.11}$$

where $\rho_{\boldsymbol{P_b}}$ is the bistatic range resulted by the transmitter-$\boldsymbol{P_b}$-receiver triangulation, $r_{T\boldsymbol{P_b}}$ is the distance between the transmitter and the position $\boldsymbol{P_b}$, and $r_{\boldsymbol{P_b}R}$ is the distance between the position $\boldsymbol{P_b}$ and the receiver. The (2.11) is dependent on the position of the point. Hence, the angles made by the target with the receiver and transmitter are covered by the formula. The time to look at $\boldsymbol{P_f}$ is determined by the bistatic range of this point. As it is stated, the point must remain inside of the beam for pulse duration. For this reason, the angle $\theta_{\boldsymbol{P_f}}$ should look at the beginning of the pulse from the possible target location, and the angle θ_{Pb} should look at the end of the pulse from the possible target location so that the relevant target position remains within the beam while the entire pulse is received. For this reason, the bistatic distance of the $\boldsymbol{P_f}$ point is one pulse duration away from the bistatic distance of $\boldsymbol{P_b}$ and is expressed in (2.12):

$$\rho_{\boldsymbol{P_f}} = \rho_{\boldsymbol{P_b}} + cT_p, \tag{2.12}$$

where T_p is the pulse duration. Using (2.12), times to look at $\theta_{\boldsymbol{P_f}}$ and $\theta_{\boldsymbol{P_b}}$ is calculated by dividing the bistatic range to speed of light. To perform pulse chasing, the receiver needs beam center and beamwidth properties. Beam center can be calculated:

$$\theta_c = \frac{\theta_f + \theta_b}{2}, \tag{2.13}$$

and beamwidth can be calculated:

$$\beta_\theta = |\theta_f - \theta_b|. \tag{2.14}$$

Another important issue to be considered here is that only one pulse must pass through the area scanned by the receiver during pulse capture [3]. This subject requires the PRF to be used in the transmitter to be selected as follows:

$$PRF_{DY} = \frac{c}{\rho_{\boldsymbol{P_f}} - \rho_{\boldsymbol{P_b}}} \tag{2.15}$$

An important point to be considered is that in bistatic radar systems where pulse chasing with only one beam is used, the scanning speed of the receiver beam is matched to the angular velocity of the pulse emitted from the transmitter. As it can be seen from the bistatic radar geometry shown in Fig. 2.1, angular velocity depends on the distance and the projection of the velocity vector on the plane perpendicular to the direction to the receiver. Let us examine the case that a pulse is transmitted to a direction close to the receiver. Since angular velocity is directly proportional to the distance, when the pulse is approaching to the receiver, beam rotation is slow. When the pulse is passing in front of the receiver, the beam must be rotated quickly. After the pulse passes the receiver and moves to opposite direction, the beam is rotated slower. Remembering that the pulse travels at the speed of light, the closer the pulse passes to the receiver, the faster the beam must be turned. Although, the beam may not be able to rotate in such speed. In such cases, any reflected signal from a target close to the receiver may not be detected.

Apart from the beam direction, beamwidth also affects the system performance. As it is stated before, any reflected signal from any target at the transmitted beam direction must be received. In order to receive any reflection not only beam direction must be changed, but also the beamwidth must be adjusted. However, wider beamwidth results in poor antenna gain, which results in poor radar performance. Considering this issue, let us examine the previous scenario. When the transmitted beam passes the receiver more closer, the beamwidth must be wider to catch any reflected signal from the target. But if the beamwidth is large, the received signal might be lost because of the poor SNR. To resolve this problem, a number of receivers can be used, which is Multistatic radar system.

2.5 Multistatic Radar Systems

In the broadest sense, multistatic radar systems consist of many radar units placed in different places and cooperate. These units can be selected from monostatic radar systems, radar systems with receivers and transmitters in approximately the same location, and bistatic radar systems. Radar transmitters and receivers are required to transmit and receive the transmitted signals in a manner that they are being informed of each other. This requires significant time synchronization and resource management. Since the developing technological infrastructure has reached the level that can meet these requirements, multistatic radar systems find more and more usage areas and can meet the technical requirements that monostatic radar systems are difficult to meet. Bistatic radar systems, which are the first examples of multistatic radar systems, were used long before monostatic radar systems. The first bistatic radar definition is used in 1955 [1]. As the expectations of military radar systems are getting more and more difficult, multistatic radar systems have been repeatedly turned to and developed significantly. Important details on this subject can be found in Chapter 2 of [3].

The subject of multistatic radar is vast and covers almost all radar technology and application areas. Multistatic radar systems are typically more complex than monostatic radar systems, and signal processing techniques differ significantly. A leading review article on multistatic radar systems was written in 1986 [1].

The only difference between bistatic and multistatic radar systems is that the multistatic radar systems has more than one transmitter and/or receiver. But, they have the same geometry, hence similar characteristics. Additionally, multistatic radar systems have more advantages of using bistatic radar systems. First of all, due to usage of several receiver, the total power received from the reflections on the target increases. In this way, the transmitted power can be saved. Because the signal is scattered to different angles, and by using more receiver, more energy is received than in the bistatic radar systems. Second, the on a target is reduced. Because most of the targets (especially stealth aircrafts) are designed to reduce back-scattering as much as possible. In order to reduce back-scattering, the signal hitting the target is scattered to other directions. By placing receiver at different locations, it is more possible to receive enough energy of reflecting signal. By increasing the level of received signal, detection and tracking performance increases. Thirdly, by seeing the target from different aspects enhances resolution and target classification performance. Fourth, for the cases where individual bistatic pair is not working or has a bad geometry with the target, other bistatic pairs will compensate the shortage when multistatic radar system is used. Lastly, using more than one transmitter saves the receiver from spoofing or other kind of attacks. Because in order to defeat a multistatic radar system, each transmitter and receiver should be aimed.

As it is stated in the introduction part, multistatic radar systems are more complex since all transmitters and receivers must be synchronized, and pulse chasing order of each receiver must be arranged to receive any possible reflections from any possible target location. In such systems, the performance of multistatic radar systems are better than monostatic radar systems.

2.6 Conclusions

In this chapter, we have presented the concept of bistatic radar systems and studied how they work. The advantages and disadvantages of bistatic radar systems over monostatic radar systems are investigated. We have observed that bistatic radar systems are suitable for detecting and tracking target planes with stealth properties. We also observe many advantages of having a passive receiver, such as protection from jamming and attacks and using CW.

Furthermore, the geometry of bistatic radar systems and their effects on radar parameters are studied. We observe that the impact of β is crucial. Because the bistatic Doppler, bistatic range, and Doppler resolution depend on β. For example, it is impossible to measure the Doppler of a target when the target is on the baseline.

In addition, we have reviewed a detection concept of bistatic radar systems called pulse chasing. Briefly, the receiver adjusts its beampattern to "catch" any reflected signal from any point in the transmission direction. The process of performing pulse chasing is highly complex. Moreover, the complexity increases much more for a multistatic radar system. Because the transmit directions, times, and receiver beampatterns must be simultaneously adjusted for the complete regional survey. Therefore, the demand for another multistatic radar system must be satisfied.

Chapter 3

MIMO Radar Systems

3.1 Introduction

We will study the concept of the MIMO radar system in this chapter. This chapter consists of two sections. In Section 3.2, we have defined the MIMO radar signal model. Furthermore, we have discussed the Doppler tolerance of a waveform and how it affects the system.

We reviewed the MIMO radar literature for waveforms with high Doppler tolerance, which are called Doppler-tolerant waveforms. First, we have reviewed piecewise linear frequency modulated (PLFM) waveforms. PLFM waveforms are designed to have the same bandwidth.

In contrast, cross-correlations between each other are adequately low. The waveform consists of two LFM parts: an upchirp LFM part with the maximum specified frequency and a down chirp LFM part with the minimum frequency equal to the maximum frequency of the upchirp LFM. Secondly, the polyphase version of the PLFM waveform is reviewed, called polyphase PLFM (PPLFM). PPLFM consists of phase codes as in the communication system PSK. When the number of chips increases, the PPLFM waveforms becomes more likely to PLFM waveforms.

In Section 3.3, we review the detection schemes that are proposed in the literature. The concept based on performing detection in the position where enough noumber of bistatic range ellipsoid intersects. For that reason, the ROI divided into small cells. For each cell, the received signals are matched filtered and integrated for detection.

3.2 MIMO Radar Signal Model

It is desired that each transmitter uses orthogonal waveforms for any delay and Doppler in interest;

$$\int_0^{T_s} s_k(t)s_m^*(t-\tau)e^{j2\pi f_d t}dt \approx 0, k \neq m$$

On the other hand, one of the most important factor of a waveform is Doppler tolerance. Most of the cases, the waveforms are designed to have high or low Doppler tolerance. Hence, we can divide radar waveforms into two, Doppler tolerant waveforms and Doppler fragile waveforms.

One of the advantages of using a Doppler tolerant waveform is that even if a Doppler shift occurs, The target can be detected by using only one matched filter without the need of Doppler shifting the generated waveform at the filter. However, generally, the receiver needs to apply further processing to estimate the Doppler shift of the detected target, and is mostly unable to distinguish the targets in the same range bin but have different Doppler frequencies. On the other hand, Doppler fragile waveforms can also be used in MIMO radar systems. Since the cross-correlation output of Doppler fragile waveforms are affected by Doppler severely, there must be an matched filter for each Doppler bin, which increases computational complexity. In this section, a number of waveforms in literature are examined.

3.2.1 Piecewise Linear Frequency Modulated Waveforms

Linear frequency modulation (LFM) is frequently used in radar systems. However, little attention has been paid to LFM waveform design with low correlation when multiple transmitters are present. Considering that the radar system will operate within a certain bandwidth, a waveform with a low correlation between the signals are presented in [50]. These waveforms are called piecewise linear frequency modulation or PLFM. This waveform is called ”piecewise” LFM because it consists of two LFM waveforms that do not overlap in time:

$$s(t) = s^a(t) + s^b(t). \tag{3.1}$$

In here:

$$s^a(t) = \begin{cases} \sqrt{\frac{2E_s}{T_s}} \cos(2\pi f_c t + \pi\alpha^a t^2 + \pi\theta^a), & 0 \le t \le \frac{T_s}{2} \\ 0, & elsewhere \end{cases} \tag{3.2}$$

$$s^b(t) = \begin{cases} \sqrt{\frac{2E_s}{T_s}} \cos(2\pi f_c t - 2\pi B_w(t - \frac{T_s}{2}) + \pi\alpha^b t^2 + \pi\theta^b), & \frac{T_s}{2} < t \le T_s \\ 0, & elsewhere \end{cases} \tag{3.3}$$

also, T_s is the signal duration, B_w is the bandwidth, f_c is the carrier frequency, $\alpha^a = \frac{f_a}{T_s/2}$ and $\alpha^b = \frac{B_w - f_a}{T_s/2}$ are the chirp rate of the $s^a(t)$ and $s^b(t)$ respectively, and θ^a and θ^b are the starting phase of the chirps (these phase are used to provide phase continuity between the chirps). The instantaneous frequency versus time of the PLFM waveform is given in Fig. 3.1.

3.2.2 Polyphase-coded PLFM Waveform

In today's technology, it is easy to produce polyphase-coded signals. Most of these signals are used in communication systems, such as phase-shift keying. A polyphase-coded signal is normally generated by changing the phase of an unmodulated reference signal periodically. The time duration of a phase is called chip. A polyphase code consists of a series of phases. Each signal has its own polyphase code:

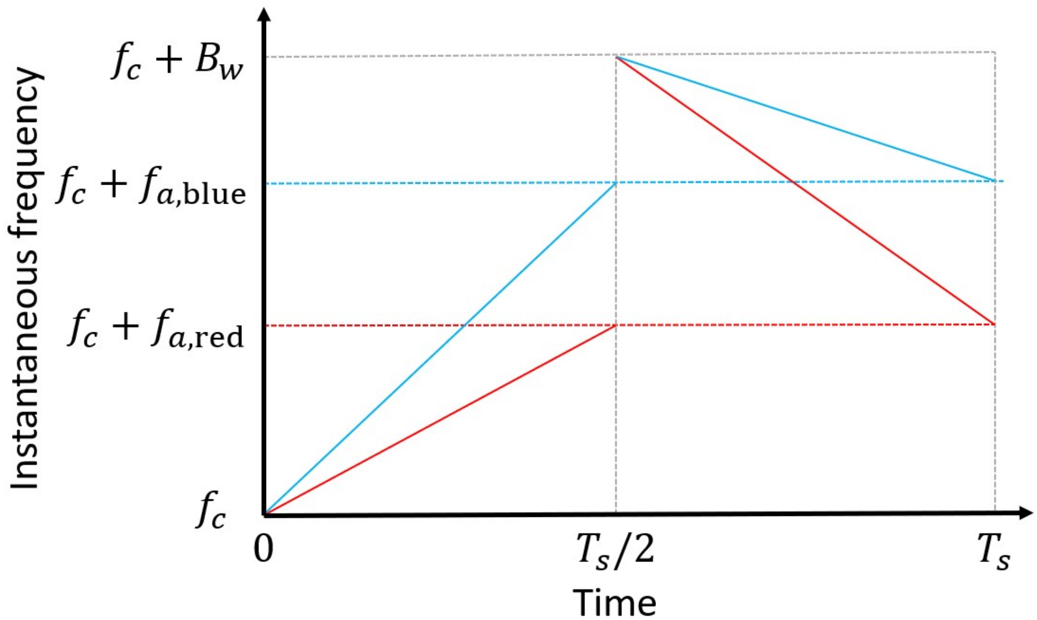

Figure 3.1: Instantaneous frequency versus time graph of Piecewise LFM waveform. Each color represents a different PLFM waveform

$$s_i(t) = \frac{1}{\sqrt{T}_s} \sum_{n=1}^{N} e^{j\phi_i(n)} \operatorname{rect}\left(\frac{t-(n-1)\,T_c}{T_c}\right). \tag{3.4}$$

Here, $s_i(t)$ is baseband, unit energy polyphase-coded signal, N is the number of chips, $T_c = \frac{T_s}{N}$ is the chip duration, $\phi_i\,(n)$ is the polyphase code of i^{th} signal.

Since polyphase-coded signals can be easily generated, PLFM waveforms can be generated as polyphase-coded signal, which is called Polyphase-coded PLFM (PPLFM), [35]. In this thesis, the PPLFM waveform proposed in [35] is studied and a parameter (range and Doppler) estimation technique for multiple target is proposed.

The PPLFM waveform consists of two parts. There are N_i^a number of chips used for the first (upchirp) part and N_i^b number of chips used for the second (downchirp) part for PPLFM waveform of i^{th} transmitter from $L > 1$ number of transmitter. The polyphase code for the first part is denoted by $\phi_i^a\,(n)$ and $\phi_i^b\,(n)$ denotes for the second part. For the previously mentioned PLFM waveform,

$N_i^a = N_i^a = N/2$ must be satisfied. But to refine the main lobe of waveforms with very low or high f_a, the slope of the small part is increased by changing the transformation time. The resulting waveforms are shown in Fig. 3.2.

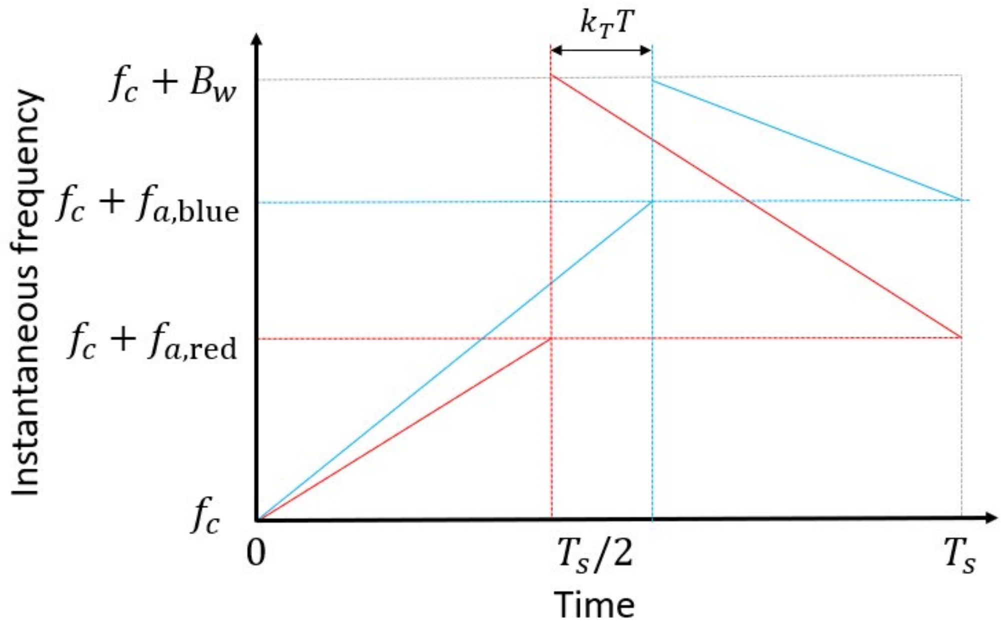

Figure 3.2: Instantaneous frequency versus time graph of PPLFM waveform. Each color represents a different waveform

P3 and P4 polyphase-coded waveforms are simply discrete-time version of conventional LFM waveform. Since a PLFM waveform is a splitted and flipped version of a LFM waveform, PPLFM waveforms can be generated by P3/P4 polyphase codes. The only difference between using P3 and P4 polyphase codes is that the spectrum of P3 is in $f_c < f < f_c + B_w$ and the spectrum of P4 is $f_c - B_w/2 < f < f_c + B_w/2$. In this thesis, we use P3 polyphase code to generate PPLFM.

To generate PPLFM waveform, first, P3 polyphase code is constructed and divided into two part as $\phi_i^{poly,a}(n)$ and $\phi_i^{poly,b}(n)$ with length $N_i^{poly,a}$ and $N_i^{poly,b}$ respectively. The first N_i^a chips are used as $\phi_i^a(n)$. Since the second part is a downchirp signal, $\phi_i^b(n)$ must start from the end of thec$\phi_i^{poly,b}(n)$. The mathematical description of PPLFM waveform is as follows:

$$\begin{aligned}
\phi_i^a(n) &= \phi_i^{poly,a}(n), n = 1, 2, \ldots, N_i^a \qquad (3.5)\\
\phi_i^b(n) &= -\phi_i^{poly,b}\left(N_i^{poly,b} - (n - (N_i^a + 1))\right)\\
&\quad + \phi_i^{poly,a}(N_i^a + 1) + \phi_i^{poly,b}\left(N_i^{poly,b}\right),\\
&\quad n = N_i^a + 1, N_i^a + 2, \ldots, N. \qquad (3.6)
\end{aligned}$$

where the parameters can be computed as:

$$N_i^a = round\left(N\psi_i^T\right), \qquad (3.7)$$

$$N_i^b = N\left(1 - \psi_i^T\right) = N - N_i^a, \qquad (3.8)$$

$$\psi_i^T = \frac{1}{2} - \frac{k_T}{2} + \frac{(i-1)\,k_T}{L-1} \qquad (3.9)$$

$$N_i^{poly,a} = \frac{N\psi_i^T}{\psi_i}, \qquad (3.10)$$

$$N_i^{poly,b} = \frac{N\left(1 - \psi_i^T\right)}{1 - \psi_i}, \qquad (3.11)$$

$$\psi_i = \left(k + \frac{(i-1)(1-2k)}{L-1}\right) \qquad (3.12)$$

The choice of k and k_T parameters here can be done by estimating. For example, $k = i/L$ is a reasonable choice.

To improve Doppler tolerance, hence detection, an extended matched filter (XMF) is proposed in [35]. The matched filter consists of two parts, $f_{i,\mathrm{xmf}}^a(n)$ and $f_{i,\mathrm{xmf}}^b(n)$, which are corresponding to matched filter to upchirp and downchirp parts respectively. The PPLFM extended filters are obtained by extending the lower and upper bound of the n index values in (3.5)-(3.6). For this, the n indices in (3.5) are changed as $n = -N_{i,\mathrm{xmf}}^a, \ldots, N_i^a + N_{i,\mathrm{xmf}}^a$, and the indices used in (3.5) are changed as $n = N_i^a - N_{i,\mathrm{xmf}}^b + 1, N_i^a + 2, \ldots, N + N_{i,\mathrm{xmf}}^b$ to obtain an XMF for PPLFM waveform. Here, the parameters $N_{i,\mathrm{xmf}}^a$ and $N_{i,\mathrm{xmf}}^b$ are the number of additional chips at the edges of the signals to create an XMF:

$$N^a_{i,\text{xmf}} = \frac{p_{\text{xmf}} N \psi_i^T}{\psi_i} \ , \tag{3.13}$$

$$N^b_{i,\text{xmf}} = \frac{p_{\text{xmf}} N \left(1 - \psi_i^T\right)}{1 - \psi_i} \ . \tag{3.14}$$

In the equations above, p_{xmf} is the ratio that indicates how much the bandwidth of the XMF will increase. An example of XMF is shown in Fig. 3.3.

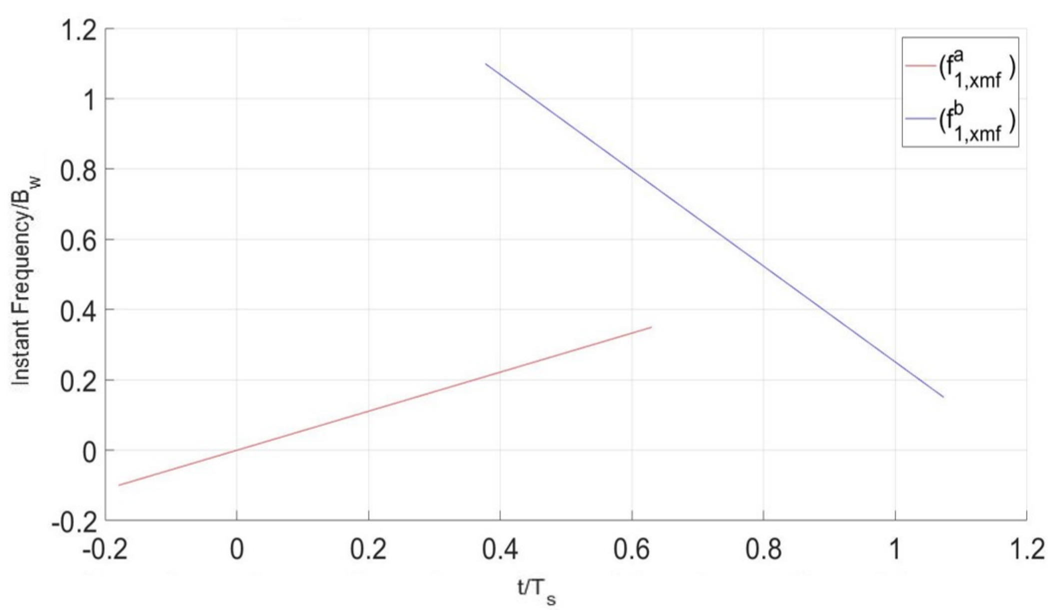

Figure 3.3: Extended matched filter for $f_a = 0.25B_w$ with $p_{\text{xmf}} = 0.1$

The resulting PPLFM waveforms are highly Doppler tolerant. Although, the Doppler of the target can be estimated by further processing on the detections. In [50], the estimation procedure when there is only one target is present is studied.

Let's consider one target case. The parts of the XMF, $f^a_{i,\text{xmf}}(n)$ and $f^b_{i,\text{xmf}}(n)$ are applied separately. This separated output results in the same filter since XMF is the summation of two parts in time space.

$$f_{i,\text{xmf}}(t) = f^a_{i,\text{xmf}}(t) + f^b_{i,\text{xmf}}(t) \tag{3.15}$$

Two separate matched filter outputs are obtained from the XMF. Detections are generated on both matched filter outputs before estimation is performed. Doppler estimation is made by using the detected time delays from two separate matched filter outputs. Let the delay obtained from the matched filter outputs of the first and second signals be T_i^a and T_i^b. The Doppler of the target can be estimated using the difference between these two delay estimations:

$$\hat{f}_D = \frac{\beta_i \psi_i (1-\psi_i)}{T_c \left[\psi_i \left(1-\psi_i^T\right) + \psi_i^T (1-\psi_i)\right]} \tag{3.16}$$

where β_i is the normalized time difference:

$$\beta_i = \frac{T_i^b - T_i^a}{T_s} \; . \tag{3.17}$$

Bistatic Doppler velocity can be estimated using the resulting Doppler estimation:

$$\hat{v} \approx \frac{c\hat{f}_D}{f_c + \hat{f}_D} \; . \tag{3.18}$$

The signal delay due to the target's range is estimated using the average of the detected time delays:

$$\widehat{T}_i = \frac{\hat{T}_i^a + \hat{T}_i^b}{2} \; . \tag{3.19}$$

Note that the target delay and Doppler are estimated with only a pair of matched filters, and any integration is performed. In that case, there are two peaks for both XMF parts. This means that both peaks in the outputs will have a 3dB decrease. Hence, when we apply the threshold, the probability of detection decreases. In contrast, we can perform incoherent integration to perform detection without 3dB loss. First, we apply $f_{i,\mathrm{xmf}}^a(t)$ and $f_{i,\mathrm{xmf}}^b(t)$ separately. Let us define the XMF outputs as $y_i^a[n]$ and $y_i^b[n]$ respectively. In conventional case, the incoherent integration is performed as follows [51]:

$$z^a[n] = \sum_{i=0}^{N_p-1} |y_i^a[n]|^2, \tag{3.20}$$

$$z^b[n] = \sum_{i=0}^{N_p-1} |y_i^b[n]|^2, \tag{3.21}$$

where N_p is the number of pulses. On the other hand, we know from (3.16) that Doppler is proportional to the difference between the peak points of the XMF outputs. In order to understand, let us investigate the output characteristic and range-Doppler coupling for incoherent integration. First, a received signal with delay τ and zero Doppler frequency is shown in Fig. 3.4.

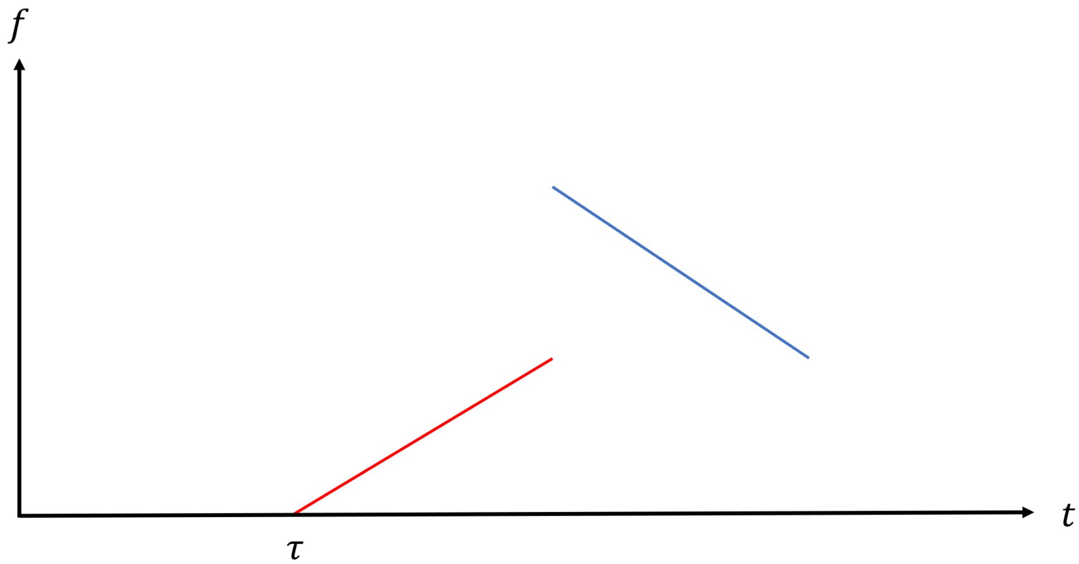

Figure 3.4: Time and frequency domain representation of a received signal with delay τ and zero Doppler.

The matched filter is applied by shifting the XMFs shown in Fig. 3.3, multiplying the signal with the received signal, and summing over time. The resulting outputs for both $f^a_{i,\mathrm{xmf}}(t)$ and $f^b_{i,\mathrm{xmf}}(t)$ will be have a peak in τ. However, in the presence of Doppler, the peaks will shift as a result of range-Doppler coupling. To understand, let us investigate the outputs for the received signal with delay τ and Doppler frequency f_D which is shown in Fig. 3.5.

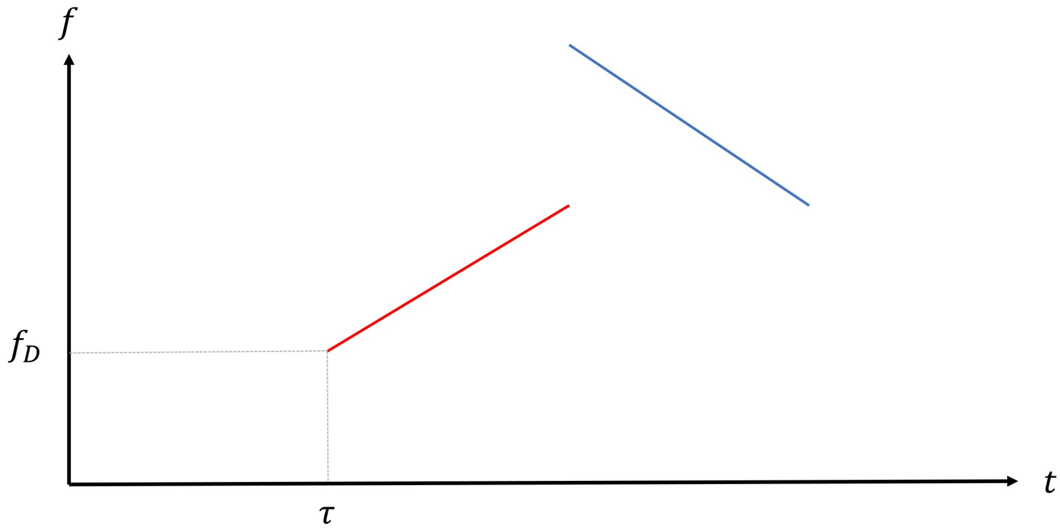

Figure 3.5: Time and frequency domain representation of a received signal with delay τ and Doppler frequency f_D.

First, we apply the first XMF $f^a_{i,\text{xmf}}(t)$ on the received signal. the filter output at τ is not high enough since the XMF and the first part of the received signal does not overlap as shown in Fig. 3.6.

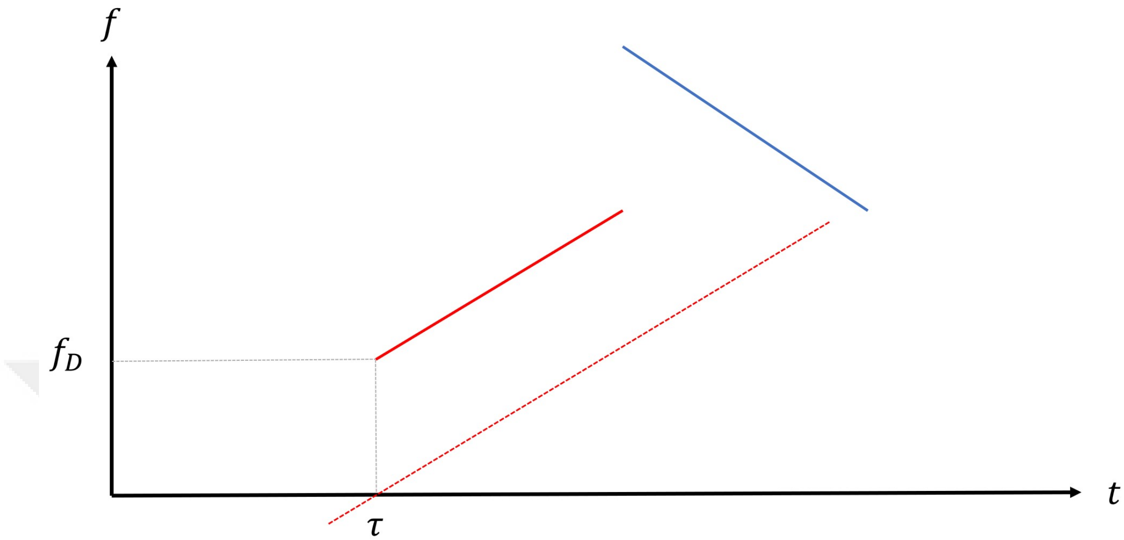

Figure 3.6: Matched filter output at the true delay value τ. The filter and received signal does not overlap which results in low output. The dashed lines present XMF and the solid lines present the received signals.

For a proper correlation, the XMF must be shifted to the left as shown in Fig. 3.7.

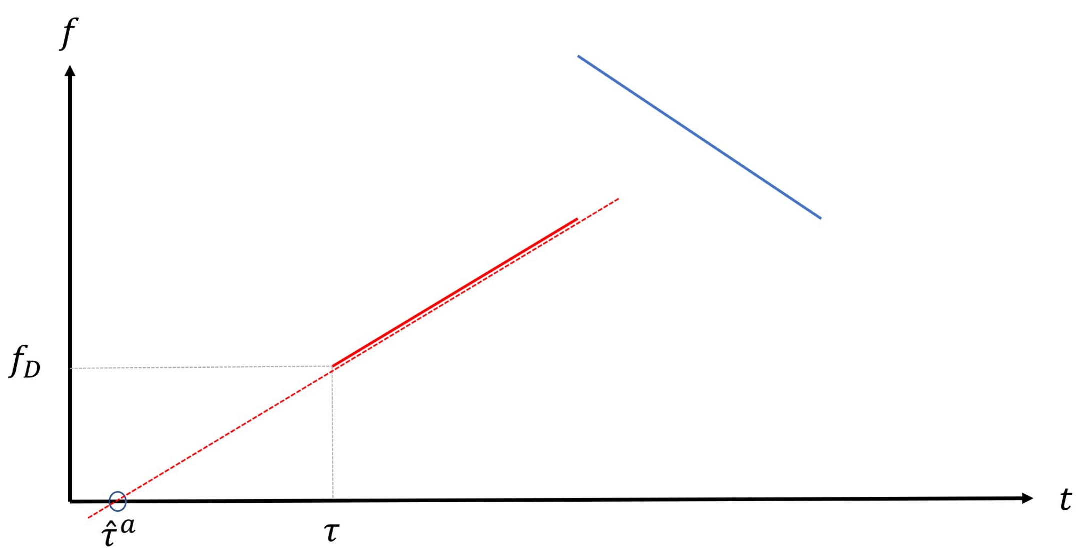

Figure 3.7: Matched filter output at proper delay. The peak is at $\hat{\tau}^a$. The dashed lines present XMF and the solid lines present the received signals.

The similar case is observed for the second part of the signal as shown in Fig. 3.8.

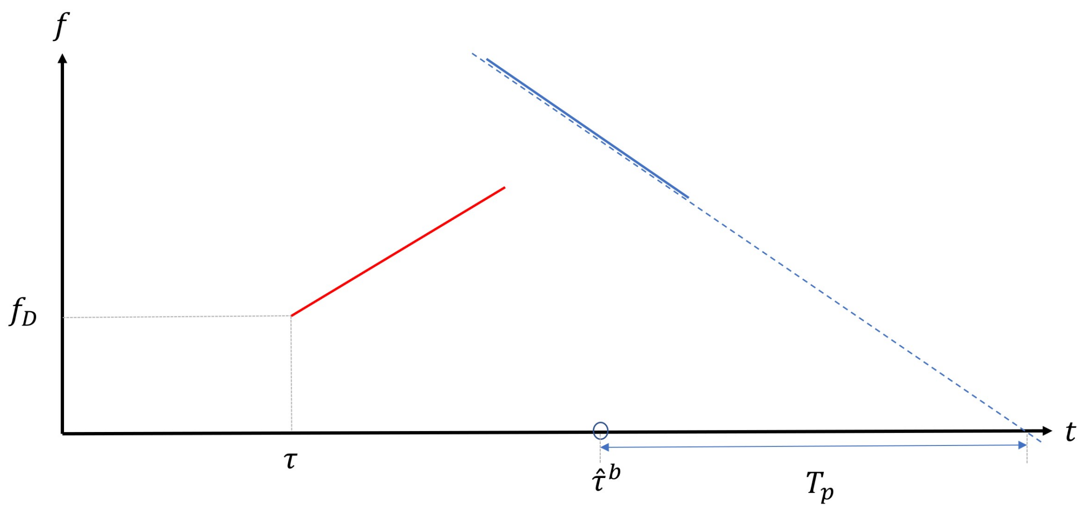

Figure 3.8: Matched filter output at proper delay. The peak is at $\hat{\tau}^b$. The dashed lines present XMF and the solid lines present the received signals.

As we can see, Doppler results in a shift in the matched filter output. This case is named "range-Doppler coupling" [51]. For the up chirp part, a positive Doppler results in a shift of mainlobe in negative delay. On the other hand, a positive Doppler results in a shift of mainlobe in positive delay.

For detection, a threshold γ_{pre} is applied for both $f^a_{i,\text{xmf}}(t)$ and $f^b_{i,\text{xmf}}(t)$ outputs. The threshold exceeding points can be incoherently integrated by adding the threshold exceeding points with each other. Finally, target detection is performed if the integration result exceeds another threshold γ_{tot}. This process enhances the system performance in several ways. One of the advantages is the decrease in false alarm with the the same probability of detection. For example, let us consider a two target case. In that case, we have points exceeding γ_{pre} for the first part and the two points for the second part. We have two correct combinations and two incorrect combinations. By performing incoherent integration, we can eliminate the false combinations since we apply another threshold γ_{tot} on the integration output.

Note that the phases are eliminated since we only consider use the absolute value of the phases. In contrast, we can have a 3dB increase if we know the phases of the filter outputs and integrate them coherently. For that reason, let us investigate the coherent integration for PLFM or PPLFM waveforms.

As it is given in (3.1), signal consists of two parts. For the sake of simplicity, let us redefine the signals

$$s_1(t) = e^{j\pi\beta_1 t^2} e^{j2\pi f_1 t} \mathrm{rect}(t/(T/2)), \tag{3.22}$$

$$s_2(t) = e^{j\pi\beta_2 t^2} e^{j2\pi f_2 t} \mathrm{rect}(t/(T/2)), \tag{3.23}$$

$$s(t) = s_1(t) + s_2(t - \frac{T}{2}). \tag{3.24}$$

Using this definition, we can define a received signal with delay τ_0 and Doppler frequency with ν_0:

$$r(t) = s(t - \tau_0) e^{j2\pi\nu_0 t} \tag{3.25}$$

The matched filtered signals can be written as follows

$$y_1(\tau) = \int e^{-j\pi\beta_1(t-\tau)^2} e^{-j2\pi f_1(t-\tau)} r(t)dt, \tag{3.26}$$

$$y_2(\tau) = \int e^{-j\pi\beta_2(t-\frac{T}{2}-\tau)^2} e^{-j2\pi f_2(t-\frac{T}{2}-\tau)} r(t)dt. \tag{3.27}$$

$$y_1(\tau) \cong \int e^{-j\pi\beta_1(t-\tau)^2} e^{-j2\pi f_1(t-\tau)} s_1(t-\tau_0) e^{j2\pi\nu_0 t} dt,$$

$$y_2(\tau) \cong \int e^{-j\pi\beta_2(t-\frac{T}{2}-\tau)^2} e^{-j2\pi f_2(t-\frac{T}{2}-\tau)} s_2(t - \frac{T}{2} - \tau_0) e^{j2\pi\nu_0 t} dt.$$

Redefining $t - \frac{T}{2} \to t$:

$$y_2(\tau) = \underbrace{\left[\int e^{-j\pi\beta_2(t-\tau)^2} e^{-j2\pi f_2(t-\tau)} s_2(t-\tau_0) e^{j2\pi\nu_0 t} dt\right]}_{\tilde{y}_2(\tau)} e^{j2\pi\nu_0\frac{T}{2}},$$

$$
\begin{aligned}
y_1(\tau) &= \int_{\tau_0}^{\tau_0+T/2} e^{-j\pi\beta_1(t-\tau)^2} e^{-j2\pi f_1(t-\tau)} e^{-j\pi\beta_1(t-\tau_0)^2} e^{-j2\pi f_1(t-\tau_0)} e^{j2\pi\nu_0 t} dt \\
&= \int_{\tau_0}^{\tau_0+T/2} e^{-j\pi\beta_1 t^2} e^{j\pi\beta_1 t\tau} e^{-j\pi\beta_1\tau^2} e^{-j2\pi f_1 t} e^{j2\pi f_1\tau} \\
&\qquad e^{j\pi\beta_1 t^2} e^{-j\pi\beta_1 t\tau_0} e^{j\pi\beta_1\tau_0^2} e^{j2\pi f_1 t} e^{-j2\pi f_1\tau_0} e^{j2\pi\nu_0 t} dt \\
&= \underbrace{\left(\int_{\tau_0}^{\tau_0+\frac{T}{2}} e^{j2\pi(\beta_1\tau-\beta_1\tau_0+\nu_0)t} dt\right)}_{\approx\frac{T}{2} \text{ if } \tau=\tau_0-\frac{\nu_0}{\beta_0}} e^{-j\pi\beta_1\tau^2} e^{j2\pi f_1\tau} e^{j\pi\beta_1\tau_0^2} e^{-j2\pi f_1\tau_0}.
\end{aligned}
$$

Therefore, the output at delay $\tau_0 - \frac{\nu_0}{\beta_1}$

$$
y_1(\tau_0 - \frac{\nu_0}{\beta_1}) = \frac{T}{2} e^{-j2\pi\nu_0\tau_0} e^{-j\pi\nu_0^2/\beta_1} e^{-j2\pi f_1 \frac{\nu_0}{\beta_1}}
$$

Applying the same process for $\tilde{y}_2(\tau)$ results in

$$
\tilde{y}_2(\tau_0 + \frac{\nu_0}{\beta_1}) = \frac{T}{2} e^{-j2\pi\nu_0\tau_0} e^{-j\pi\nu_0^2/\beta_2} e^{-j2\pi f_2 \frac{\nu_0}{\beta_2}}
$$

Hence, the resulting outputs are

$$
y_1(\tau_0 - \frac{\nu_0}{\beta_1}) = \frac{T}{2} e^{j2\pi\left(\tau_0\nu_0 - \frac{\nu_0^2}{2\beta_1} - f_1\frac{\nu_0}{\beta_1}\right)} \tag{3.28}
$$

$$
y_2(\tau_0 + \frac{\nu_0}{\beta_2}) = \frac{T}{2} e^{j2\pi\left(\tau_0\nu_0 + \frac{\nu_0^2}{2\beta_2} + f_2\frac{\nu_0}{\beta_2} + \nu_0 T/2\right)} \tag{3.29}
$$

Now, we can formulate the coherent integration as:

$$
z(t_1, t_2) = y_1(t_1) e^{\frac{\nu_0^2}{2\beta_1} + f_1\frac{\nu_0}{\beta_1}} + y_2(t_2) e^{-\frac{\nu_0^2}{2\beta_2} - f_2\frac{\nu_0}{\beta_2} - \frac{\nu_0 T}{2}}. \tag{3.30}
$$

For detection, we must apply threshold on $z(t_1, t_2)$ to detect presence of a peak. After detection is performed, delay and Doppler can be estimated at the peak location (t_1, t_2). We know the real delay and Doppler at $\left(\tau_0 - \frac{\nu_0}{\beta_1}, \tau_0 + \frac{\nu_0}{\beta_2}\right)$:

$$
\nu_0\left(\frac{1}{\beta_1} + \frac{1}{\beta_2}\right) = t_2 - t_1 \Longrightarrow \hat{\nu}_0 = \frac{\beta_1\beta_2(t_2 - t_1)}{\beta_1 + \beta_2} \tag{3.31}
$$

$$
\tau_0 = t_1 + \frac{\nu_0}{\beta_1} \Longrightarrow \hat{\tau}_0 = \frac{\beta_1 t_1 - \beta_2 t_2}{\beta_1 + \beta_2} \tag{3.32}
$$

Using (3.32) and (3.31), delay and Doppler of the detected point (t_1, t_2) can be estimated.

Note that the search area is two dimensional since the $z(t_1, t_2)$ is a function of t_1 and t_2. On the other hand, we only use two different matched filters in zero Doppler cut as given in (3.15). That means when we use coherent integration, the computational complexity increases from $O(2N_s)$ to $O(N_s^2)$ where N_s is the number of samples in pulse duration. In other words, in the algorithm given in [34], we search for peaks in two matched filter outputs with one dimension. On the other hand, we must search for peaks in two dimensions for the coherent integration case. Although coherent integration brings computational complexity, it prevents the system from 3dB loss. With the 3dB increase, the probability of detection increases.

Since only one target case is studied in the paper [50], a novel method to estimate the range and Doppler in multiple target cases is proposed in the next chapter of this thesis.

3.3 MIMO Radar Moving Target Detection

MIMO radar detection systems are a subject that has been studied for a long time. The relatively old studies are [12, 22, 23, 52, 53, 54, 37, 55]. It is still a hot topic in literature. Some of the remarkable studies in the recent years are [56, 57, 58].

MIMO radar systems can perform detection in two ways, centralized or distributed. To perform centralized detection, receivers must sample and send the received signals to a center where a decision is made whether there is a target or not. This system requires complex communication networks. On the other hand, in distributed detection systems, each receiver makes soft decisions, and these soft decisions are sent to the fusion center. Great majority of these papers filters the received signal for a specific range and Doppler gate, which defines a point and a velocity for a possible target, integrate each transmitter-receiver pair filter output, and apply threshold to a defined likelihood function.

There are some advantages of using MIMO radar for target detection, especially the moving targets. Being able to evaluate the signals reaching the receiver together also contributes to the performance. Receiving reflected signals from different aspects also enhances detection performance for the targets with fluctuating RCS. It is also possible to increase probability of detection by using the estimated Doppler shifts. Because the probability of detection of Doppler shifted signals are higher in clutter. Some of the studies examining the effect of Doppler shift to detection performance, [12, 59, 54].

In [59], centralized and distributed MIMO detection technique are proposed. For distributed detector, each receiver makes soft decisions for each transmitter signal. Soft decisions are Doppler estimates in this paper. Each Doppler estimate is sent to a fusion center. Fusion center performs detection, which is called hard decision. The disadvantages of using Doppler estimates for detection are that the clutter model must be known; for some cases, Doppler estimation may not be performed for some transmitter-receiver pairs.

Another important problem of the studies in the literature is that only one point on space is considered, hence the detection is performed using a matched filter specifically designed for the corresponding range and Doppler bin, or it is assumed that the number of target is known. For the unknown number of target case, for each possible location, a time and Doppler shifted waveform should be generated and used to filter the received filter for each possible point where a target can be presence. In order to perform such a detection system, in [12], A grid of possible target points is created inside the region of interest. Such scheme is shown in Fig. 3.9.

For any point on grid, detection is performed by filtering the received signal by a generated waveform for that specific point, and a threshold is applied on a likelihood function. Assume the detection algorithm is working on two dimensional space. Let $\boldsymbol{P}_i = \begin{bmatrix} x_i & y_i \end{bmatrix}^T$ be the i^{th} point position on the grid, and $\boldsymbol{P}_{tgt} = \begin{bmatrix} x_{tgt} & y_{tgt} \end{bmatrix}^T$ be the position of the target. The matched filter output of the k^{th} transmitter and l^{th} receiver for the i^{th} grid point can be shown as:

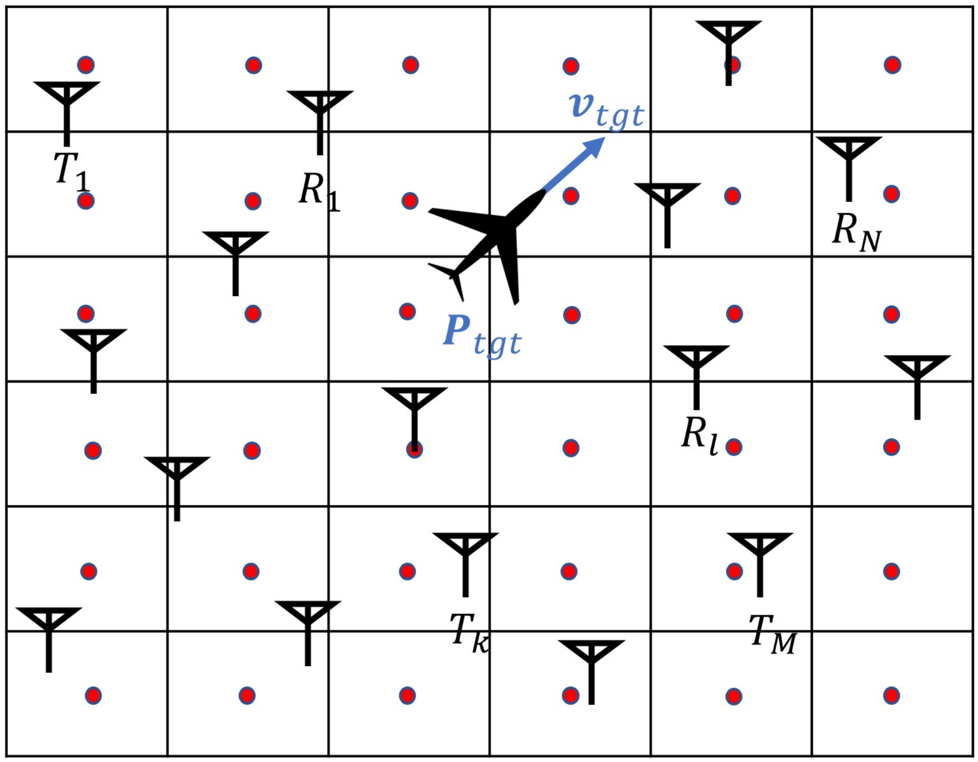

Figure 3.9: Detection of the target at $\boldsymbol{P}_{tgt}$ with velocity $\boldsymbol{v}_{tgt}$ using MIMO radar system. Red dots define the generated grid points for detection. The antenna T_i defines the i^{th} transmitter antenna and R_j defines the j_{th} receiver antenna.

$$y_{k,l}\left(\boldsymbol{P}_i\right) = \int_0^{T_s} y\left(t;l\right) s_{k,1}^{*}\left(t - \tau_{T_k}\left(\boldsymbol{P}_i\right) - \tau_{R_l}\left(\boldsymbol{P}_i\right)\right) dt, \tag{3.33}$$

where $y\left(t;l\right)$ is the received signal of l^{th} receiver, $\tau_{T_k}\left(\boldsymbol{P}_i\right) = r_{T_k\boldsymbol{P}_i}/c$ and $\tau_{R_l}\left(\boldsymbol{P}_i\right) = r_{\boldsymbol{P}_iR_l}/c$. After obtaining matched filter output for each transmitter-receiver pair, a variable defined by likelihood is calculated and thresholded for detection.

As can be seen from the above, for each point on the grid, the signal $s_{k,1}^{*}\left(t - \tau_{T_k}\left(\boldsymbol{P}_i\right) - \tau_{R_l}\left(\boldsymbol{P}_i\right)\right)$ is generated and integrated with the received signal, which brings unacceptable computational complexity. As it is discussed in the previous section, it is possible to estimate delay and Doppler of a signal by only using one matched filter. In Chapter 4 of the thesis, some novel detection techniques are proposed.

3.4 Conclusions

In this chapter, we have reviewed the concept of the MIMO radar system by studying its signal model, waveforms presented in the literature, and the detection scheme proposed in the literature. We see that there are mainly two types of waveforms; Doppler-fragile and Doppler-tolerant waveforms. These types are determined by a property called Doppler tolerance. The length of the main lobe determines Doppler tolerance at the matched filter output in the frequency axis. In other words, Doppler tolerance is the maximum Doppler where the received signal can still be detected. Doppler-tolerant waveforms have high Doppler tolerance, while Doppler-fragile waveforms have low Doppler tolerance.

We have observed that the Doppler-fragile waveforms are more interested in the MIMO radar literature since detecting and estimating the delay and Doppler value is easy. On the other hand, we observed remarkable Doppler-tolerant waveforms available in the literature, two of which are PLFM and PPLFM waveforms. We have studied these waveforms in detail. We have reviewed the extended matched filter and estimated the delay and Doppler value by using the detection points.

We have reviewed the detection system of MIMO radar systems. In the MIMO radar literature, a detection scheme is generally based on generating a grid of points. Typically, detection is performed by using noncoherent integration and thresholding. The matched filtering for a possible target point is performed, and the filtered and integrated signal is thresholded. We have observed that the solutions in the literature bring high computational complexity and are studied for a zero Doppler environment. Hence, we have turned our focus on these problems.

Chapter 4

Proposed MIMO Radar Target Detection and Tracking

4.1 Introduction

In this chapter, a number of novel techniques for MIMO radar systems are proposed. First, A target parameter estimation in presense of multiple target using polyphase-coded piecewise linear frequency modulated (PPLFM) waveform is proposed. Our method depends on the idea of data association. We first apply matched filter on received signal and create plots by thresholding. The matched filter consists of two parts, hence two different output point set is obtained. The each combination of points from first and second set are associated and corresponding range and Doppler value examined. If range or Doppler exceeds a certain interval, the point is ignored. As a result, only the plots corresponding to the real targets are aimed to be used.

Secondly, an alternative MIMO radar antenna which is called Electromagnetic Vector Antenna (EMVA) and its properties and suitability for MIMO radar applications are studied.

Third, target detection techniques for MIMO radar are proposed. The target detection technique for MIMO radar using bistatic-range-based, bistatic range and Doppler based, bistatic range and DOA based target detection techniques are studied separately.

Fourth, a policy iteration based position and velocity estimation technique is proposed. Lastly, a Generalized Multi Bernoulli filter is designed for target tracking using the bistatic range and Doppler measurements.

4.2 Range and Doppler Estimation of Multiple Targets Using PPLFM Waveform

In [50], PPLFM waveform and technique to estimate range and Doppler of a target is proposed. However, they did not studied multiple target case. In this section, multiple target range and Doppler estimation case is studied.

When multiple targets are present, the detections observed in the matched filter outputs must be correctly correlated with the targets. For easy understanding, the algorithm will be explained through two target example. There are two T_i^a values and two T_i^b values when there are two targets are present. The right combination of these detections is not known. If there is a significant amplitude difference between these detections, correct matching can be determined by matching detections with similar amplitudes. However, if the amplitude difference between detections is not selective enough, all possible matches are considered. Therefore, Doppler and signal delay are obtained for each T_i^a and T_i^b mapping. In the case given as an example, although there are two targets, four targets are detected. Here, two unreal targets out of the four are called ghost targets. Note that even there are four possible target points, only two possible combinations are available since both values of T_i^a and T_i^b are should be used. Another way is to apply maximum and minimum thresholds on the estimated Doppler and delay values. Thus, if the Doppler or delay values estimated by using the wrong pairings are not within the expected value range, the wrong pairing is eliminated. Another way is to set maximum and minimum thresholds for matched groups. For example, when a T_i^a and a T_i^b are matched in the given two target examples, these two are matched because there is only one T_i^a and T_i^b left. This method is shown in Fig. 4.1.

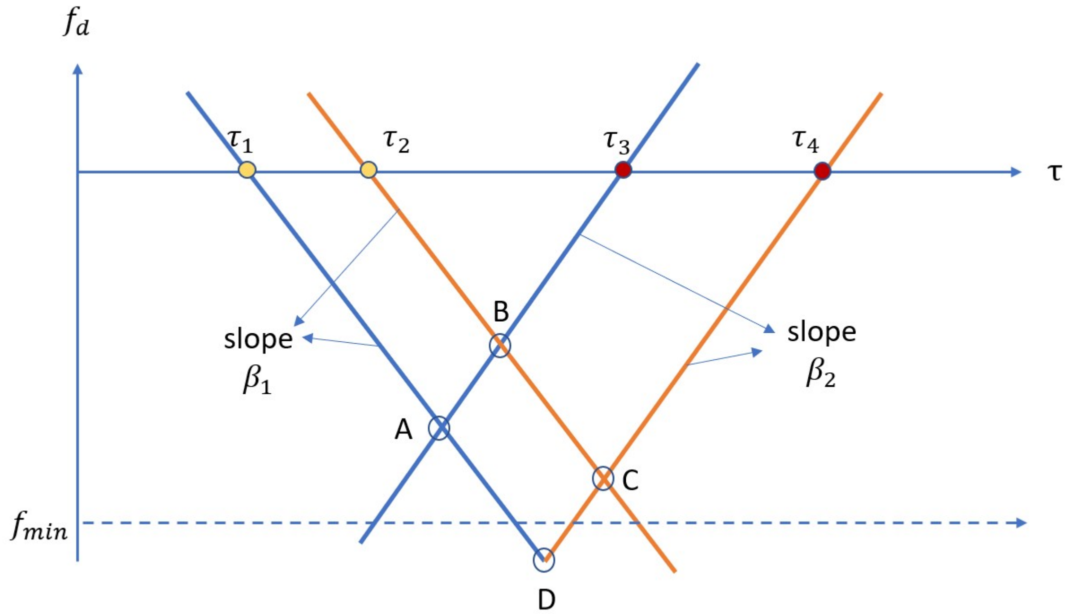

Figure 4.1: Point association of matched filter output for PPLFM waveform. f_{min} is the minimum Doppler of a possible target.

In Fig. 4.1:

- A is the intersection of lines $\beta_1(\tau - \tau_1)$ and $\beta_2(\tau - \tau_3)$
- B is the intersection of lines $\beta_1(\tau - \tau_2)$ and $\beta_2(\tau - \tau_3)$
- C is the intersection of lines $\beta_1(\tau - \tau_2)$ and $\beta_2(\tau - \tau_4)$
- D is the intersection of lines $\beta_1(\tau - \tau_1)$ and $\beta_2(\tau - \tau_4)$

According to these given line equations, the delays and Dopplers are obtained as follows:

- $A = \left(\frac{\beta_2 \tau_3 - \beta_1 \tau_1}{\beta_2 - \beta_1}, \frac{\beta_1 \beta_2}{\beta_2 - \beta_1} (\tau_3 - \tau_1) \right)$
- $B = \left(\frac{\beta_2 \tau_3 - \beta_1 \tau_2}{\beta_2 - \beta_1}, \frac{\beta_1 \beta_2}{\beta_2 - \beta_1} (\tau_3 - \tau_2) \right)$
- $C = \left(\frac{\beta_2 \tau_4 - \beta_1 \tau_2}{\beta_2 - \beta_1}, \frac{\beta_1 \beta_2}{\beta_2 - \beta_1} (\tau_4 - \tau_2) \right)$
- $D = \left(\frac{\beta_2 \tau_4 - \beta_1 \tau_1}{\beta_2 - \beta_1}, \frac{\beta_1 \beta_2}{\beta_2 - \beta_1} (\tau_4 - \tau_1) \right)$

As mentioned, if these obtained points are grouped, two possible matches are obtained. For example, when τ_1 is paired with τ_3, the remaining τ_2 and τ_4 are also paired. Thus, points A and C are obtained. Or, when τ_1 is matched with τ_4, τ_2 and τ_3 are also matched to obtain B and D points. One way to determine which of these mappings is false is to apply the maximum and minimum thresholds to the Doppler and delay. Thus, the wrong pairing can be determined if the estimated Dopplers or delays are not within the expected value range.

In case the proposed method for the detection of close targets cannot determine which of the two possible matches is correct, it is transmitted to the target trace generation stage as plots in both cases. Using these plots transmitted in successive time intervals, the tracking algorithm which is proposed in this thesis can detect plots that are compatible with the target trace and initiate a reliable trace.

Note that the described litations can be reduced by using two matched filter in different Doppler frequency for each waveform instead of using only one matched filter. Hence, the association problem becomes more reliable with the cost of slightly increase in computational complexity.

4.3 Alternative MIMO Antenna Structures

MIMO radar transmitters radiate energy to simultaneously illuminate targets in a large search volume. Therefore, MIMO receivers are designed to intercept target reflections that can impinge on a wide range of directions. For this purpose, MIMO systems typically employ dipole antennas. However, there exists other

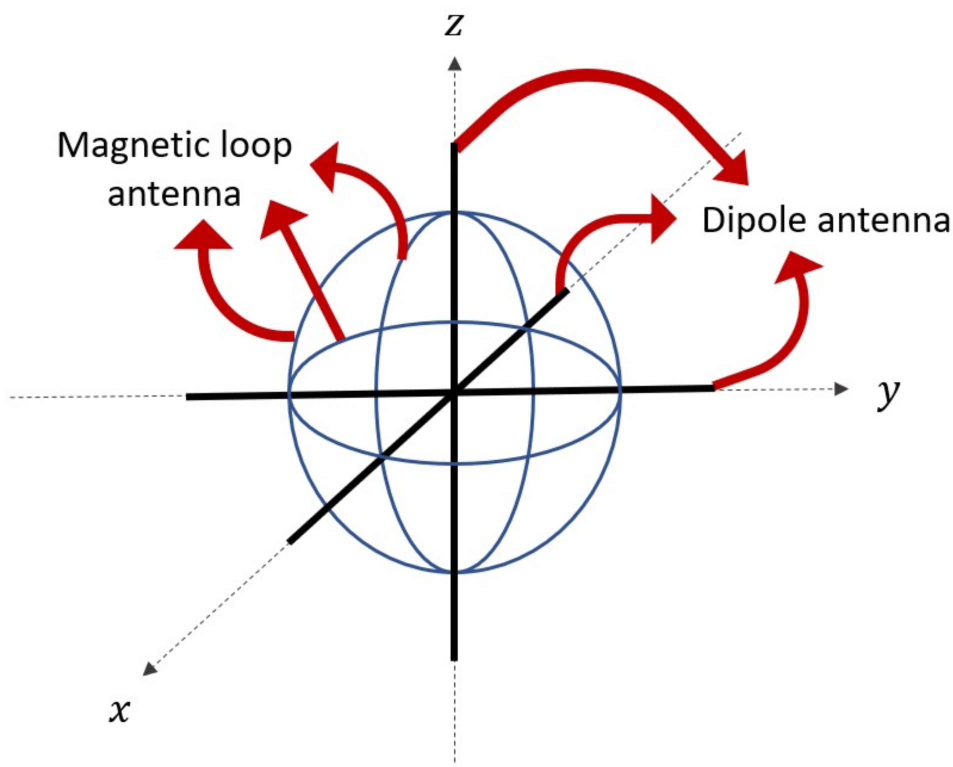

Figure 4.2: Electromagnetic vector antenna, [2]. Black lines and blue circles represent electric dipole and magnetic loop antennas respectively.

viable alternative antenna systems that can be used in MIMO radar systems. In this chapter, we will consider in detail one such alternative antenna system which is known as Electromagnetic Vector Antenna (EMVA) [60]. In this structure, dipole antennas are used to evaluate the electric field, and magnetic loop antennas are used to evaluate the magnetic field. The proposed antenna structure is given in Fig. 4.2. EMVA antenna has many advantages over most of the other antenna types. Using EMVA, it is possible to measure the magnitude of electric and magnetic fields in all directions. It is possible to estimate the direction of arrival and the polarization by processing the measured magnitude. Before going into detail, we will explain electromagnetic waves and the characteristics of some essential antennas.

There are some EM wave models such as spherical, cylindrical, and plane.

These types specify the direction of the waves. For example, in the spherical model, the wave propagates to space from a point. Hence the wave consists of an infinite number of vectors pointing perpendicular to any sphere whose center is the source. The most commonly used wave is the plane wave. The reason is that in any finite region that is sufficiently far from the source of the EM wave, it can be assumed that at any point in the region, the wave has the same direction. In other words, for any plane that is perpendicular to the direction of the EM, the magnitude and phase of the electric and magnetic field remain locally constant, [61].

Let us define electric field and magnetic field by functions as $\mathbf{E}(x, y, z; t) = \mathrm{Re}\{\mathbf{E}^0(x, y, z)e^{jwt}\}$ and $\mathbf{H}(x, y, z; t) = \mathrm{Re}\{\mathbf{H}^0(x, y, z)e^{jwt}\}$ respectively, where $\mathbf{E}^0(x, y, z)$ and $\mathbf{H}^0(x, y, z)$ are the phasor terms. Note that the phasor terms define the phase differences and field directions. Then the wave equations can be given as follows, [61]:

$$\nabla^2\mathbf{E} + k^2\mathbf{E} = 0, \tag{4.1}$$

$$\nabla^2\mathbf{H} + k^2\mathbf{H} = 0, \tag{4.2}$$

where $k = w\sqrt{\mu\epsilon}$, $w = 2\pi f_c$, and μ and ϵ are permittimity and permeability of the material that the wave is propagating. Note that in free space, $1/\sqrt{\mu_0\epsilon_0} = c$ the speed of light.

In order to examine the characteristic of electromagnetic waves, some parameters need to be defined. Hence, we define electric and magnetic field by vector components at zero instant:

$$\mathbf{E}^0(x, y, z) = \vec{\mathbf{a}}_x E_x^0 + \vec{\mathbf{a}}_y E_y^0 + \vec{\mathbf{a}}_z E_z^0, \tag{4.3}$$

$$\mathbf{H}^0(x, y, z) = \vec{\mathbf{a}}_x H_x^0 + \vec{\mathbf{a}}_y H_y^0 + \vec{\mathbf{a}}_z H_z^0. \tag{4.4}$$

Note that at any instant, the magnitude and phase of $\mathbf{E}$ and $\mathbf{H}$ are constant on the plane perpendicular to the direction of propagation. The direction of propagation, magnitude and phase of each field is determined by the phasor terms, $E_x^0, E_y^0, E_z^0, H_x^0, H_y^0, H_z^0$.

Let us define a local coordinate frame $\{l\}$ where $\vec{\mathbf{a}}_{x'}, \vec{\mathbf{a}}_{y'}, \vec{\mathbf{a}}_{z'}$ are unit vector representation of principal directions. Any EM wave can be defined in any direction using that local coordinate frame. To obtain the EM wave in the general frame, rotation matrices can be used. An easy way to obtain rotation matrix, the projections of each unit vector defining the principal direction of local frames on the general frame can be taken, [62]:

$$ {}^{l}\mathbf{R} = \begin{bmatrix} \vec{\mathbf{a}}_{x'} \cdot \vec{\mathbf{a}}_x & \vec{\mathbf{a}}_{y'} \cdot \vec{\mathbf{a}}_x & \vec{\mathbf{a}}_{z'} \cdot \vec{\mathbf{a}}_x \\ \vec{\mathbf{a}}_{x'} \cdot \vec{\mathbf{a}}_y & \vec{\mathbf{a}}_{y'} \cdot \vec{\mathbf{a}}_y & \vec{\mathbf{a}}_{z'} \cdot \vec{\mathbf{a}}_y \\ \vec{\mathbf{a}}_{x'} \cdot \vec{\mathbf{a}}_z & \vec{\mathbf{a}}_{y'} \cdot \vec{\mathbf{a}}_z & \vec{\mathbf{a}}_{z'} \cdot \vec{\mathbf{a}}_z \end{bmatrix}. \tag{4.5} $$

Now, let us define a plane wave in the direction of z'-axis. As it is stated, at any instant, the magnitude and phase of $\mathbf{E}$ and $\mathbf{H}$ are constant on the plane perpendicular to the direction of propagation. Hence, the electric and magnetic fields must have components in the directions parallel to the plane. For that reason, electric and magnetic fields are defined in x' and y' axes, respectively. The resulting waveform is

$$ \mathbf{E}^0 = \vec{\mathbf{a}}_{x'} E^0_{x'}, \tag{4.6} $$

$$ \mathbf{H}^0 = \vec{\mathbf{a}}_{y'} H^0_{y'}. \tag{4.7} $$

Note that the constants has a phase related to the propagation axis, which means that they are a function of the position in direction of propagation. As a result of this, the constants can be rewritten as a function of z', such as $E^0_{x'}(z') = \tilde{E}^0_{x'} e^{-jkz'}$. Note that the direction is assumed to be in $+z'$, not $-z'$. A general form can be written as $E^0_{x'}(z') = \tilde{E}^{0+}_{x'} e^{-jkz'} + \tilde{E}^{0-}_{x'} e^{+jkz'}$. But for convenience, only the fields in the direction of $+z'$ is considered.

We can generalize (4.6) and (4.7) for any time and point in the direction of propagation:

$$ \begin{aligned} \mathbf{E}(z', t) &= \vec{\mathbf{a}}_{x'} \mathrm{Re}\{E^0_{x'}(z') e^{jwt}\} \\ &= \vec{\mathbf{a}}_{x'} \mathrm{Re}\{\tilde{E}^0_{x'} e^{j(wt - kz')}\} \\ &= \vec{\mathbf{a}}_{x'} |\tilde{E}^0_{x'}| \cos(wt - kz' + \angle \tilde{E}^0_{x'}). \end{aligned} \tag{4.8} $$

$$ \begin{aligned} \mathbf{H}(z', t) &= \vec{\mathbf{a}}_{y'} \mathrm{Re}\{H^0_{y'}(z') e^{jwt}\} \\ &= \vec{\mathbf{a}}_{y'} \mathrm{Re}\{\tilde{H}^0_{y'} e^{j(wt - kz')}\} \\ &= \vec{\mathbf{a}}_{y'} |\tilde{H}^0_{y'}| \cos(wt - kz' + \angle \tilde{H}^0_{y'}). \end{aligned} \tag{4.9} $$

Note that electric and magnetic field, and the direction of propagation are perpendicular to each other. Up to that point, the electric and magnetic fields are written independently of each other in the wave equations. However, it is known from Maxwell's equations that both electric and magnetic fields are related to each other. Describing electric and magnetic flux as $\mathbf{D} = \epsilon\mathbf{E}$ and $\mathbf{B} = \mu\mathbf{H}$ respectively, the Maxwell equations in differential form which relate electric and magnetic field:

$$\nabla \times \mathbf{E} = -\frac{\partial}{\partial t}\mathbf{B} \tag{4.10}$$

$$\nabla \times \mathbf{H} = \mathbf{J} + \frac{\partial}{\partial t}\mathbf{D}, \tag{4.11}$$

where $\mathbf{J}$ is the volume current density, which is zero in free space. Again assuming that the electric field is in $\vec{\mathbf{a}}_{x'}$ direction and the magnetic field is in $\vec{\mathbf{a}}_{y'}$, the relation can be written as:

$$\mathbf{H} = \vec{\mathbf{a}}_{y'} H_{y'}(z') = \vec{\mathbf{a}}_{y'} \frac{k}{w\mu} E_{x'}(z'). \tag{4.12}$$

In the relation between electric and magnetic field given in (4.12), we define intrinsic impedance υ as,

$$\upsilon = \sqrt{\mu/\epsilon}. \tag{4.13}$$

The intrinsic impedance of the air is $\upsilon_0 = \sqrt{\mu_0/\epsilon_0} = 120\pi$.

Another critical topic is the polarization of an electromagnetic wave. The electric and magnetic can be expressed by orthogonal components defined in the plane perpendicular to the direction of propagation. The polarization can be described by the orientation angle ϑ, and the ellipticity angle φ, [63]:

$$\boldsymbol{\kappa} = \begin{bmatrix} \cos\vartheta & -\sin\vartheta \\ \sin\vartheta & \cos\vartheta \end{bmatrix} \begin{bmatrix} \cos\varphi \\ j\sin\varphi \end{bmatrix} \tag{4.14}$$

The polarization is a 2×1 vector since it represents the amplitude and phase difference of the signal in horizontal and vertical plane, $\boldsymbol{\kappa} = [\kappa_H, \kappa_V]^T$. The ellipticity angle can be defined as the tangent of the fraction of the wave amplitude minor axis and the wave amplitude in the major axis, and the orientation angle is the counterclockwise angle from the original plane [63]. Hence, to cover any possible state, the boundaries are set to $\vartheta \in (-\pi/2, \pi/2]$ and $\varphi \in [-\pi/4, \pi/4]$.

Interpreting these definitions, if $\vartheta = 0$, $\tan\varphi$ gives the ratio between the magnitudes of the field in the vertical plane and the horizontal plane of a field. Note that this ratio is not the polarization angle but the ratio of the magnitude of both electric and magnetic fields. Also, note that if $\varphi = 0$, the wave has linear polarization and has circular polarization otherwise. For example, $\varphi > 0$ result in right-hand circular polarization and $\varphi < 0$ result in left-hand circular polarization.

After following the basics of electromagnetic plane waves, we will introduce concepts related with antenna radiation and reception. A critical concept that provides functional description of an antenna is the antenna pattern. The antenna pattern of an antenna is a measurement of relative power at a fixed far-field distance as a function of azimuth and elevation angle, [64]. The calculation of antenna pattern is calculated by the average power inside a unit area times the distance r:

$$G_D(\theta, \phi) = \frac{U(\theta, \phi)}{P_r/4\pi} = \frac{4\pi U(\theta, \phi)}{\oint U(\theta, \phi)\sin(\theta) d\theta d\phi} \tag{4.15}$$

where $G_D(\theta, \phi)$ is the antenna gain as a function of θ and ϕ, $U(\theta, \phi) = r^2 P_{av}$ is the average power at at the distance r where P_{av} is the average power.

Although there are many antenna types, we will only consider a few antenna types suitable for use in a MIMO radar system. Dipole antennas are commonly used in MIMO systems. Typically dipole antennas has thin linear structures that is generally fed by a source from its center. The antenna pattern of a linear dipole antenna is: [64]:

$$\mathbf{E}_{dipole}(\theta) = \frac{j60 I_0}{R_0} e^{-j2\pi R_0/\lambda} \frac{\cos\left(\frac{2\pi h_{dipole}}{2\lambda}\cos(\theta)\right) - \cos\left(\frac{2\pi h_{dipole}}{2\lambda}\right)}{\sin(\theta)}, \tag{4.16}$$

where h_{dipole} is the length of the antenna, I_0 is the peak current at the feed of the antenna, and R_0 is the distance between the measurement point and the feed of the antenna. Note that since the structure of the antenna is symmetric in the azimuth, the pattern is isotropic in azimuth direction. Since the antenna structure is fixed according to azimuth. Because of that reason, dipole antennas are suitable to be used in MIMO radar systems with widely separated antennas so that each receiver can receive reflected signals from all azimuth directions.

Besides dipole antenna, loop antennas are also useful and essential antennas. Loop antennas can be separated into two classes, large (resonant) and small (magnetic) loop antennas, [65]. The terms large and small define the size of the antenna with respect to the interested wavelength. The radius of a large loop equals the resonant frequency wavelength. This type is advantageous to receive signals in a specified frequency.

On the other hand, magnetic loop antennas have a radius much smaller than the specified wavelength. This results in a change in the antenna pattern. A magnetic loop antenna responds to the magnetic flux passing through the plane of the loop. Because of that reason, the pattern of the magnetic loop antenna is similar to the dipole antenna pattern, where the response is small in the direction perpendicular to the antenna plane and large in the plane of propagation. As a result, we can say that dipole and magnetic loop antennas are suitable to measure electric and magnetic fields, respectively. Hence, they can be used together to measure polarization and bring extra features by positioning and selecting the sizes appropriately.

Electric and magnetic fields are perpendicular to the direction of propagation. Hence, the polarization is applied to both fields. Therefore, it is possible to detect the direction and polarization of an impinging wave with a suitable antenna structure. Dipole and magnetic loop antennas are appropriate to such applications. To achieve this goal, the idea of the Electromagnetic Vector Sensor (EMVS) emerged.

Recently, the invention of an antenna called Electromagnetic Vector Sensor (EMVS), [2] has become a milestone for MIMO radar systems. The first EMVS-based MIMO radar is proposed in [66]. Since then, EMVS MIMO radar has been an intense research area. Recent studies on EMVS-based bistatic MIMO radar systems, [67, 68, 69, 70, 71, 72], show that EMVS is suitable for MIMO radar applications, and its usage is investigated in recent literature.

The impinging wave to EMVA can be considered a plane electromagnetic wave since the source of the wave is at a distance much larger than the half wavelength. Moreover, by using three orthogonal antenna for both electric and magnetic field, The response for any direction is unique. It is convenient to use spherical coordinate system since the direction of propagation can be defined by $\hat{\mathbf{r}}$. Hence, for any azimuth angle ϕ and elevation angle θ which is defining the direction of propagation, the electric and magnetic field has same magnitude and phase on the plane perpendicular to $\vec{\mathbf{r}}$, [60, 73]:

$$\mathbf{E} = \sin\gamma e^{j\eta}\vec{\mathbf{a}}_\phi + \cos\gamma\vec{\mathbf{a}}_\theta \tag{4.17}$$

$$\mathbf{H} = \upsilon\left(\cos\gamma\vec{\mathbf{a}}_\phi + \sin\gamma e^{j\eta}\vec{\mathbf{a}}_\theta\right), \tag{4.18}$$

where γ is polarization angle and η is polarization phase difference.

Converting spherical coordinate to Cartesian coordinate system and defining each component on a vector, spatial response of a EMVA as electric and magnetic field is

$$\mathbf{c}(\theta, \phi, \gamma, \eta) = \mathbf{Q}(\theta, \phi)\boldsymbol{\varepsilon}, \tag{4.19}$$

where $\mathbf{c} = [\mathbf{E}^T, \mathbf{H}^T]^T$, $\mathbf{E} = [E_x, E_y, E_z]^T$ representing the electric field vector and $\mathbf{H} = [H_x, H_y, H_z]^T$ representing the magnetic field vector, $\mathbf{Q}$ is the produced response of an EMVA, [60]:

$$\mathbf{Q}(\theta, \phi) = \begin{bmatrix} \cos\theta\cos\phi & -\sin\phi \\ \cos\theta\sin\phi & \cos\phi \\ -\sin\theta & 0 \\ -\sin\phi & -\cos\theta\cos\phi \\ \cos\phi & -\cos\theta\sin\phi \\ 0 & \sin\theta, \end{bmatrix} \tag{4.20}$$

and the polarization vector $\boldsymbol{\varepsilon}$ defined for spatial response,

$$\boldsymbol{\varepsilon} = \left[\sin\gamma e^{j\eta}, \cos\gamma\right]^T. \tag{4.21}$$

Note that both (4.14) and (4.21) represents polarization of the wave. However, (4.21) is the special case arranged to apply on (4.20). The orientation angle and ellipticity angle can be determined by the polarization angle and polarization phase difference by poincare sphere. In other words, there is unique reversible transformation from (ϑ, φ) to (γ, η), [74].

The azimuth and elevation angles are commonly called as two dimensional Direction-of-arrival or direction-of-departure (2D-DOA/2D-DOD). In order to avoid confusion, we will refer to 2D-DOA and 2D-DOD as DOA and DOD respectively since we only study three dimensional space.

Because of the reason that each element in EMVA is spatially orthogonal, there is a direct relation between DOA/DOD and spatial response $\mathbf{c}(\theta, \phi, \gamma, \eta)$. DOA and DOD can be defined by the poynting vector, which is defined as:

$$\begin{aligned} \mathbf{u} &= \frac{\mathbf{E}}{\|\mathbf{E}\|} \times \frac{\mathbf{H}^*}{\|\mathbf{H}\|} \\ &= [\sin\theta\cos\phi, \sin\theta\sin\phi, \cos\theta]. \end{aligned} \tag{4.22}$$

Conventional MIMO radar systems can benefit from waveform diversity, [12]. Waveform diversity is achieved by effectively designing waveforms from limited sources, [75]. For instance, in MIMO radar systems, waveform diversity is achieved by designing orthogonal waveform for each transmitter on limited bandwidth and energy. On the other hand, if the elements are separated enough, it also benefits from spatial diversity gain, which is achieved by using the spatial properties of the radar to estimate the target properties, [12]. By taking the benefits of MIMO radars and EMVS, EMVS-MIMO can exploit better DOA, polarization estimation, and target localization.

Most of the localization systems for EMVS-MIMO radar systems proposed in the literature are based on DOA and/or DOD estimation. One of the most important work on DOA and polarization estimation is given in [73]. In this work, for only one EMVS, DOA and polarization estimation based on ESPRIT algorithm is proposed. This method is the source of many EMVS based systems, including the EMVS-MIMO radar systems. The main goal of EMVS-MIMO is to estimate targets parameters, such as DOA, DOD and polarization. To do that, most of the studies focus on development of an EMVS-MIMO radar system by modifying and improving the technique proposed in [73] for multiple EMVA geometries. In the rest of this chapter, such studies in the literature will be examined. The development stages will be explained and compared with the older systems.

In the early stages, one of the most significant work on EMVS-MIMO is given in [66]. In the paper, a localization scheme for a MIMO radar with each element is an EMVA is proposed. The system has M number of transmit EMVAs. Let us define the position of m^{th} transmitter as $\mathbf{p}_m = [x_m, y_m, z_m]$ and the direction that the antenna pointing towards $(\theta_{t_m}, \phi_{t_m})$.

The transmitter controls the polarization of the transmitted signal by a 6×1 weight function $\mathbf{w}_m$. The m^{th} transmitter's signal is then transmitted from the EMVA with desired polarization as follows:

$$\mathbf{x}_m(t) = \mathbf{Q}^T(\theta_{t_m}, \phi_{t_m})\mathbf{w}_m s_m(t). \tag{4.23}$$

By using the weights, the polarization of the signal is determined as

$$\boldsymbol{\varepsilon} = \mathbf{Q}^T(\theta_{t_m}, \phi_{t_m})\mathbf{w}_m. \tag{4.24}$$

In [66], a case of single receiver is examined. Assuming that the polarization of each transmitter is the same and there are R number of targets in the far-field, the received signal can be modelled:

$$\mathbf{y}(t;p) = \sum_{i=1}^{R} \sigma_i(p)\mathbf{Q}(\theta_i, \phi_i)\boldsymbol{\zeta}_i\boldsymbol{\varepsilon}\boldsymbol{\alpha}^T(\theta_i, \phi_i)\mathbf{s}(t) + \mathbf{n}(t;p), \tag{4.25}$$

where $\sigma_i(p)$ is the i^{th} target's reflection at p^{th} time, $\boldsymbol{\zeta_i}$ is the i^{th} target's 2×2 scattering matrix, $\boldsymbol{\alpha}(\theta_i, \phi_i)$ contains the phases of the transmitted signals that reflected from the i^{th} target.

By using $L \geq R$ number of pulses, the DOA of each target (θ_i, ϕ_i) can be estimated.

Applying matched filter for each transmit signal, the output of m^{th} signal is:

$$\mathbf{y}_m(p) = \int_0^{T_{\text{coh}}} \mathbf{y}(t;p)s_m^*(t)dt. \tag{4.26}$$

The matched filter output can also be expressed as

$$\begin{aligned}\mathbf{y}_m(p) &= \sum_{i=1}^{R} \mathbf{c}_i e^{j2\pi/\lambda \mathbf{p}_m^T \mathbf{u}_i} \sigma_i(p) \\ &= \mathbf{C}\boldsymbol{\Phi}_m \boldsymbol{\sigma}(p),\end{aligned} \tag{4.27}$$

where $\mathbf{C} = [\mathbf{c}_1, ..., \mathbf{c}_R]$ is the array of spatial response of all pulses, $\Phi_k = \text{diag}(e^{j2\pi/\lambda \mathbf{p}_m^T \mathbf{u}_1}, ..., e^{j2\pi/\lambda \mathbf{p}_m^T \mathbf{u}_R})$ is the diagonal matrix created by the phases of all received signals, and $\boldsymbol{\sigma}(p) = [\sigma_1(p), ..., \sigma_R(p)]^T$ is the reflection of all pulses.

From the relation of $y_k(p)$ and $y_l(p)$ to the relation between $\boldsymbol{\Phi}_m$ and $\boldsymbol{\Phi}_l$, ESPRIT algorithm is used to estimate the target locations. The ESPRIT algorithm depends on the covariance matrix constructed by subsets of a signal. In the paper, $y_k(p)$ and $y_l(p)$ are concatenated in order to perform estimation by the covariance matrix of the concatenated signals. Defining $\mathbf{Z}(p) = [y_k^T(p), y_l^T(p)]^T$, the covariance matrix can be determined:

$$\mathbf{R}_{\mathbf{Z}} = \sum_{p=1}^{L} \mathbf{Z}(p)\mathbf{Z}^H(p). \tag{4.28}$$

Assuming that the number of targets R is perfectly known, a unique $R \times R$ full-rank matrix $\mathbf{G}$ exists such that

$$\begin{aligned}\mathbf{F}_k &= \mathbf{C}\boldsymbol{\Phi}_k\mathbf{G} \\ \mathbf{F}_l &= \mathbf{C}\boldsymbol{\Phi}_l\mathbf{G}\end{aligned} \tag{4.29}$$

By using (4.29),

$$\mathbf{F}_l = \mathbf{F}_k\mathbf{G}^{-1}\boldsymbol{\Phi}_k^{-1}\boldsymbol{\Phi}_l\mathbf{G}. \tag{4.30}$$

To estimate the spatial response $\mathbf{C}$, total least square estimation of $\boldsymbol{\Psi}$ is calculated where $\boldsymbol{\Psi} = \mathbf{G}^{-1}\boldsymbol{\Phi}\mathbf{G}$. Here, $\boldsymbol{\Phi} = \boldsymbol{\Phi}_k^{-1}\boldsymbol{\Phi}_l$. The resulting estimation is used in the equation:

$$\hat{\mathbf{C}}\boldsymbol{\Phi}_k = (\mathbf{F}_k\mathbf{G}^{-1} + \mathbf{F}_l\mathbf{G}^{-1}\boldsymbol{\Phi}^{-1})/2 \tag{4.31}$$

To estimate the azimuth and elevation angle of i^{th} target, first, the poynting vector of receiver to the i^{th} target must be estimated. After estimating the poynting vector, azimuth and elevation angle can be estimated by applying geometrical transformations on poynting vectors. By using (4.31), $\hat{\mathbf{c}}_i$ can be estimated by normalizing the i^{th} column of $\hat{\mathbf{C}}\boldsymbol{\Phi}$. Using the estimation $\hat{\mathbf{c}}_i$, poynting vector can be estimated by using (4.22):

$$\begin{bmatrix} \hat{u}_i \\ \hat{v}_i \\ \hat{w}_i \end{bmatrix} = \frac{\hat{\mathbf{E}}_i}{\left\|\hat{\mathbf{E}}_i\right\|} \times \frac{\hat{\mathbf{H}}_{\mathbf{i}}^*}{\left\|\hat{\mathbf{H}}_i\right\|}. \tag{4.32}$$

By using the estimated poynting vector given in (4.32), the azimuth and elevation location of the target can be estimated as

$$\hat{\theta}_i = \sin^{-1}\sqrt{\hat{u}_i^2 + \hat{v}_i^2}, \tag{4.33}$$

$$\hat{\phi}_i = \angle(\hat{u}_i + j\hat{v}_i). \tag{4.34}$$

Even though this system does not impose any restriction to transmitter placement, this system can resolve only up to six target. On the other hand, there is only one receiver used. After the publication of the paper presenting this system, the literature focused on the development of multi-receiver systems. One of the most significant and earliest study on EMVS-MIMO radar system with multiple transmit and receive antenna is given in [76]. In this work, an EMVS-MIMO radar with a number of transmit EMVAs colocated to construct a ULA and a number of receiver EMVAs colocated to construct an ULA is studied. On the other hand, the system can estimate both DOA and DOD.

The system is considered as a bistatic radar in which both transmitter and receiver arrays are considered as phased array antennas. In the system, the transmitter is a ULA with M number of EMVAs and the receiver is a ULA with N number of EMVAs. The spacing between each element is ι_t for transmitter and ι_r for receiver. It is assumed that there are R number of target in the same bistatic range cell. Hence, for the i^{th} target, the corresponding steering vector of the transmitter $\mathbf{a}_{t,i}$, and the receiver $\mathbf{a}_{r,i}$ can be expressed as

$$\mathbf{a}_{t,i} = \boldsymbol{\alpha}_{t,i} \otimes \mathbf{c}_{t,i}(\theta_{t,i}, \phi_{t,i}, \gamma_{t,i}, \eta_{t,i}) \tag{4.35}$$

$$\mathbf{a}_{r,i} = \boldsymbol{\alpha}_{r,i} \otimes \mathbf{c}_{r,i}(\theta_{r,i}, \phi_{r,i}, \gamma_{r,i}, \eta_{r,i}), \tag{4.36}$$

where $\boldsymbol{\alpha}_{t,i}$ and $\boldsymbol{\alpha}_{r,i}$ are the steering vectors where each element corresponds for each EMVA element:

$$\boldsymbol{\alpha}_{l,i} = [1, \alpha_{l,i}, ..., \alpha_{l,i}^{M-1}]^T, \alpha_{l,i} = e^{-j2\pi\iota_l \sin\theta_{l,i}/\lambda}, l = \{t, r\}; i = 1, ..., R.$$

Note that the spatial response of each EMVA in transmitter and in receiver are the same. The reason is that the targets are assumed to be in the far field so that the angular position and the polarization of any target is approximately the same for each element in the array.

Similar to the study in [66], an ESPRIT-like algorithm is implemented on the filtered signal in [76]. But, unlike the first one, in the latter paper, the signal is defined in discrete time each of which is defined by $\mathbf{s_{m_e}}$ which is a $J \times 1$ vector for e^{th} element of the EMVA. Since its defined in discrete time, the energy of the signals equals to its length J. Then, the received signal of p^{th} pulse can be written as

$$\mathbf{Z}(p) = \mathbf{A}_r \Lambda_\sigma(p) \mathbf{A}_t^T \mathbf{S} + \mathbf{W}(p), \tag{4.37}$$

where $\mathbf{S} = [\mathbf{S}_1^T \mathbf{S}_M^T]$ is the $6M \times J$ signal matrix in which $\mathbf{S}_m = [\mathbf{s}_{m_1}, ..., \mathbf{s}_{m_6}]^T$, $A_t = [A_{t,1}, ..., A_{t,R}]$ and $A_r = [A_{r,1}, ..., A_{r,R}]$ are the steering vector matrices of all targets, $\Lambda_\sigma(p) = \mathrm{diag}(\sigma_1(p), ..., \sigma_R(p))$ is the matrix of RCS of all targets, $\mathbf{W}(p)$ is the $6N \times J$ noise matrix at p^{th} pulse time.

The received signal is matched filtered with $\mathbf{S}^H/\sqrt{J}$:

$$\mathbf{Y}(p) = \sqrt{J}\mathbf{A}_r \Lambda_\sigma(p) \mathbf{A}_t^T + \frac{1}{\sqrt{J}} \mathbf{W}(p) \mathbf{S}^H. \tag{4.38}$$

To apply a modified version of ESPRIT algorithm, still, the covariance matrix of two vector-type signal must be constructed. However, in (4.38), the received signal is modelled as a matrix. We need to vectorize the received signal:

$$\begin{aligned} \mathbf{y}(p) &= \mathrm{vec}(\mathbf{Y}(p)) \\ &= \mathbf{A}\tilde{\sigma}(p) + \mathbf{w}(p), \end{aligned} \tag{4.39}$$

where $\mathbf{A} = \mathbf{A}_t \boxtimes \mathbf{A}_r$ in which $\boxtimes$ defines Khatri-Rao product, $\tilde{\sigma}(p) = \sqrt{J}[\sigma_1(p), ..., \sigma_R(p)]^T$, and $\mathbf{w}(p) = \frac{1}{\sqrt{J}} \mathrm{vec}\left(\mathbf{W}(p)\mathbf{S}^H\right)$.

The covariance matrix is defined by the vectorized output:

$$\begin{aligned}\mathbf{R_y} &= E[\mathbf{y}\mathbf{y}^H] \\ &= \mathbf{A}\mathbf{R}_\sigma\mathbf{A}^H + \mathbf{R_w}\end{aligned} \tag{4.40}$$

where $\mathbf{R}_\sigma = E[\tilde{\sigma}\tilde{\sigma}^H]$ is the covariance matrix of the targets RCS, and $\mathbf{R_w}$ is the noise covariance matrix.

Since there is only L number of observations, the covariance matrix can be estimated as:

$$\hat{\mathbf{R}}_\mathbf{y} = \frac{1}{L}\sum_{p=1}^{L}\mathbf{y}(p)\mathbf{y}^H(p) \tag{4.41}$$

The proposed DOA and DOD estimation is a similar solution to the technique proposed in [73]. However, the system in [76] is an advanced version for multiple EMVA case. Assuming that the number of target R is correctly estimated, $\mathbf{c}_{r,i}$ and $\mathbf{c}_{t,i}$ can be estimated by eigendecomposition of $\hat{\mathbf{R}}_\mathbf{y}$, like in [76]. By eigendecomposing the covariance matrix $\mathbf{R_y}$, The signal-subspace matrix $\mathbf{F}_s$ with size $36MN \times R$ can be calculated.

There exists a unique $R \times R$ matrix H that leads to the signal-subspace matrix from A, mathematically speaking,

$$\mathbf{F}_s = \mathbf{A}\mathbf{H}. \tag{4.42}$$

By using $\mathbf{F}_s$, both DOA and DOD can be estimated. The estimation of DOA and DOD can be performed by dividing $\mathbf{A}$. This division process is totally linear. For DOA and DOD, different separations are applied.

To estimate DOA, hence $\hat{\mathbf{c}}_{\mathbf{r_i}}$, (4.42) is divided into two parts by applying linear operations:

$$\mathbf{F}_{U,r} = \mathbf{\Omega}_{U,r}\mathbf{\Omega}_{P,r}\mathbf{F}_s = \mathbf{A}_{U,r}\mathbf{G}_c, \tag{4.43}$$

$$\mathbf{F}_{L,r} = \mathbf{\Omega}_{L,r}\mathbf{\Omega}_{P,r}\mathbf{F}_s = \mathbf{A}_{L,r}\mathbf{G}_c, \tag{4.44}$$

where the selection matrices are defined as

$$\mathbf{\Omega}_{P,r} = \left[\mathbf{0}_{6N\times 6iN}|\mathbf{I}_{6N}|\mathbf{0}_{6N\times(36MN-6(i+1)N)}\right], \tag{4.45}$$

$$\mathbf{\Omega}_{U,r} = \left[\mathbf{I}_{6(N-1)}|\mathbf{0}_{6(N-1),6}\right], \tag{4.46}$$

$$\mathbf{\Omega}_{L,r} = \left[\mathbf{0}_{6(N-1),6}|\mathbf{I}_{6(N-1)}\right], \tag{4.47}$$

in which $i = 0, ..., 6M-1$ is the selection of index.

Moreover, since $\mathbf{F}_{U,r}$ and $\mathbf{F}_{L,r}$ are full-rank, there exists a unique $R \times R$ matrix $\mathbf{\Phi}_r$ such that

$$\mathbf{F}_{L,r} = \mathbf{F}_{U,r}\mathbf{\Phi}_r. \tag{4.48}$$

From (4.44), we know that $\mathbf{A}_{L,r}\mathbf{G}_c = \mathbf{A}_{U,r}\mathbf{\Lambda}_{\alpha_r}\mathbf{G}_c$ where $\mathbf{\Lambda}_{\alpha_r} = \text{diag}(\boldsymbol{\alpha_r})$. From that equation and (4.48),

$$\mathbf{\Phi}_r = \mathbf{G}_c^{-1}\mathbf{\Lambda}_{\alpha_r}\mathbf{G}_c. \tag{4.49}$$

Hence, the matrix $\mathbf{A}_{U,r}$ can be derived in two ways:

$$\mathbf{A}_{U,r} = \mathbf{F}_{U,r}\mathbf{G}_c^{-1} \tag{4.50}$$

$$= \mathbf{F}_{L,r}\mathbf{G}_c^{-1}\mathbf{\Lambda}_r^{-1}. \tag{4.51}$$

Therefore, the EMVA components $\hat{\mathbf{c}}_{r,i}$ can be estimated, hence the poynting vectors and DOAs can be estimated by using (4.32)-(4.34).

To estimate the DOD angles, a very similar process is applied. Only the selection matrices are different:

$$\mathbf{F}_{U,t} = \mathbf{\Omega}_{U,t}\mathbf{\Omega}_{P,t}\mathbf{F}_s = \mathbf{A}_{U,t}\mathbf{G}_t, \tag{4.52}$$

$$\mathbf{F}_{L,t} = \mathbf{\Omega}_{L,t}\mathbf{\Omega}_{P,t}\mathbf{F}_s = \mathbf{A}_{L,t}\mathbf{G}_t, \tag{4.53}$$

where the selection matrices are defined as

$$\mathbf{\Omega}_{P,t} = \left[\mathbf{0}_{6M\times 6iM}|\mathbf{I}_{6M}|\mathbf{0}_{6M\times(36MN-6(i+1)M)}\right], \tag{4.54}$$

$$\mathbf{\Omega}_{U,t} = \left[\mathbf{I}_{6(M-1)}|\mathbf{0}_{6(M-1),6}\right], \tag{4.55}$$

$$\mathbf{\Omega}_{L,t} = \left[\mathbf{0}_{6(M-1),6}|\mathbf{I}_{6(M-1)}\right], \tag{4.56}$$

in which $i = 0, ..., 6M-1$ is the selection of index. The remaining process is the same. Hence, poynting vector of transmitter array and DOD angles can be estimated similarly. Even though this system can estimate both DOA and DOD, each DOA and DOD estimates must be paired. This can be obtained by minimizing the steering vector difference corresponding for a DOA and DOD pair.

A later work given in [70] uses the same technique proposed in [76] to estimate DOA and DOD. But, in addition to DOA and DOD estimation, a technique to estimate two dimensional transmit and receive polarization angles (2D-TPA, 2D-RPA) is also proposed. Two dimensional polarization parameter is (γ, η). To avoid confusion, we will refer to 2D-TPA and 2D-RPA as TPA and RPA since only three dimensional space is considered.

To estimate TPA and RPA, least squares method is applied using the estimations of spatial response vector, DOA and DOD:

$$\begin{aligned} \hat{\boldsymbol{\varepsilon}} &\triangleq [\hat{\varepsilon}_1, \hat{\varepsilon}_2]^T \\ &= \left(\mathbf{Q}^H\left(\hat{\theta}_l, \hat{\phi}_l\right)\mathbf{Q}\left(\hat{\theta}_l, \hat{\phi}_l\right)\right)^{-1}\mathbf{Q}^H\left(\hat{\theta}_l, \hat{\phi}_l\right)\hat{\mathbf{c}}_l, \\ l &= \{t, r\} \end{aligned} \tag{4.57}$$

By using (4.14), γ and η can be estimated as

$$\hat{\gamma}_l = \tan^{-1}\left(\frac{|\hat{\varepsilon}_1|}{\hat{\varepsilon}_2}\right) \tag{4.58}$$

$$\hat{\eta}_l = \angle\left(\frac{\hat{\varepsilon}_1}{\hat{\varepsilon}_2}\right). \tag{4.59}$$

Additionally, the system has similar DOA and DOD pairing process as in [76]. Although this pairing process is easy to demonstrate, the pairing process increases computational complexity of the system significantly.

To localize the targets without pairing DOA and DOD, a direction estimation algorithm without the need of pairing is proposed in [68]. To eliminate the pairing process, this system reorganizes the estimation process. First, the elevation angles of DOD and DOA are estimated and are automatically paired. Same process is performed for the azimuth angles. After that, TPA and RPA are estimated similar to the technique proposed in [70]. The notation and the definition of the problem given in this work is the same as in [76]. Therefore, the proposed algorithm in [68] is the faster solution for the same problem given in [76] and [70].

Note that from that point, the surveyed studies assume that all of the targets are in the same bistatic range cell. However, in conventional MIMO radar systems, target detection and positioning mostly depend on bistatic range measurements. As a result, it can be said that EMVS-MIMO radar systems should provide delay estimation to exploit the conventional MIMO radar features. Considering this, some EMVS-MIMO systems for delay estimation are studied in literature, such as in [77, 78].

The delay estimation in [77] and [78] is performed by MUSIC algorithm applied to the received signal in frequency domain. Additionally, in [77] the elements of each EMVA is separated to improve the performance. For simplicity, the delay estimation proposed in [78] is investigated.

In this work, The parallel factor decomposition (PARAFAC) is developed for delay and DOA estimation. A multipath environment is considered. The case where R number of rays is considered. The scatters in this work can be treated as targets. The received signal of i^{th} target is parametrized with $\tau_i, \phi_i, \theta_i, \sigma_i$ which are the delay, azimuth angle of DOA, elevation angle of DOA and the RCS of the target respectively. The spatial response for i^{th} target is modeled as

$$\mathbf{c}_i = \sigma_i \mathbf{Q}(\theta_i, \phi_i)\boldsymbol{\varepsilon} \tag{4.60}$$

Hence, the received signal can be expressed in frequency domain as

$$\mathbf{Z} = \mathbf{CFS} + \mathbf{W}, \tag{4.61}$$

where $\mathbf{C} = [\mathbf{c}_1, ..., \mathbf{c}_R]$, $\mathbf{F}$ is the $R \times N$ phase shifting matrix in which N is the number of DFT samples and each element $\mathbf{F}_{i,n} = e^{-j2\pi f_n \tau_i}$, $\mathbf{S} = \text{diag}(s(f_1), ..., s(f_N))$ is the transmitted signal in frequency domain defined in diagonal matrix, and $\mathbf{W}$ is the noise. After matched filtering, the response of the targets is estimated.

$$\hat{\mathbf{Y}} = \mathbf{Z}\mathbf{S}^{\mathbf{-1}} \tag{4.62}$$

To estimate delay, PARAFAC algorithm is used. To perform delay estimation using PARAFAC algorithm, first, trilinear factor model must be constructed. For that reason, by using the estimaion $\hat{\mathbf{Y}}$, P number of submatrices are constructed each of which contains $(N - P + 1)$ number of frequency bins. By adjoining the submatrices, a three dimensional matrix $\underline{\mathbf{Y}}$ with size $6 \times (N - P + 1) \times P$ is constructed. Performing PARAFAC decomposition on the matrix, the matrix $\mathbf{\Phi}$ each element of which $[\mathbf{\Phi}]_{p,k} = \exp\left(-j2\pi(p-1)\Delta f \tau_k\right)$ is estimated.

Let $\mathbf{F}_n$ be the matrix of $P \times (P-R)$ whose columns are eigenvectors corresponding to $P-R$ small eigenvalues of the covariance matrix $\mathbf{R}_{\mathbf{\Phi}} = \mathbf{\Phi\Phi}^H$. Performing the pseudospectrum MUSIC estimation, the delay estimation can be defined as

$$P_{MUSIC}(\tau) = \frac{1}{\mathbf{v}(\tau)\mathbf{F}_n\mathbf{F}_n^H\mathbf{v}^H(\tau)}, \tag{4.63}$$

where

$$\mathbf{v}(\tau) = \left[1, e^{-j2\pi\Delta f\tau}, ..., e^{-j2\pi(P-1)\Delta f\tau}\right]. \tag{4.64}$$

Note that the proposed system in related article is for one receiver. In [77], the system in [78] is revised for multiple receiver EMVSs. On the other hand, each EMVA is reconstructed by separating each element from the center by a small amount.

As it is known, the effective aperture of an antenna array depends on the distance between the elements. Hence in ULA configuration, this distance cannot be greater than half a wavelength. Additionally, mutual coupling cannot performance decreases, and may lead to failure of the system when the distance between the element is small. To overcome the mentioned problems, an antenna configuration which uses coprime numbers for spacing the elements of the antenna arrays is proposed in [79].

In the following studies, an new concept called coprime EMVS-MIMO is proposed. Some of the remarkable works on coprime EMVS-MIMO are given in [80, 72, 81, 69]. Coprime EMVS-MIMO radar systems consist of linear transmit and receiver array whose antennas are are EMVAs and has specific specific spacings. The transmit array has M element with spacing $N\lambda/2$, and the receiver array has N element with spacing $M\lambda/2$ where M and N are coprime numbers. Note that each element is a EMVA, which has six components. From the fact that the spacing of the transmitter and receiver is larger than half of wavelength, the aperture of both array are larger than the transmitter and receiver array in other EMVS-MIMO radar systems.

Consequently, EMVS is compatible with MIMO radar systems, and such applications are in the interest of the literature. However, only EMVS-MIMO radar systems with bistatic (transmit antennas and receive antennas are colocated) and monostatic geometry is studied in the literature. In this thesis, we will study EMVS-MIMO radar systems with multistatic geometry (each transmit and receive antennas are widely separated).

4.4 Detection of Target in MIMO Radar Systems

The ability to observe moving targets in a wide angular sector is an important advantage of MIMO radars. It is vital for the detection of moving targets to observe them at different angles that are difficult to separate from clutter signals due to a possible low radial velocity. On the other hand, generating a unique signal for each point on the grid increases computational complexity considerably. To perform detection without encountering these problems, a novel distributed MIMO radar detection technique is proposed in this section of the thesis.

As in the detection scheme proposed in [12], in the region of interest (ROI), a grid of possible positions where the target can be found is created. In the case studied in this section, there is a moving target in the detection zone. In the two- and three-dimensional system, the position of the moving target when examined in two-dimensional space $\boldsymbol{P}_{tgt} = [x\ y]^T$, its speed $\boldsymbol{v}_{tgt} = [v_x\ v_y\ ]^T$, its position when viewed in three-dimensional space $\boldsymbol{P}_{tgt} = [x\ y\ z]^T$, speed $\boldsymbol{v}_{tgt} = [v_x\ v_y\ v_z]^T$ assumes the number of transmitters is M and the number of receivers is N. In this case, there are $M \times N$ views between the receivers and transmitters. The transmitters are expressed as $T_k, 1 \leq k \leq M$, and the receivers as $R_l, 1 \leq l \leq N$. This scheme is shown in Fig. 3.9.

A likelihood ratio test has been proposed for target detection in a cell located in the grid. The likelihood ratio here can be obtained using different parameters. The bistatic ranges obtained by the cells can be compared with the measured bistatic range. The other option is to compare the measured bistatic range and

Doppler with bistatic range and Doppler obtained by the position of the cells and some velocity vectors generated at that location.

The relationship of the interested cell location with the bistatic range measurement of the relevant transmitter-receiver pair is studied in two ways. The first is the minimum distance of the cell location to the ellipse corresponding to the measured bistatic range around the base of the transmitter-receiver pair, and the other is the difference between the bistatic range of the cell location for the transmitter-receiver pair and the measured bistatic range. The former may vary with the proximity of the cell to the transmitter or receiver. As a result of the analyses, it is observed that this variability can make a difference in systems in two-dimensional space, it creates a negligible difference in the system in three-dimensional space, and the measurement of the minimum distance of a point from an ellipsoid in three-dimensional space creates a lot of computational load on the system. Therefore, the minimum distance of the point to the ellipse in two-dimensional cases, and the bistatic range difference in three-dimensional cases are used.

Target detection was carried out in two ways and performance analyzes were carried out for both cases. These two options are the target detection and position estimation using bistatic range, and target detection and position and velocity estimation using bistatic range and Doppler. The second technique is obtained by creating a grid in the velocity space in addition to the former system. These two systems and a more efficient algorithm that can be used with these systems are presented in detail below.

4.4.1 Bistatic Range based Target Detection

An important issue in target detection is that number of targets in the relevant search area is unknown. In addition, when it is not known which bistatic range measurement belongs to which target, incorrect measurement matching may lead to position estimation incorrectly or not at all. Considering these two criteria, a likelihood ratio test is proposed. Since the instant target number and positions are not known, cells are created at a regular interval in the relevant search area (in a grid shape). Tightening these cells increases the number of cells in the relevant region, and therefore, the processing load can be brought to unacceptable levels. To lower the computational load, target detection is done in two steps.

First, a coarse grid is created in the relevant region. The coarse grid referred to here represents widely spaced cells across ROI. As mentioned above, two different dissimilarity definitions can be made for the cell in the $\boldsymbol{P}$ position to determine it in two or three dimensional space:

$$d\left(\boldsymbol{P};k,l\right)=\begin{cases}\left\|\boldsymbol{P}-\hat{\boldsymbol{P}}_{min}\left(k,l\right)\right\|, & \text{for 2 dimensional case}\\ \mid\rho\left(\boldsymbol{P};k,l\right)-\hat{\rho}\left(k,l\right)\mid, & \text{for 3 dimensional case}\end{cases}\tag{4.65}$$

Here, $\hat{\rho}\left(k,l\right)$ is the measured bistatic range for k^{th} transmitter and l^{th} receiver, $\hat{\boldsymbol{P}}_{min}\left(k,l\right)$ is the closest point to $\boldsymbol{P}$ on the ellipsoid created by the measured bistatic range, and $\rho\left(\boldsymbol{P};k,l\right)$ is the bistatic range of $\boldsymbol{P}$ for k^{th} transmitter and l^{th} receiver.

For each point $\boldsymbol{P}$ on the grid, $d\left(\boldsymbol{P};k,l\right)$ is calculated. After calculating the dissimilarity for each transmitter-receiver pair for each cell on the grid, a weight for each point is calculated defined as follows:

$$w\left(\boldsymbol{P}\right)=\sum_{k=1}^{M}\sum_{l=1}^{N}e^{-\frac{d\left(\boldsymbol{P};k,l\right)^{2}}{2\sigma^{2}}}.\tag{4.66}$$

The value of σ here is chosen as the distance between cells in the detection space. The weight is inversely proportional to the distance between the point on the grid $\boldsymbol{P}$ and the target. Hence, the weights can be treated as a likelihood function. It should be noted that the system mentioned so far is for situations where there is only one target in the environment and each transceiver pair makes a single bistatic range measurement. When the system here is generalized, the weight $w\left(\boldsymbol{P}\right)$ is generalized as follows:

$$w\left(\boldsymbol{P}\right)=\sum_{k=1}^{M}\sum_{l=1}^{N}\sum_{i=1}^{N_{meas}(k,l)}e^{-\frac{d(\boldsymbol{P};k,l,i)^2}{2\sigma^2}}, \tag{4.67}$$

where $N_{meas}(k,l)$ is the number of measurements for k^{th} transmitter and l^{th} receiver pair, $d\left(\boldsymbol{P};k,l,i\right)$ is the difference between the i^{th} measurement $\hat{\rho}\left(k,l\right)$ and the bistatic range of the point $\boldsymbol{P}$ for the k^{th} transmitter and l^{th} receiver. This value is calculated by using (4.65).

Calculated weights are compared with a certain threshold. A fine grid is opened around the area occupied in space by cells crossing the threshold. The weights for the cells in this grid are calculated and re-threshold, and target detection is made at the points crossing the threshold. In both cases, the threshold is chosen in proportion to the total number of transmitter-receiver pairs. This is because when the ellipses cross over the target position, $d\left(\boldsymbol{P}_{tgt};k,l\right)=0$ which results in $e^{-\frac{d(\boldsymbol{P}_{tgt};k,l)^2}{2\sigma^2}}=1$, hence $w\left(\boldsymbol{P}_{tgt}\right)=M\times N$. The resulting thresholding is defined as follows:

$$w\left(\boldsymbol{P}\right)\underset{H_0}{\overset{H_1}{\gtrless}}\gamma_w MN, \tag{4.68}$$

where $0\leq\gamma_w\leq 1$ is a design constant. If this parameter is chosen close to 1, the probability of detection decreases, hence probability of false alarm also decreases. If this parameter is chosen close to 0, the probability of detection increases, hence probability of false alarm. Additionally, the $w(\boldsymbol{P})$ value will be close to the $M\times N$ at a $\boldsymbol{P}$ point close to the target, and in cases where there are other targets in the environment, the weight may increase as a result of different ellipses passing close to the relevant cell position, thus the probability of detection may also increase. However, as the number of target and transceiver pairs in the environment increases, the number of ellipses created increases, so the intersection points will increase and the probability of false alarms will increase. Receiver and transmitter positions should be well chosen to reduce the false alarm level.

4.4.2 Bistatic Range and Doppler based Target Detection

Since the receivers can jointly estimate bistatic range and Doppler, the bistatic Doppler measurements can also be used in the Detection process with bistatic range. We will explain the detection process using the joint bistatic range and Doppler measurements. This detection scheme is similar to the target detection scheme with bistatic range measurements. We will define a grid in spatial and velocity space and define a weight function to perform detection by thresholding.

To understand the proposed system, it is necessary to understand the bistatic Doppler velocity. Unlike (2.6), it is possible to define the bistatic Doppler velocity more clearly. Bistatic Doppler velocity is the average of the velocity components of the target in the receiver and transmitter directions:

$$v_{bi}\left(\boldsymbol{P}, \boldsymbol{V}; k, l\right) = \frac{v_{t_k}\left(\boldsymbol{P}, \boldsymbol{V}\right) + v_{r_l}\left(\boldsymbol{P}, \boldsymbol{V}\right)}{2} \tag{4.69}$$

where $v_{t_k}\left(\boldsymbol{P}, \boldsymbol{V}\right)$ is the relative speed of a target with velocity vector $\boldsymbol{V}$ at location $\boldsymbol{P}$ to the k^{th} transmitter, and $v_{r_l}\left(\boldsymbol{P}, \boldsymbol{V}\right)$ is the relative speed of the target to the l^{th} the receiver. The relative velocities to the given directions can be found as the projection of the velocity vector of the target on the radar directions. Relative velocity of target to the k^{th} transmitter can be calculated as

$$v_{t_k}\left(\boldsymbol{P}, \boldsymbol{V}\right) = \frac{\boldsymbol{V} \cdot \left(\boldsymbol{P_{t_k}} - \boldsymbol{P}\right)}{\left\|\boldsymbol{P_{t_k}} - \boldsymbol{P}\right\|} \tag{4.70}$$

where $\boldsymbol{P_{t_k}}$ denotes the transmitter position. The relative velocity to receiver v_{r_l} can be calculated similarly.

When bistatic range measurements are used alone, grids are opened in ROI to perform target detection. On the other hand, we create joint grids in velocity domain and the position domain to jointly use bistatic range and Doppler velocity measurements.

Note that created velocity grid is not additional to the spatial grids, yet expands the grid point by adding velocity dimensions. In other words, the number of dimension is doubled by adding the unknown target velocity components to the system parameters. To understand the creation of grid points in position and velocity space, let us consider the creation of grid in only position (spatial) domain. As it is shown in Fig. 3.9, the grid points are created in a way such that any region in ROI is covered by a grid point. Let L_d and σ_d be the length of the ROI and distance between grid points in each space respectively. Hence there will be $(L_d/\sigma_d)^2$ number of grid points created for 2D space. On the other hand, we need to create grid points for possible target positions and velocities. To meet this need, we also create grid of velocities for every spatial point. Let L_v and σ_v be the maximum interested target velocity and magnitude of velocity grid point spaces. In other words, for each velocity direction, the velocity values for each axis is divided into L_v/σ_v number of grids. For example, in v_x, which is the x-axis component of the velocity, the grid is created as $-L_v, -L_v + \sigma_v, \ldots, L_v - \sigma_v, L_v$. Hence, creating grid in spatial and velocity domain will result in $(L_d/\sigma_d)^2(L_v/\sigma_v)^2$ number of grid points total. Thus, two different N-dimensional grids are formed orthogonal to each other, and the resulting grid is created in a $2N$-dimensional space.

For each bistatic range and Doppler measurement, we calculate two dissimilarity values. The first one is for bistatic range only and given in (4.65). The second one is for bistatic Doppler measurement. The latter dissimilarity function defines the difference between the measured bistatic Doppler velocity and the bistatic Doppler velocity of a cell in position and velocity space, which is a specific point in spatial space (x, y, z) and the velocity vector (v_x, v_y, v_z) inside the ROI);

$$v\left(\boldsymbol{P}, \boldsymbol{V}; k, l\right) = \left|v_{bi}\left(\boldsymbol{P}, \boldsymbol{V}; k, l\right) - \hat{v}_{bi}\left(k, l\right)\right| \tag{4.71}$$

Note that the bistatic Doppler velocity is also position-dependent since the bistatic Doppler velocity depends on the direction of the radar to the target. By using the predefined dissimilarity functions, weights are calculated. The weight function in this case is similar to the weight function given in (4.67). The exponential for bistatic range dissimilarity function and bistatic Doppler dissimilarity function are multiplied and summed for each bistatic pair.

$$w\left(\boldsymbol{P},\boldsymbol{V}\right)=\sum_{k=1}^{M}\sum_{l=1}^{N}e^{-\frac{d(\boldsymbol{P};k,l)^2}{2\sigma_d{}^2}}e^{-\frac{v(\boldsymbol{P},\boldsymbol{V};k,l)^2}{2\sigma_v{}^2}}. \tag{4.72}$$

Here, σ_d and σ_v should be selected as the distance between cells of the generated grid in position and velocity spaces, respectively. Finally, Detection is performed by thresholding as it is given in (4.68). Note that coarse and fine grid structure can also be used in this case to reduce computational complexity.

There are some advantages of using bistatic Doppler measurements in detection phase. First, by including the velocity information in the weight calculation, the weights in positions different from the target position will be lower. Unlike the case where only bistatic range information is used, this ensures that the weights in the neighborhoods of the cell where the target is located are low. Since the weights in the neighborhoods are low, using a single threshold will be sufficient for the coarse grid. Then, a fine grid opens within cells $(\boldsymbol{P},\boldsymbol{V})$ that crosses the threshold. Here, the position and velocity domain are thresholded together. Cells in the $\boldsymbol{P}$ position and $\boldsymbol{V}$ velocity crossing the threshold will generate more frequent cells in the position and velocity space. Target detection is made in cells with position and velocity values that exceed the threshold by opening the fine grid. Additionally, unlike the previous system, velocity estimation is also made in addition to the position estimation.

Besides of the advantages, there is a critic disadvantage of including bistatic Doppler measurements in detection process, which is the increase in computational complexity. The number of grid points can become unacceptably high when using bistatic range and Doppler. For example, in the system operating in 2-dimensional space, $N_x \times N_y$ cells are created in the course grid. Here N_x and N_y indicate how many parts the x-axis and y-axis are divided. When the grid is opened in the velocity domain in addition to the spatial domain, a total number of $N_x \times N_y \times N_{v_x} \times N_{v_y}$ grid points are formed. This means that the computational complexity increases $N_{v_x} \times N_{v_y}$ times more. Note that the computational complexity increases more for 3-dimensional case. As a result, we can say that performing detection using bistatic range and Doppler may not be suitable for most of the real-life applications. For that reason, we will not study on bistatic range and Doppler based target detection.

4.4.3 Bistatic Range and DOA based Target Detection

As it is discussed in Section 4.4, target detection system has great computational complexity and can be decreased by using coarse and fine grids. However, using gradual grids may not decrease computational complexity enough to be implemented in real life scenarios. For this reason, a multistatic EMVS-MIMO radar detection system is proposed in this thesis.

In the proposed system, there are M transmitter with dipole antenna, and N receiver with EMVA. The antennas are widely separated for spatial diversity gain. The main difference between the MIMO detection scheme proposed in 4.4 and this detection system using EMVS is that the receivers are capable of estimating DOA in the latter system. Since the receiver can associate a bistatic measurement with a DOA estimation, the system does not have to scan the entire ROI for target detection. Instead, only the region within the detection cone of the corresponding DOA is searched. The detection cone has an angular width that is equal to the standard deviation of the estimation error. The search region is determined by the intersecting regions of the detection cone and two bistatic range ellipsoids that are defined by the measured bistatic range plus and minus the range resolution. Detection is performed on the grid points inside the detection cone.

To understand the system better, let us define the signal model and describe the receiver structure. The signal model is defined similar to the signal model defined in [66] but a generalized formula:

$$\mathbf{y}_l(t) = \sum_{k=1}^{M}\sum_{i=1}^{R} P_r(k,l,i)\mathbf{Q}(\theta_{l,i},\phi_{l,i})\boldsymbol{\varepsilon}_{l,i}\mathbf{s}_k(t-\tau_{k,l,i})e^{-j2\pi f_d t} + \mathbf{n}_l(t), \tag{4.73}$$

where $\mathbf{Q}(\theta_{l,i},\phi_{l,i})$ and $\boldsymbol{\varepsilon}_{l,i}$ are the spatial response matrix and polarization vector of the signal reflected from the i^{th} target, $\tau_{k,l,i} = c/(r_{t_k,i} + r_{r_l,i})$ is the time delay caused by the bistatic range which is the summation of range between k^{th} transmitter and i^{th} target denoted by $r_{t_k,i}$, and range between l^{th} receiver and i^{th}

target denoted by $r_{r_l,i}$, $P_r(k,l,i)$ is the received power which can be calculated by bistatic radar equation by omitting the noise power [82]:

$$P_r(k,l,i) = \frac{P_{t_k} G_{t_k} G_{r_l} \lambda_k^2 \sigma_i(k,l)}{16\pi^2 r_{t_k,i}^2 r_{r_l,i}^2}, \tag{4.74}$$

where P_{t_k} is k^{th} transmitter power, G_{t_k} and G_{r_l} are the k^{th} transmitter and l^{th} receiver antenna gain, λ_k is the wavelength of the k^{th} transmitter. Note that the other loss factors are also omitted for the sake of simplicity.

Each receiver has M number of filter for each transmitter. Note that each receiver has six antenna elements which receive the signal separately. Hence, there must be M number of filter for each element. Therefore, a receiver has $6M$ filters total.

For the sake of simplicity, only one period pulse is examined. Then, matched filter for each element which is represented in vector form can be given as

$$\mathbf{y}_l(\tau; k) = \int_0^{T_{\text{coh}}} \mathbf{y}_l(t+\tau) s_k^*(t) dt. \tag{4.75}$$

The matched filter output can also be presented as

$$\mathbf{y}_l(\tau; k) = \sum_{i=1}^{R} P_r(k,l,i) \mathbf{c}_i e^{j2\pi((\tau - \tau_{k,l,i})/\lambda + f_d t)}. \tag{4.76}$$

Here, $\mathbf{y}_l(\tau; k)$ is a 6×1 vector where each element corresponds to the filter output of corresponding antenna element. By using any suitable TOA and DOA estimation presented in the literature can be used. Note that the Doppler shift is estimated, hence can be removed from the filter output by using PPLFM waveforms. As it is stated in this chapter, TOA estimation of EMVS-MIMO is studied in [77]. However, the proposed TOA estimation is only suitable for colocated receiver antennas which is seen in (4.63) and (4.64). On the other hand, a peak detection can be done on the filter outputs of elements. An integration of signals from each element is performed in each range bin:

$$\mathbf{y}_l(\tau; k)^H \mathbf{y}_l(\tau; k) \underset{H_0}{\overset{H_1}{\gtrless}} \gamma_{plot}, \tag{4.77}$$

where $[\cdot]^H$ denotes the hermitian, and γ_{plot} is the threshold value to detect signal. At the τ values where threshold is exceeded, DOA estimation is performed. To perform DOA estimation, any suitable DOA estimation algorithm can be used, one of which is given in [66]. The DOA estimation algorithm is briefly explained where the estimation is performed from (4.49). For the sake of simplicity, let us define the received signal array as

$$\mathbf{y}_l(t) = \begin{bmatrix} y_{l,D_x} \\ y_{l,D_y} \\ y_{l,D_z} \\ y_{l,M_x} \\ y_{l,M_y} \\ y_{l,M_z} \end{bmatrix},$$

where D_x, D_y, D_z define the dipole antennas in x, y and z axes, and M_x, M_y, M_z define the magnetic loop antennas in x, y and z axes. Hence, the received signal is differentiated to each element. Using this notation, we visualize the receiver scheme for the k^{th} transmitter in Fig. 4.3.

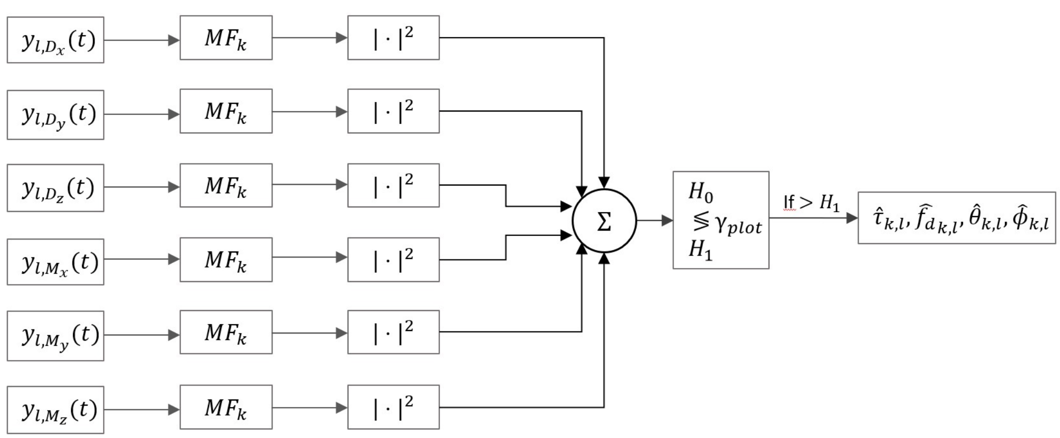

Figure 4.3: Proposed EMVS-MIMO radar receiver structure of the for the i^{th} transmitter signal of the l^{th} receiver. The six signals are obtained from each defined element.

A bistatic measurement with DOA estimation can be performed using the proposed receiver scheme. To perform target detection, we must create a grid of points inside a region defined by the bistatic range and DOA estimations. The region is defined as the volume between the intersections of four lines created by the DOA estimations and its estimation error variances and two ellipsoids created by the bistatic range measurements and bistatic range resolution. The mathematical definition of such region can be written as follows:

$$A_{k,l,i} = \left\{ \boldsymbol{P} \in A_{k,l,i} \middle| \left\{ \begin{array}{c} \hat{\rho}_{k,l,i} - \rho_{\text{res}} < \rho(\boldsymbol{P}; k, l) < \hat{\rho}_{k,l,i} + \rho_{\text{res}}, \\ \hat{\theta}_{l,i} - \sigma_{\text{az}} < \theta(\boldsymbol{P}; l) < \hat{\theta}_{l,i} + \sigma_{\text{az}}, \\ \hat{\phi}_{l,i} - \sigma_{\text{el}} < \phi(\boldsymbol{P}; l) < \hat{\phi}_{l,i} + \sigma_{\text{el}} \end{array} \right. \right\} \tag{4.78}$$

Note that for $N > 1$, there are multiple intersections for a region. Hence, a joint region must be obtained.

To determine the joint areas, first we need to determine the center of each region. The center of a region is the intersection of bistatic range ellipsoid and the vector pointing at the DOA from the receiver. Note that DOA measurements are performed in the receiver's ENU coordinate system. On the other hand, the ellipsoid is defined in the basis line of transmitter and receiver. The steps to find the intersection of ellipsoid and the vector pointing at the DOA are given as follows:

First, a spherical coordinate which is defined in AER coordinate frame with its basis is located at the receiver has the estimated DOA with unit length. The AER coordinate is transformed to ECEF coordinate system and subtracted by the ECEF coordinate of the receiver. The resulting is a unit vector pointing to the measured DOA, which is called DOA vector for the sake of simplicity. To calculate the intersection point, our aim is to extend the length of the DOA vector by the range between receiver and target, and add receiver's position. The receiver range can be calculated by (2.4). To use the equation, ϕ_r must be determined. On the other hand, (2.4) is defined in 2D-space. However, the geometry in the defined problem is in 3D-space. To use (2.4) a plane parallel to the DOA vector and passing through the transmitter and receiver is defined. Since the problem is reduced to two dimensional space, we can use (2.4). it is known that the projection of a vector to any other vector can be defined by the norm of the projected vector and the angle between the two vectors. Let us

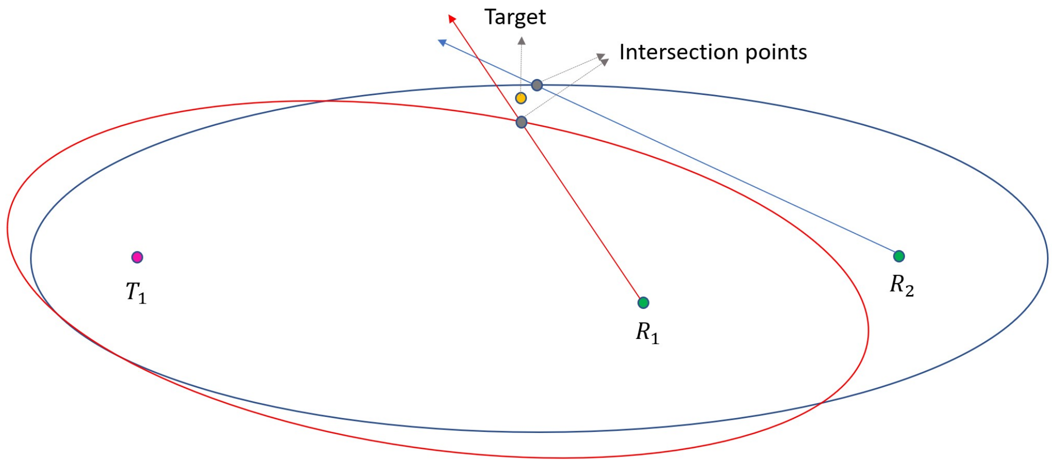

Figure 4.4: Obtained intersection points for two bistatic measurements. Colors indicate the corresponding receiver, straight and dashed lines define the bistatic range regions and the DOA regions, respectively.

define a unit vector at the receiver pointing towards the transmitter, which will be called as base vector for the sake of simplicity. Hence, ϕ_r can be calculated by the projection of DOA vector on base vector:

$$\phi_r = \cos^{-1}\left(\vec{v}_{\text{DOA}} \cdot \vec{v}_{\text{base}}\right), \tag{4.79}$$

where $\vec{v}_{\text{DOA}}$ and $\vec{v}_{\text{base}}$ are the DOA and base vectors respectively. by using ϕ_r in (2.4), r_r is calculated and the intersection point is calculated:

$$P_{\text{is}} = P_r + r_r \vec{v}_{\text{DOA}}.$$

For each bistatic measurement, an intersection point is calculated. The intersection points are illustrated in an example given in Fig. 4.4.

In Fig.4.4, there is only one transmitter and two receiver present in space. From both bistatic pair, a measurement is made. By using the DOA and bistatic range measurements, intersection points are calculated. Note that the intersection points are not on the target position due to the noise in measurements.

Each measurement, which is a combination of bistatic range and receiver DOA estimation, corresponds to a potential target region. Such regions for the example case given in Fig. 4.4 are shown in Fig. 4.5.

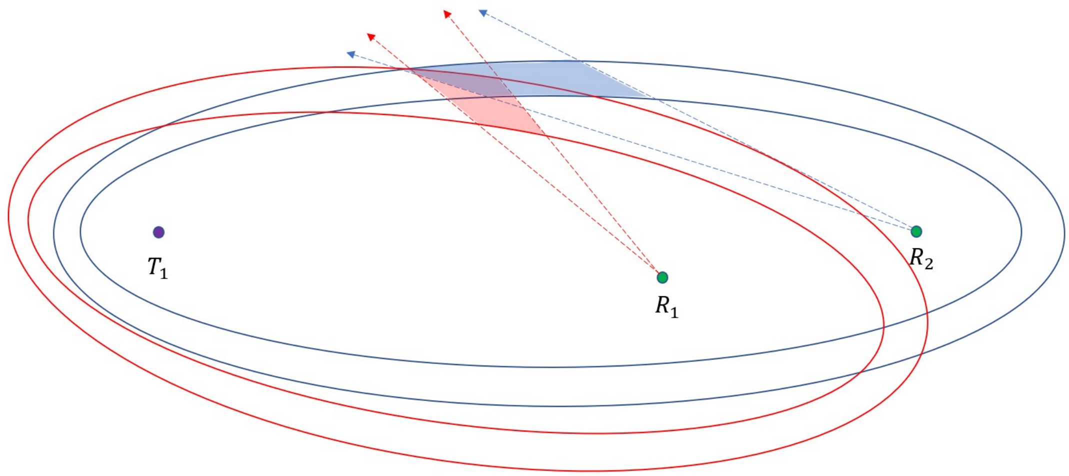

Figure 4.5: Potential target regions obtained by the measurements are shown as the tinted regions. The colors indicate the corresponding receiver, and the straight and dashed lines define the bistatic range regions and the DOA regions respectively.

To perform detection, some grid points must be generated inside each region defined by a bistatic measurement. However, some regions may intersect. In that case, generating a grid for each bistatic measurement can result in duplication of some grid points and performing detection for a point more than once. To overcome duplication, the regions are clustered and a joint grid is generated for any joint region.

To group potential target regions, a matrix D where each element is the distance between two intersection points is calculated.

$$D = \begin{bmatrix} d_{1,1} & \dots & d_{1,L_{\text{is}}} \\ \vdots & \ddots & \vdots \\ d_{L_{\text{is}},1} & \dots & d_{L_{\text{is}},L_{\text{is}}} \end{bmatrix}, \tag{4.80}$$

where L_{is} is the number of intersection points, and $d_{i,j} = \|P_{\text{is},i} - P_{\text{is},j}\|$ is the distance between the i^{th} and j^{th} intersection points respectively. If $d_{i,j}$ is smaller than a specified distance, γ_d, the i^{th} and j^{th} intersections are grouped to create the set $\{i, j\}$. Note that intersection cannot be element of more than one set. For example, let $\{i, j\}$ and $\{j, k\}$ be two sets. Since j is the element of both sets, the sets are combined to create the set $\{i, j, k\}$.

An important point to discuss is that the distance threshold, γ_d should be decided on the system needs. For the cases where the targets are more likely to be in a considerable distance and the high values of variance of the estimation errors of measurements, increasing γ_d will result in better detection performance. On the other hand, for the cases where the targets are likely to be close, and the variance of the estimation errors of measurements to be small, decreasing γ_d will result in better detection performance.

Let's examine an example to better understand the situation. Let us imagine a case where there are two targets present. The intersection points may have occurred far from each other due to the measurement error. If the intersection points obtained from the measurements belonging to the same target are far from each other, the γ_d value should be selected high so that the points belonging to the same group can be grouped. However, in this case, if the targets are close to each other, the measurements belonging to different targets will be grouped as a single set. As a result, a possible target will be missed because the intersection of potential target regions of this group will be too small or no joint region for the specified group will be achieved. On the other hand, decreasing γ_d will result in more than one set for a target which may result in duplication of target detection. As a result, there is a trade-off between missing a target and misdetection. Therefore, γ_d value should be chosen according to system needs. The selection of γ_d is discussed in more detail in the The Results chapter.

For each set, a potential target region is obtained and a grid of points is generated. Let A_i be the region of i^{th} measurement. The region created by set C is the intersection of potential target regions obtained by the measurements inside the set:

$$A_C = \bigcap_{i \in C} A_i. \tag{4.81}$$

Inside the obtained joint region A_C, a grid of points must be generated. However, since the region has nonuniform shape, we generate a large grid with uniformly spaced grid points and remove the points outside of the region.

To understand the process of generating a joint region and grid points, in Fig.

4.4, let us assume that γ_d is greater than the distance between two intersection points, hence they create a joint region. Therefore large possibly included grid points are generated around the mean of the intersection points of measurements which are inside the set. It is shown in Fig. 4.6. Also the potential target regions obtained for each measurement are shown in Fig. 4.5. The straight lines define the bistatic range regions and the dashed lines indicate the DOA regions.

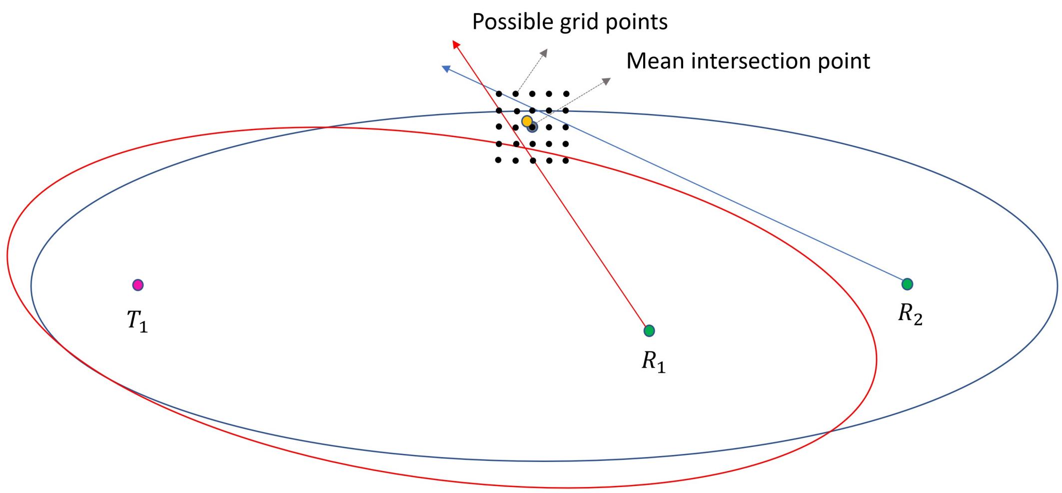

Figure 4.6: Generation of large grid with uniformly separated grid points.

Using the obtained potential target regions and (4.81), the intersection of potential target regions of the group, which is ROI for the case, is the area where any point inside the area is in the region of both receiver which is shown in Fig. 4.7.

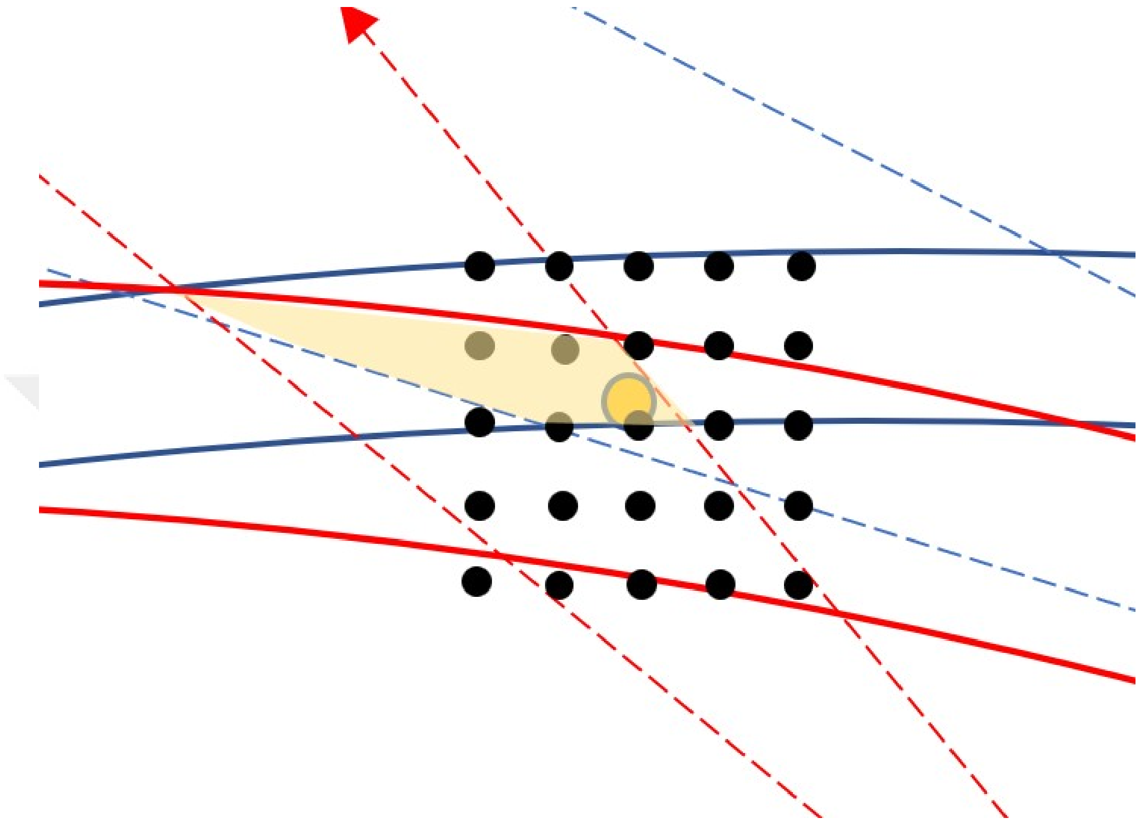

Figure 4.7: Yellow area is the ROI defined by the intersection of both areas A_1 and A_2 using (4.81).

Since the joint region which is the intersection of potential target regions is created. The grid points outside of the region are excluded and target detection is performed on the remaining grid points.

To perform detection, a weight function is defined:

$$w(\boldsymbol{P}) = \sum_{k=1}^{M}\sum_{l=1}^{N}\sum_{i=1}^{N_{meas}(k,l)} \psi_w e^{-\frac{|\rho(\boldsymbol{P};k,l)-\hat{\rho}_{k,l,i}|^2}{2\sigma_{\mathrm{rng}}^2}} + (1-\psi_w)e^{-\frac{|\theta(\boldsymbol{P};k,l)-\hat{\theta}_{k,l,i}||\phi(\boldsymbol{P};k,l)-\hat{\phi}_{k,l,i}|}{2\sigma_{\mathrm{az}}\sigma_{\mathrm{el}}}}, \tag{4.82}$$

where ψ_w is ratio between the effect of bistatic range over DOA on weight function. Note that for $\psi_w = 1$, the weight function equals to (4.67). After weights of grid points are calculated, detection is performed by thresholding.

The case shown in Fig. 4.7 is the ideal case where the closest grid point to the target is in the created region. In addition, the majority of other grid points are at the outside of the region, which prevents false alarms. on the other hand, probability of missed detection increases since the grid points close to the target are extracted if they are not in the ROI. To include more grid point, we can redefine the joint region by editing (4.81):

$$A_C = \bigcup_{i \in C} A_i. \tag{4.83}$$

Here, the joint region is defined as the union of regions, A_i generated by each measurement. In Fig. 4.8, the ROI defined using (4.83) is shown.

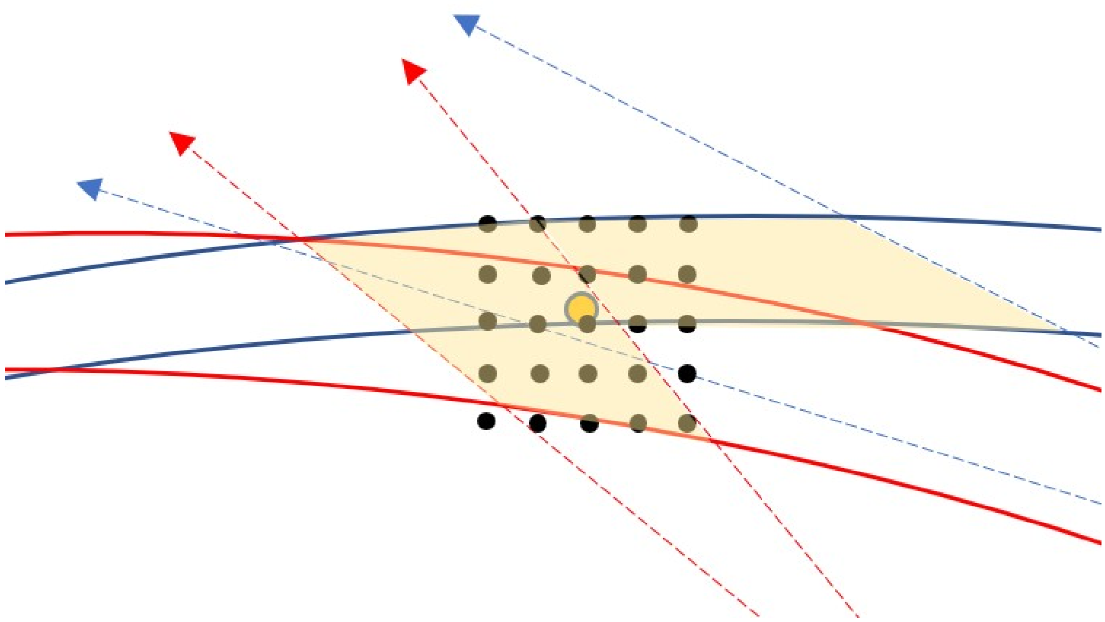

Figure 4.8: Yellow area is the ROI defined by the union of both areas A_1 and A_2 using (4.83).

An important factor to be considered is when the measurements are too noisy. In such cases, it is probable that the areas created by measurements do not intersect, or the intersection does not include the grid points around the target. Such case is shown in Fig. 4.9.

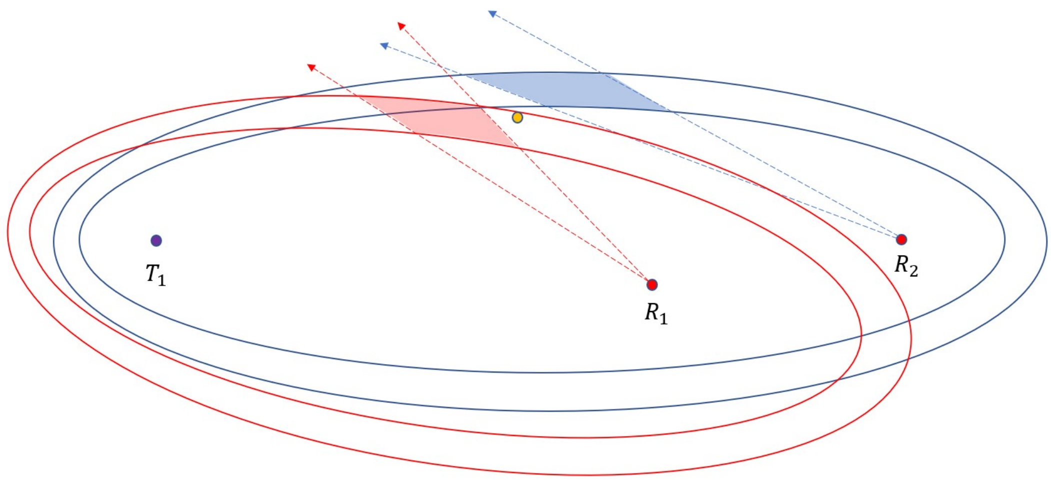

Figure 4.9: The non-overlapping regions case. Colored areas indicate the measurement zone.

Note that it is not possible to include any grid point if the regions do not overlap when (4.81) is used to define the joint region. However, it is still possible to detect the target even if they are not in the joint region. For that purpose, the union of the each measurement region can be defined as the joint region by using (4.83).

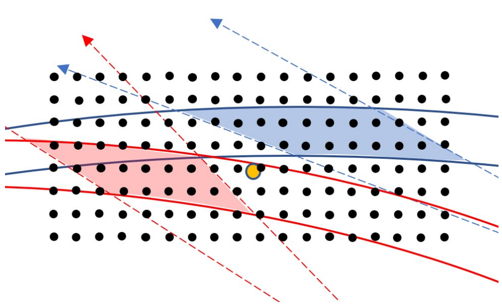

(a) Creation of grid points

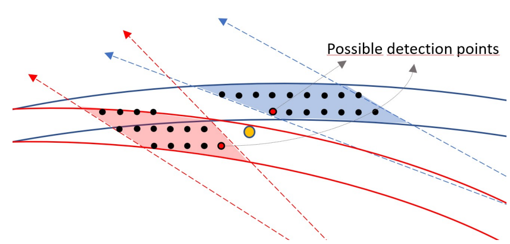

(b) Extraction of grid points outside of the joint region

Figure 4.10: Creating grid inside the joint region defined by the union of regions using (4.83).

In Fig. 4.10b, it is seen that some of the grid points are close to the target. Depending on the weights and the target detection threshold, probability of false alarm or target miss is greater than the performing target detection properly. Because the grid points are at a far distance. To not miss the target, the threshold value should be reduced significantly, which will result in false alarms. On the other hand, if the threshold is not reduced enough, the target will be missed.

In general, most measurement regions cover the target, but few measurement regions do not include the target. For such cases, both intersection and union of sets, which are mathematically defined in (4.81) and (4.83), for joint region definition will provide insufficient system. There are several ways to avoid such case. First solution is to make a new definition of the joint region. Let N_C be the number of measurements in the set C. The intersection of bistatic range and DOA vector of each measurement is calculated and the mean of these intersection points is calculated. Afterwards, a large grid is generated around the mean of the intersection points. We must extract the grid points outside of the joint region. To make a new joint region, we calculate the number of measurement regions that the point is inside of. If a grid point is in enough number of region, the grid point is included to detection phase. Another way is to redefine the regions that was defined in (4.78). To increase the probability of the target present in the region, we can expand the region of each measurement. Since we modeled the DOA measurement error as Gaussian distributed, we can expand the angular range. In (4.78), the angular range is defined as $\pm\sigma_{\mathrm{az}}$ and $\pm\sigma_{\mathrm{el}}$. Since we know that the probability of a gaussian random variable in $\pm 3\sigma$ is 99.73%. Hence, we can expand the angular range from $\pm\sigma$ to $\pm 3\sigma$ for both azimuth and elevation. The resulting region of a measurement is defined as:

$$A_{k,l,i} = \left\{ \boldsymbol{P} \in A_{k,l,i} \middle| \left\{ \begin{array}{c} \hat{\rho}_{k,l,i} - \rho_{\mathrm{res}} < \rho(\boldsymbol{P}; k, l) < \hat{\rho}_{k,l,i} + \rho_{\mathrm{res}}, \\ \hat{\theta}_{l,i} - 3\sigma_{\mathrm{az}} < \theta(\boldsymbol{P}; l) < \hat{\theta}_{l,i} + 3\sigma_{\mathrm{az}}, \\ \hat{\phi}_{l,i} - 3\sigma_{\mathrm{el}} < \phi(\boldsymbol{P}; l) < \hat{\phi}_{l,i} + 3\sigma_{\mathrm{el}} \end{array} \right. \right\} \tag{4.84}$$

In conclusion, the MIMO radar bistatic range and DOA-based Detection system have three main steps. First, we obtain the region for each bistatic pair. Secondly, we generate a grid of possible target positions inside a joint region, which can be (4.81), (4.83), or the way that is described in the paragraph above. Finally, we calculate the weight value of each grid point using (4.82) and perform detection by thresholding as given in (4.68).

4.5 Iterative Position and Velocity Estimation in MIMO Radar Systems

The position of a target can be estimated using bistatic range measurements. At least three bistatic range measurements for two-dimensional space and four bistatic range measurements for three-dimensional space are needed for positioning. The directions of the bistatic Doppler velocities formed by the bistatic pairs must be different from each other for target velocity estimation. In this section, we propose a recursive method for target position and velocity estimation. The proposed method assumes that the measurements for each target are distinguished. Therefore, we have also studied and propose a method for data matching in the case of multiple targets.

4.5.1 Single Target Position and Velocity Estimation

In the case studied here, it is assumed that a single bistatic range and Doppler measurement of the target are made by each transmitter-receiver pair. Some methods for estimating position and velocity using the obtained plots are available in the literature, [41, 42, 83, 39]. In this thesis, we propose a unique policy-iteration-based position and velocity estimation method for MIMO radar systems. This method provides system-level position and velocity estimation by minimizing the following error function:

$$J\left(\boldsymbol{P},\boldsymbol{V}\right)=\sum_{k=1}^{M}\sum_{l=1}^{N}J_1\left(\boldsymbol{P}\right)+\psi_J J_2\left(\boldsymbol{P},\boldsymbol{V}\right), \tag{4.85}$$

where $J_1\left(\boldsymbol{P}\right)$ and $J_2\left(\boldsymbol{P},\boldsymbol{V}\right)$ are the sub-cost values for bistatic range and bistatic Doppler measurements respectively, which are defined as

$$J_1(\boldsymbol{P}) = \sum_{k=1}^{M}\sum_{l=1}^{N}\left(d_{bi}(\boldsymbol{P};k,l) - \hat{d}_{bi}(k,l)\right)^2, \tag{4.86}$$

$$J_2(\boldsymbol{P},\boldsymbol{V}) = \sum_{k=1}^{M}\sum_{l=1}^{N}\left(v_{bi}(\boldsymbol{P},\boldsymbol{V};k,l) - \hat{v}_{bi}(k,l)\right)^2. \tag{4.87}$$

Note that the $J_1(\boldsymbol{P})$ and $J_2(\boldsymbol{P},\boldsymbol{V})$ are defined similar to the (4.72). The weight defined in (4.72) increases for the position and velocity resulting in the bistatic range and Doppler close to the measurements and decreases when the resulting bistatic range and Doppler and measurements differ. In addition, the range of values that the weight value can take is limited inside 0 and MN. On the other hand, the cost function $J(\boldsymbol{P},\boldsymbol{V})$ increases exponentially with the bistatic range and Doppler difference between measured and obtained for the $(\boldsymbol{P},\boldsymbol{V})$ point.

The term ψ_J is determined by the system's importance to velocity estimation. If the ψ_J value is selected high, the system makes the speed estimation more sensitive, and if it is set low, the position estimation is obtained more sensitively. When we studied the results, we observed that position and velocity estimation are performed successfully if the ψ_J value is not selected at the extreme points.

The proposed method works with the policy iteration method. First, the position $\boldsymbol{P}$ is estimated iteratively by minimizing $J_1(\boldsymbol{P})$. Using the resulting $\boldsymbol{P}$ estimation, the velocity $\boldsymbol{V}$ minimizing the $J_2(\boldsymbol{P},\boldsymbol{V})$ function is found iteratively. From here on, the same operations are done for the function $J(\boldsymbol{P},\boldsymbol{V})$ using $\boldsymbol{V}$ obtained in the previous step instead of $J_1(\boldsymbol{P})$. The process is stopped when the change of position and velocity vectors becomes negligible. The pseudo-code of proposed method is given in Algorithm 1.

Algorithm 1 Iterative Position and Velocity Estimation: Cost function $J(\boldsymbol{P}, \boldsymbol{V})$

procedure PosVelEst($(\hat{d}_{bi}(k,l), \hat{v}_{bi}(k,l))$)

  Initialize: $(\boldsymbol{P}_0, \boldsymbol{V}_0)$

  $\widehat{\boldsymbol{P}}_1 \leftarrow \arg\min_{\boldsymbol{P}} J_1(\boldsymbol{P}_0)$

  $\widehat{\boldsymbol{V}}_1 \leftarrow \arg\min_{\boldsymbol{V}} J_2\left(\widehat{\boldsymbol{P}}_1, \boldsymbol{V}_0\right)$

  while $(\widehat{\boldsymbol{P}}, \widehat{\boldsymbol{V}})$ is not converged **do**

    $\widehat{\boldsymbol{P}}_{\mathrm{k}+1} \leftarrow \arg\min_{\boldsymbol{P}} J\left(\boldsymbol{P}, \widehat{\boldsymbol{V}}_{\mathrm{k}}\right)$

    $\widehat{\boldsymbol{V}}_{\mathrm{k}+1} \leftarrow \arg\min_{\boldsymbol{V}} J_2\left(\widehat{\boldsymbol{P}}_{\mathrm{k}+1}, \boldsymbol{V}\right)$

    k $\leftarrow$ k+1

  end while

  return $(\widehat{\boldsymbol{P}}_{\mathrm{k}}, \widehat{\boldsymbol{V}}_{\mathrm{k}})$

end procedure

The main point in this case is the algorithm to be used for calculation of arguments $\boldsymbol{P}$ and $\boldsymbol{V}$ that are minimizing the cost functions. There are some methods for this minimizing process such as gradient descent, Nelder-Mead simplex method [84], etc. The problem is a constrained minimization problem since the position must be inside ROI and the speed of the target cannot be higher than a specified maximum speed. The conventional iterative methods for solving constrained minimization problems are summarized in [85]. However, using constrained minimization solvers is not a must. Hence, we can also use unconstrained minimization solvers for better estimation performance. As a result, we will study position and velocity estimation performance by using Nelder-Mead simplex minimization solver.

4.5.2 Multiple Target Position and Velocity Estimation

When more than one target is in the environment, more than one bistatic range and Doppler measurements are obtained for bistatic pairs. One of the difficulties in multi-target position and velocity estimation is that it is unknown how many targets are in the environment instantly. In addition, The system does not know which of the obtained bistatic range and Doppler measurements belong to which target. For this reason, before estimating the total number of targets in the environment and estimating the position and velocity, it is necessary to match the data additionally. Consideration should be given to the convergence to the local minimum so that precise position and velocity estimation can be made using measurements compared with targets. To overcome this problem, we should roughly estimate the target's position.

When the previously mentioned systems are examined, the target detection system proposed in Section 4.4.1 and 4.4.3 estimates the number of targets in the ROI and the positions of the targets since it performs target detection and position estimation simultaneously. On the other hand, the system described in Section 4.4.2 also performs target detection and estimation of the position and velocity of the targets. However, since the processing load is high, this system is not suitable for practicality. In response to these two systems, the method presented in Section 4.5.1 can quickly and precisely obtain a single target's position and velocity given the bistatic range and Doppler measurements. When these systems are examined, we can see that the detection methods and estimation methods are complementary. Considering these criteria, we propose a novel technique that performs two-stage target detection and position and velocity estimation at the system level.

In the proposed technique, firstly, the coarse grid is opened, and the weights for the cells in the grid are calculated and thresholded in the same way. The proposed technique can work in two ways. The first option is to use only a coarse grid. Target detection is done on the generated coarse grid only. Bistatic measurements corresponding to the detected target detection are matched to the target, and position and velocity are estimated iteratively using the matched measurements. However, when only the coarse grid is used, the targets in the same cell cannot be distinguished. However, when there are two or more bistatic range measurements passing through the same cell, the bistatic measurements passing closest to the cell can be selected. Thus, bistatic range and Doppler measurements belonging to the target with a high probability are selected, and position and velocity estimation is performed consistently. The second option for the proposed technique is to perform two-staged detection. After we generate the coarse grid, we also generate fine grids within the cells where the threshold is crossed, and detection is performed on these fine grids. Thus, multiple targets in the same coarse cell can be distinguished. Then, the system performs data association by matching bistatic range and Doppler measurements for each target, making data ready for the iterative position and velocity estimation.

The aforementioned bistatic measurement matching is done as follows; First, target detection is performed by thresholding the cells in the coarse grid (target detection over the fine grids that are opened after the coarse grids are thresholded). The bistatic ranges of the plots $d_{bi}\left(\boldsymbol{P};k,l\right)$ are calculated for each bistatic pair (k,l). For each bistatic pair, one or more bistatic range measurements $\hat{d}_{bi}\left(k,l\right)$ is made and $\alpha_{k,l} = e^{-\frac{d(\boldsymbol{P};k,l)^2}{2\sigma^2}}$ weights are calculated. This calculation is performed in (4.66),(4.72) or (4.82) for each cell and there is no need to recalculate these values. However, since the computational load of the $\alpha_{k,l}$ calculation is low and the memory usage may be small, there does not appear to be any difficulty in recalculating the $\alpha_{k,l}$ values. The resulting $\alpha_{k,l}$ values are converted into a vector $\alpha_{k,l} = \left[\alpha_{k,l}\left(1\right),\ldots,\alpha_{k,l}\left(N_{det}\right)\right]^T$. Where N_{det} is the total number of detections.

For each bistatic pair (k,l), the measurements $\alpha_{k,l}$ must be associated with one of the plots $\boldsymbol{P}$. This association can be shown in a table:

Meas. / Plots	$E_{1,1}$	$E_{1,2}$	$\ldots$	$E_{M,N}$
$\boldsymbol{P}_1$	$\alpha_{1,1}\left(r_{1,1,1}\right)$	$\alpha_{1,2}\left(r_{1,2,1}\right)$		$\alpha_{M,N}\left(r_{M,N,1}\right)$
$\boldsymbol{P}_2$	$\alpha_{1,1}\left(r_{1,1,2}\right)$	$\alpha_{1,2}\left(r_{1,2,2}\right)$		$\alpha_{M,N}\left(r_{M,N,2}\right)$
$\vdots$				
$\boldsymbol{P}_{N_{det}}$	$\alpha_{1,1}\left(r_{1,1,N_{det}}\right)$	$\alpha_{1,2}\left(r_{1,2,N_{det}}\right)$		$\alpha_{M,N}\left(r_{M,N,N_{det}}\right)$

Table 4.1: Association of bistatic measurements to plots.

In Table 4.1, $E_{k,l}$ is the list of measurements obtained from k^{th} transmitter and l^{th} receiver, $\boldsymbol{P}_t$ is the t^{th} plot obtained from the detection phase, and $r_{k,l,t} \in \{1, 2, \ldots, N_{det}, \emptyset\}$ is the association indices defined by the system. As can be seen in Table 4.1, $r_{k,l,t}$ performs an association between the obtained measurements and the detected plots. Finally, The position and velocity of each plot is estimated by using the associated measurements and with the method presented in Section 4.5.1.

Note that in Table 4.1, it is assumed that there are N_{det} number of measurements obtained by each bistatic pair. However, it is not obligatory that the number of measurements must be equal to N_{det}. A bistatic range measurement can be associated with more than one plot. Additionally, any bistatic range measurement can be associated with a plot by a bistatic pair. In that case, $r_{k,l,t}$ is an empty set. In other words, if we define $r_{k,l,t}$ as a function, this function does not have to be injective nor surjective. Hence, it depends on the method that the system is using for data association.

Data association can be done in several ways. One of them is to make position and velocity estimations using measurements that give the maximum of the weights obtained. For example, let us assume the case where two targets are present in ROI. Furthermore, two separate measurements are considered for the two targets. Here, we can assume that the system obtains two different measurements for both targets of each transceiver pair. Of the two separate contacts obtained for each transceiver pair, those belonging to the detection point of interest now give the higher weight value. Therefore, estimations are made using the measurements with the highest weight value. This technique is quite successful when each bistatic pair's correct measurements for all targets are provided. However, matching the highest weight value providing measurements may not always give the best results. In cases where the system cannot make measurements by each bistatic pair for each target, the position and velocity estimations of the targets with missing measurements will be erroneous. Because when the system cannot perform a measurement that belongs to the interested target, position and velocity estimations are made using the measurements that give the highest weight value among the measurements obtained for other targets. Therefore, the estimation error is remarkably high when the distance between the mismatched measurements and the target of interest is significant.

Another alternative way is to threshold the weights. Thus, in cases where measurements are appropriately provided since the weights obtained from other contacts will probably be low, no data will be used for that bistatic pair, so the estimation errors mentioned above will not occur. However, using thresholds also has unfavorable effects on the system. One of them is the processing load. Suppose more than one weight value exceeds the threshold. In that case, the position and velocity estimation algorithm will run for each data that exceeds the threshold because it is not known which of the predicted positions and velocities is true.

As a result, we found the best way to perform data association. First, we threshold the weights. If any measurement passes the threshold, we do not include any measurement for that bistatic pair. If more than one weight passes, we select the measurement giving the highest weight. If only one weight crosses the threshold, we match the corresponding measurement to the plot.

To summarize, in the case of multiple targets, the position and velocity estimation is calculated for each target point by the method presented in the Section 4.5.1. Data association is performed to make a separate estimation for each target. Associating can be performed in three ways. One is to estimate the position and velocity using the measurements closest to the detection point. The second option is to apply a threshold to the weights obtained from the distance of the measurements to the detection point and make an estimation using measurements that exceed the threshold. The last and the most demanding option is to apply thresholding and choose the closest measurement to the point.

4.6 Generalized Labeled Multi Bernoulli Filter Based Tracking in MIMO Radar Systems

Tracking techniques to be used after detecting moving targets in MIMO Radar systems are generally extended Kalman or particle filters based on the nonlinear measurement models introduced by geometry [86, 87].

The tracking techniques to be used in MIMO Radar systems have two important purposes. These are the determination of the total number of targets in the relevant region and the realization of target tracking by estimating the parameters of these targets. In the literature, there are a number of techniques developed for systems with more than one sensor, similar to MIMO Radar systems. Among these techniques are Joint Probabilistic Data Association [43], Multiple Hypotheses Tracking [44], and Random Finite Set [45, 46] are considered the basic approaches for multi-target tracking. Random Finite Set (RFS) has been used relatively more frequently recently for multi-target tracking. Random Finite Set-based Probability Hypothesis Density (PHD) [88], and Cardinalized PHD (CPHD) [89], developed for multi-target tracking in case of multiple sensors, and the relatively new Multi Bernoulli [45, 46, 90] algorithms have been developed.

The earliest and conceptually simplest multi-sensor PHD, CPHD, and multi-Bernoulli filters are methods that recursively perform parameter correction using the information obtained from each sensor in turn. These methods are also called iterated corrector techniques. This approach produces final solutions based on the processing order of the sensors. Multisensor PHD and CPHD filters that can operate relatively quickly and are independent of the sensor order are proposed in [46]. However, this approach includes a two-stage approach as multisensor PHD, CPHD, and multi-Bernoulli filters are actually approximations of Bayesian multisensor multitarget filter. It should be noted that the multi-target filters discussed so far only predict current states, not trajectories.

A Bayesian multitarget filter that estimates multiple target trajectories is the

Generalized Labeled Multi-Bernoulli (GLMB) filter [91, 92]. The trajectories are obtained by matching the particles obtained in the next step with those in the previous step when the tracking phase of more than one detected target is passed. The biggest obstacle to multisensor GLMB filtering is the very complex (NP-hard) multidimensional particle association problem. The recursive fix strategy will provide the definitive solution if all GLMB components are retained. In practice, however, cutting is performed on each sensor update. Even if the final GLMB filtering density contains only a small number of essential components, the filter will need many particles with each update. A bigger problem is that particles that might be important in GLMB filtering recursion may be discarded after one step and cannot be used afterward. In [93], a multisensor version of the approximate GLMB filter known as the marginalized GLMB filter is proposed. Like the systems mentioned above, this system includes a two-level approach: reducing the GLMB density and filtering this truncated GLMB density.

There are some tracking applications on specifically on MIMO radar systems two of which are given in [47, 48]. These are based on probability hypothesis density and Bernoulli filter. Note that the latter is designed for MIMO radar with colocated antennas. However, these trackers can be enhanced since there are enhanced models are proposed later in the literature. To best of our knowledge, there are any study on MIMO radar tracking using GLMB filter. As a result, we will study the performance of GLMB filter on MIMO radar.

In the rest of this chapter, we will give a summary of GLMB filter by summarizing RFS, multi-Bernoulli RFS, and labelled multi-Bernoulli RFS briefly.

4.6.1 Random Finite Set

An RFS is a set of random variables with a finite number of elements. Each element in this set is represented as a particle which is state vector. When we model the system in discrete time, we define the particle at time k as a vector:

$$\xi = [\boldsymbol{P}, \boldsymbol{V}]^T. \tag{4.88}$$

Let us denote the state vector ξ_i for i^{th} particle. Tracking is performed over the set of these particles, namely RFS $\xi = \{\xi_1, \ldots, \xi_n\}$.

There are two main reasons for its frequent use in multiple tracking systems. First, since the number of targets followed can change over time, adding and removing these targets from the cluster is straightforward. The second reason is that, unlike a matrix system, there is no specific order among the set elements.

4.6.2 Bernoulli RFS

A Bernoulli RFS ξ is an empty set with probability $1 - r$ or a single-element set with a $p(\cdot)$ distribution defined over the space Ξ with probability r. Its probability density function is given as follows:

$$\pi(\xi) = \begin{cases} 1 - r, \xi = \emptyset \\ rp(\xi), \xi = \{\xi\} \end{cases}$$

Ξ is the state space. For example, if there is no limitation over position and velocity, this space equals to $\mathbb{R}^4$ or $\mathbb{R}^6$ for two and three dimensional space respectively.

4.6.3 Multi Bernoulli RFS

A Multiple Bernoulli RFS ξ is a union of independent Bernoulli RFSs $\xi^{(i)}$ and is mathematically expressed as $\xi = \bigcup_{i=1}^{K} \xi^{(i)}$. This RFS is defined by the parameter set $\{\left(r^{(i)}, p^{(i)}\right)\}_{i=1}^{K}$. The probability distribution of this Multiple Bernoulli RFS is

$$\pi(\{\xi_1, \ldots, \xi_n\}) = \prod_{i=1}^{K} (1 - r^{(i)}) \sum_{1 \leq i_1 \neq \ldots \neq i_n \leq J} \prod_{j=1}^{n} \frac{r^{(i_j)} p^{(i_j)}(\xi_j)}{1 - r^{(i_j)}}.$$

In this equation, summation is performed over all permutations $n \leq K$ among K number of particle. We can also obtain the distribution of the total number of targets by subtracting the spatial distributions of the particles $p^{(i_j)}(\xi_j)$ from the equation:

$$\varpi(n) = \prod_{i=1}^{K}(1 - r^{(i)}) \sum_{1 \le i_1 \ne \ldots \ne i_n \le J} \prod_{j=1}^{n} \frac{r^{(i_j)}}{1 - r^{(i_j)}}.$$

4.6.4 Labelled Multi-Bernoulli RFS

The state vectors created here $\xi \in \Xi$ are assigned a "label" $\ell \in \mathbb{L}$ to create trajectories by matching in multi-target tracking in later stages. These labels are allocated from the discrete number space $\mathbb{L} = \{\alpha_i : i \in \mathbb{N}\}$ where the α_i values are different from each other. Labels assigned to different targets consist of a pair of integers $\ell = (k, i)$. Here, k is the moment of emergence of the target, or the moment of birth, as the term PHD is mentioned, and i is the index numbers assigned to separate the targets that appear simultaneously. By using this labeling, that is, the numbering system, the numbers of the targets are different from each other, and there is no need to change it from step to step. The label space resulting at time k is $\mathbb{L}_k = \{k\} \times \mathbb{N}$. The enumerated state vector $\bar{\xi} \in \Xi \times \mathbb{L}_k$ for a target that appeared at time k, and the enumeration space formed by all targets at that moment (those that were created at that moment and survived the filter earlier) $\mathbb{L}_{0:k}$ is regenerated at each step, $\mathbb{L}_{0:k} = \mathbb{L}_{0:k-1} \cup \mathbb{L}_k$. It is shown as $\mathbb{L} \triangleq \mathbb{L}_{0:k}$ to avoid complexity in notation.

A label set of generated numbered RFS $\bar{\xi}$ is shown as $\mathcal{L}\left(\bar{\xi}\right) = \{\mathcal{L}\left(\xi\right) : \xi \in \bar{\xi}\}$ where $\mathcal{L} : \Xi \times \mathbb{L} \to \mathbb{L}$ is the tag pointer. Remember, a unique label must be assigned to each target $\left|\mathcal{L}\left(\bar{\xi}\right)\right| = \left|\bar{\xi}\right|$. Here $|\bullet|$ returns the total number of targets (cardinality). To control this, a distinct label indicator is defined,

$$\hbar\left(\bar{\xi}\right) = \delta_{|\bar{\xi}|}\left(\left|\mathcal{L}(\bar{\xi})\right|\right)$$

where δ is the Kroneker delta function:

$$\delta_y(x) = \begin{cases} 1, \text{if } x = y \\ 0, \text{otherwise} \end{cases}.$$

Similar to the multi-Bernoulli RFSs, LMB RFSs can be defined by a parameter set $\left\{\left(r^{(\dagger)}, p^{(\dagger)}\right) : \dagger \in \mathbb{D}\right\}$ where$\mathbb{D}$ is the index space. If a single Bernoulli component returns a non-empty set, it is assigned the number $\alpha(\dagger)$ as mentioned above. Distribution of obtained LMB RFS

$$\pi\left(\left\{\left(\xi_1, \ell_1\right), \ldots, \left(\xi_n, \ell_n\right)\right\}\right) = \prod_{\dagger \in \mathbb{D}} \left(1 - r^{(\dagger)}\right) \prod_{j=1}^{n} \frac{1_{\alpha(\mathbb{D})}\left(\ell_j\right) r^{\left(\alpha^{-1}(\ell_j)\right)} p^{\left(\alpha^{-1}(\ell_j)\right)}\left(\xi_j\right)}{1 - r^{\left(\alpha^{-1}(\ell_j)\right)}} .$$

Even if α can be any function suitable for the desired conditions, identity mapping that gives the same output as the α input is used for convenience. In other words, the displayed indexes of the targets will also be equal to the numbers assigned to them.

4.6.5 Generalized Labeled Multi-Bernoulli RFS

The distribution of the generalized labeled multi-Bernoulli (GLMB) RFS is

$$\pi\left(\bar{\xi}\right) = \hbar(\bar{\xi}) \sum_{(I,h) \in \mathcal{F}(\mathbb{L}) \times \mathbb{H}} w^{(I,h)} \delta_I\left(\mathcal{L}\left(\bar{\xi}\right)\right) p^{(h)}(\bar{\xi}). \tag{4.89}$$

where $\mathbb{H}$ is the space of trajectories created by matching the points in the past. I is the trajectory index which is a new trajectory assignment that is defined in the trajectory set $\mathcal{F}(\mathbb{L})$ in current time. Additionally, $w^{(I,h)}$ is a weight function that is defined to satisfy the following conditions,

$$\sum_{L \subseteq \mathbb{L}} \sum_{(I,h) \in \mathcal{F}(\mathbb{L}) \times \mathbb{H}} w^{(I,h)} \delta_I\left(\mathcal{L}\left(\bar{\xi}\right)\right) = 1 \tag{4.90}$$

$$\int p^{(h)}\left(\xi, \ell\right) d\xi \ = 1 \tag{4.91}$$

The trajectory space $\mathbb{H}$ is created by the history of associations $\mathbf{h}_i = (h_i(j_i), h_i(j_i+1) \ldots, h_i(k_i))$ where j_i is the time of birth of the i^{th} target and k_i is the time of death of the i^{th} target and $h_i(t)$ is associated measurement to i^{th} target at time t. Besides, the current track label space $\mathcal{F}(\mathbb{L})$ is created by the new state associations I. Note that if k_i equals to the current time step and a new association I is made for i^{th} target, the target is continued to be tracked and the time of death is increased until any new association is made.

A pair $(I, h) \in \mathcal{F}(\mathbb{L}_{0:k}) \times \mathbb{H}$ is called an hypothesis. In other words, (4.89) gives us the probability distribution at time k for $\bar{\xi}$ given the measurements at time k, which can be denoted by $\pi_{k|k}(\bar{\xi}, \hat{\xi}_k)$. Using the definitions, we can write the initial probability as

$$\pi_0(\bar{\xi}) = \hbar(\bar{\xi}) \sum_{I \in \mathcal{F}(\mathbb{L})} w_0^{(I)} \delta_I \left(\mathcal{L}\left(\bar{\xi}\right)\right) p_0^{(h)}(\bar{\xi}).$$

Since this is the initial step, the labels $I \in \mathcal{F}(\mathbb{L})$ represents a set of track labels. For convenience, let us define a label $\ell \in I$ by two integers $\ell = (k, l)$ where k is the time step that the target is born and l is the target index that is assigned at the time of born.

The GLMB distribution includes all possible hypotheses. For example, let us consider the case that there are two measurements $\hat{\xi}_1, \hat{\xi}_2$ obtained in the initial step. Noting that the weights must satisfy the conditions given in (4.90) and (4.91), we can consider weights as the probability of the given hypothesis. With probability $w_0^{\{\emptyset\}}$, any target is born at the initial step. With probability $w_0^{\{(0,1)\}}$, only the first target is born. With probability $w_0^{\{(0,2)\}}$, only the second target is born. Lastly, with probability $w_0^{\{(0,1),(0,2)\}}$, both targets are born. Additionally, defining the state probability densities as $p_0^{(0,1)}(\bar{\xi}) = \mathcal{N}(\mu_1, \sigma_1)$ and $p_0^{(0,2)}(\bar{\xi}) = \mathcal{N}(\mu_2, \sigma_2)$, the GLMB distribution becomes:

$$\begin{aligned}
\pi_0(\bar{\xi}) = {} & w_0^{\{\emptyset\}} \delta_{\{\emptyset\}} \left(\mathcal{L}\left(\bar{\xi}\right)\right) \\
& + w_0^{\{(0,1)\}} \delta_{\{(0,1)\}} \left(\mathcal{L}\left(\bar{\xi}\right)\right) p_0^{(0,1)}(\bar{\xi}) \\
& + w_0^{\{(0,2)\}} \delta_{\{(0,2)\}} \left(\mathcal{L}\left(\bar{\xi}\right)\right) p_0^{(0,2)}(\bar{\xi}) \\
& + w_0^{\{(0,1),(0,2)\}} \delta_{\{(0,1),(0,2)\}} \left(\mathcal{L}\left(\bar{\xi}\right)\right) p_0^{(0,1)}(\bar{\xi}) p_0^{(0,2)}(\bar{\xi})
\end{aligned}$$

Note that we did not include the h since it is the initial step. For other cases, we have to include the trajectory history.

The parameters in the calculations shown so far have to be calculated separately. Since the actual locations of the targets are unknown, target tracking is carried out in three stages: Instant target estimations, predictions in the following step, and estimating target positions. In short, the GLMB filters start or stop tracking and assign a point to trajectories by labeling the points to any trajectory. Hence, the GLMB filter can track multiple times even if the number of targets changes during the tracking times.

4.7 Conclusions

In this chapter, we have proposed some novel techniques to be used in MIMO radar systems. The first one is the range and Doppler estimation in the presence of multiple targets using PPLFM waveforms. The system is based on point association and limiting the range and Doppler span. The points exceeding the limits are eliminated. The measurements are then sent to the proposed detection system.

The second proposed method is a low complexity MIMO radar detection scheme. The proposed method can depend on three measurement types, bistatic range, bistatic Doppler, and DOA. We have studied three cases; detection using bistatic range-only, bistatic range and Doppler, and bistatic range and DOA. We have designed the system by generating a grid of possible target points, calculating a weight value, and performing detection by thresholding. Note that the detection points are also a coarse estimation of target positions. These detection points are directed to the third proposed system.

The third proposed method is to estimate the position and velocity of a target using the bistatic range and Doppler measurements. We have offered a cost function and iteratively estimated the position and velocity of the target by minimizing this cost function. The system is designed as a policy iteration. As indicated previously, this method is applied to the detection points. First, data association is made for each detection point. After that, estimation is performed using the associated measurements. The estimated position and velocities are then directed to the tracker.

The last proposed method is the implementation of a GLMB filter on MIMO radar systems for target tracking. As indicated in the previous paragraph, the system uses the target estimations obtained by performing estimation on detection points. These estimations are used as measurements by the GLMB filter. The GLMB filter then tracks the targets.

As a result, we have studied and developed novel techniques for MIMO radar applications. Note that these proposed methods can create a complete MIMO radar system.

Chapter 5

Performance of Proposed MIMO Signal Processing Techniques

5.1 Introduction

In this chapter, we will show simulation results of the mentioned and proposed techniques in chapter 4. In Section 5.2, we will study the performance of the PLFM and PPLFM waveforms and analyze the effects of the system parameters. First, the auto and cross ambiguities of the PLFM waveforms are studied. Afterward, the performance of the PPLFM waveform by studying the auto and cross ambiguity functions and examining the effects of specific parameters.

In Section 5.3, we will show the simulation results of the MIMO radar bistatic range only detection algorithm. The algorithm will be tested on a specific scenario. we will study the effects of γ_w and the geometry.

In Section 5.4, we will perform position and velocity estimation and analyze the results. We will examine the performance by estimating the position and velocity of detection points obtained in the detection phase. Therefore, We will also discuss the system performance of the measurement association technique.

In Section 5.5, we will study the performance of the EMVS-MIMO radar system. Many factors are affecting the total performance of the system. Hence, we will examine the effects of the parameters ψ_w, γ_d, and the effects of geometry.

Lastly, we will study the GLMB filter performance on the MIMO radar tracking problem in Section 5.6. We will use the detection points as measurements and perform tracking on these points. We will use a different set of detections to test. Therefore, we will see the effects of the detection algorithm outputs on tracking performance. On the other hand, we will study the impact of other factors, such as the probability of birth, on system performance.

5.2 PLFM and PPLFM Waveforms and Multiple Target Range and Doppler Estimation

To analyze PLFM and PPLFM waveforms' performance, the ambiguity function (AF) is used:

$$A_{y,s}(\tau, f_d) = \int_0^T y(t)s^*(t-\tau)e^{j2\pi f_d t}dt. \tag{5.1}$$

Note that the ambiguity function can be used for the same signal and the correlation between two signals. For the case when $y(t) = s(t)$, the ambiguity function is called auto ambiguity function, and when $y(t) \neq s(t)$, the ambiguity function is called cross ambiguity function, [94].

First, PLFM waveform is examined. The auto and cross ambiguity function output of PLFM waveform is given in Fig. 5.1 and 5.2.

As we can see, the PLFM waveform has considerably prominent peaks in cross AF. Hence, the PLFM waveform may not be suitable for MIMO radar systems. To this end, the PPLFM waveform is studied to see if this waveform is suitable for MIMO radar applications.

PPLFM waveforms are polyphased modulated version of PLFM waveforms. From the point that it has rectangular wave for each chip, the properties of the

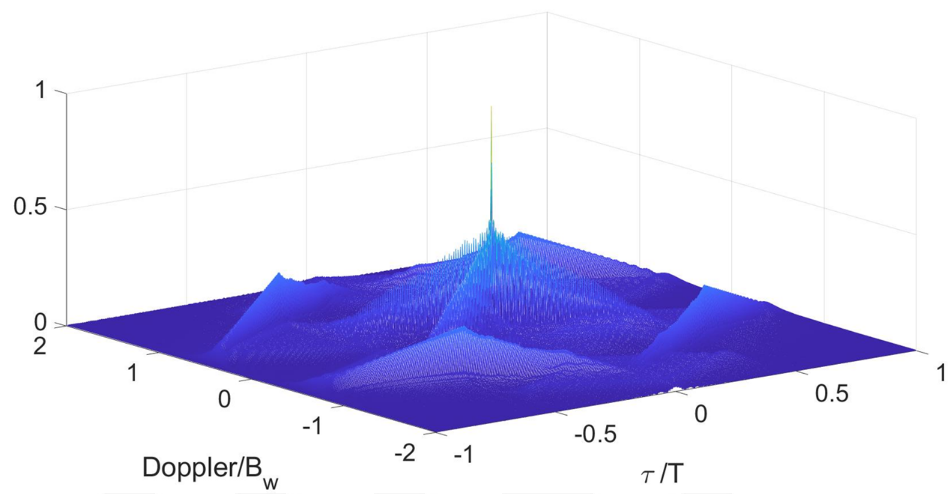

Figure 5.1: Auto ambiguity function of PLFM waveform for $f_a = 0.5B_w$

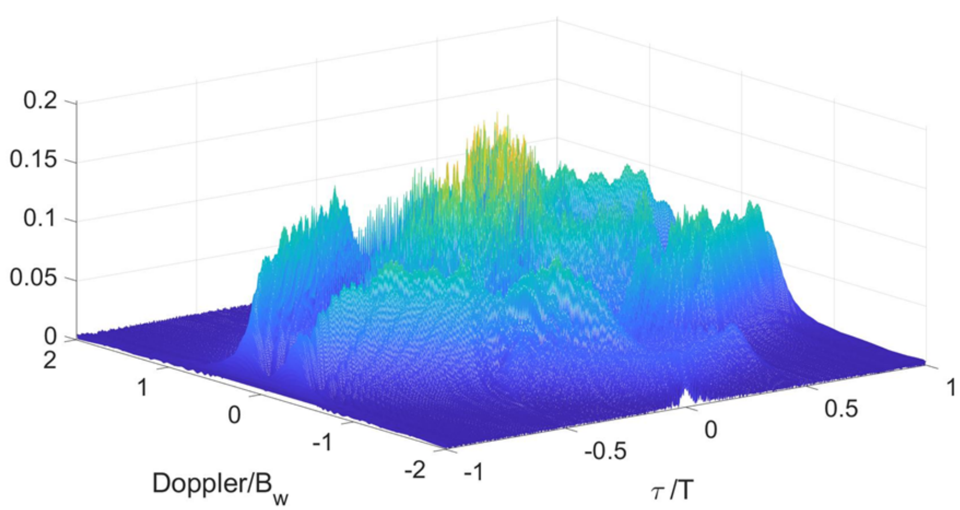

Figure 5.2: Cross ambiguity function of PLFM waveform for $f_a = 0.25B_w$ and $f_a = 0.75B_w$

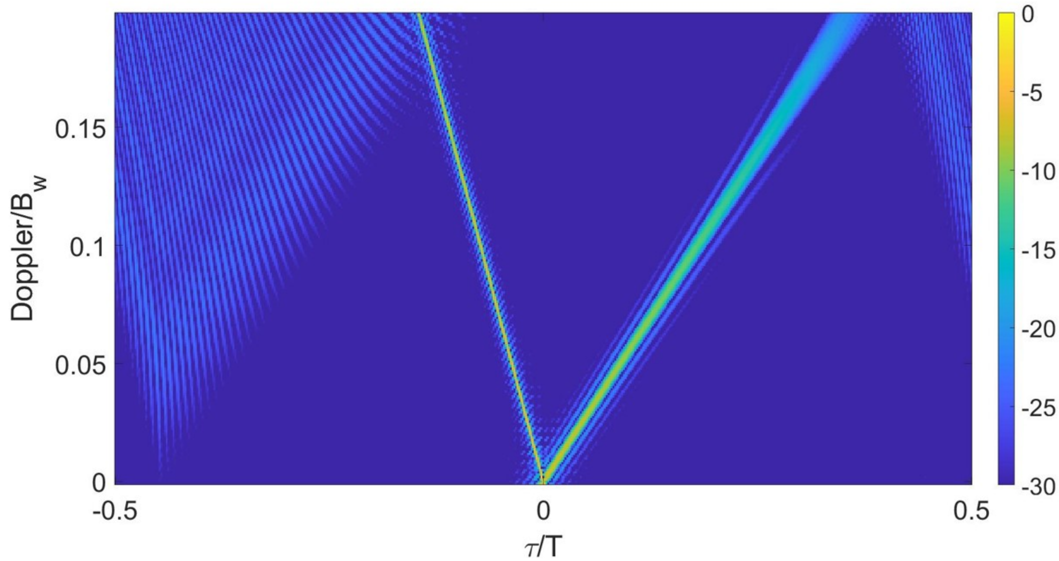

Figure 5.3: Auto AF of PPLFM waveform for $i = 1$ and $N = 500$. The result given in dB

waveform changes according to the chip duration, hence number of chips since the period of the signal is constant.

Doppler tolerance of the PPLFM waveform is expected to be sufficiently high. To evaluate its Doppler tolerance and performance, the auto AF is applied for two cases, one for $N = 500$, one for $N = 3000$. We consider the waveforms with $f_a = 0.25B_w$, $f_a = 0.5B_w$ and $f_a = 0.75B_w$, and refer them as $i = 1$, $i = 2$ and $i = 3$ respectively. The auto AF of PPLFM with $f_a = 0.25B_w$, $f_a = 0.5B_w$ and $f_a = 0.75B_w$ for both case is given in Fig. 5.3, 5.4, 5.5, 5.6, 5.7, 5.8.

Comparing Fig. 5.3, 5.4 and 5.5 with Fig. 5.6, 5.7 and 5.8, it is obvious that the Doppler tolerance is better for greater number of chips used. The output on main lobes are higher and the width is smaller, which makes it easier to detect the main lobes and increases range resolution. In addition to this, it is observed that the level of the main lobe decreases as it progresses in the Doppler plane, the Doppler tolerance decreases. As mentioned earlier, extended matched filters increase Doppler tolerance on the receiver side.

On the other hand, the correlation between any two signal is required to be

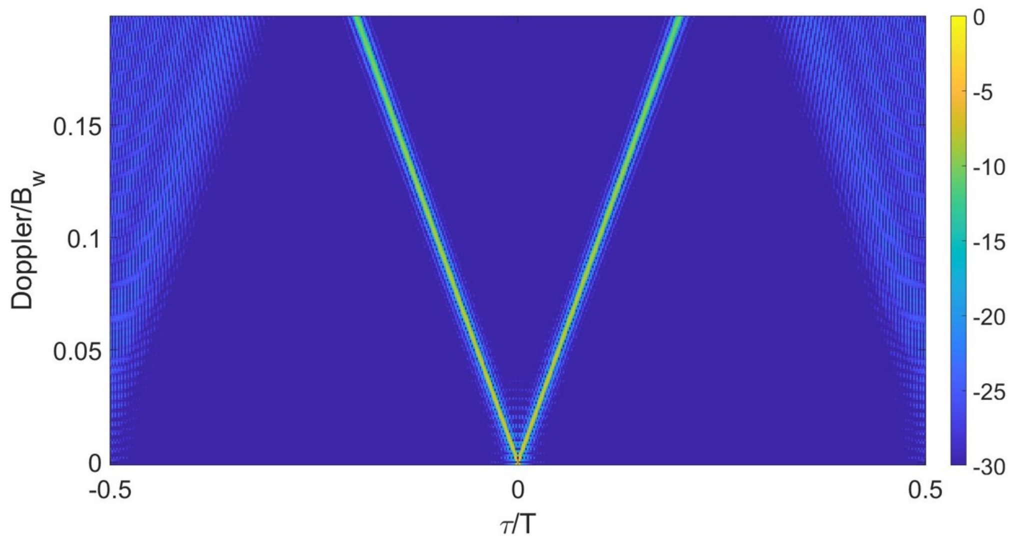

Figure 5.4: Auto AF of PPLFM waveform for $i = 2$ and $N = 500$. The result given in dB

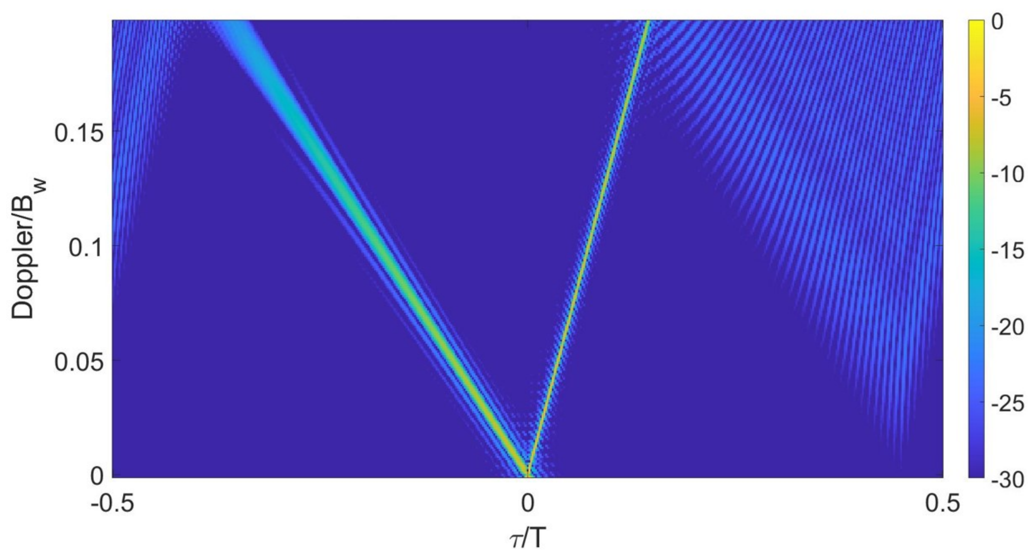

Figure 5.5: Auto AF of PPLFM waveform for $i = 3$ and $N = 500$. The result given in dB

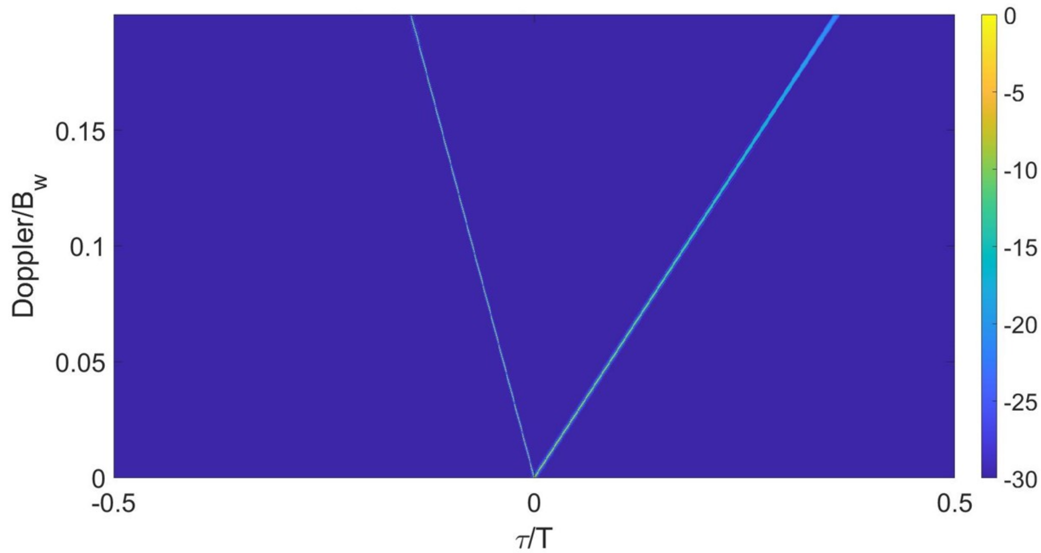

Figure 5.6: Auto AF of PPLFM waveform for $i = 1$ and $N = 3000$. The result given in dB

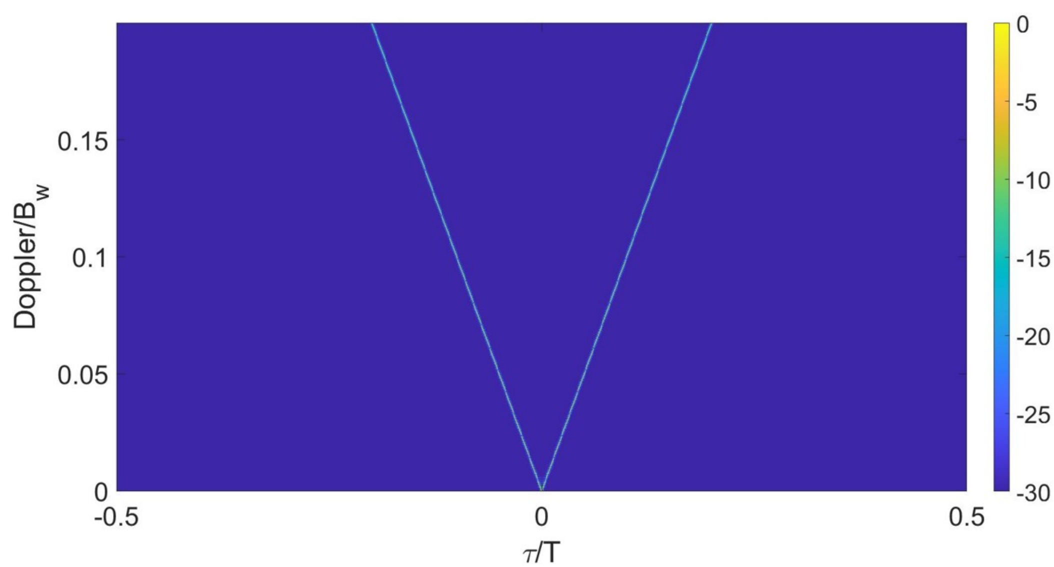

Figure 5.7: Auto AF of PPLFM waveform for $i = 2$ and $N = 3000$. The result given in dB

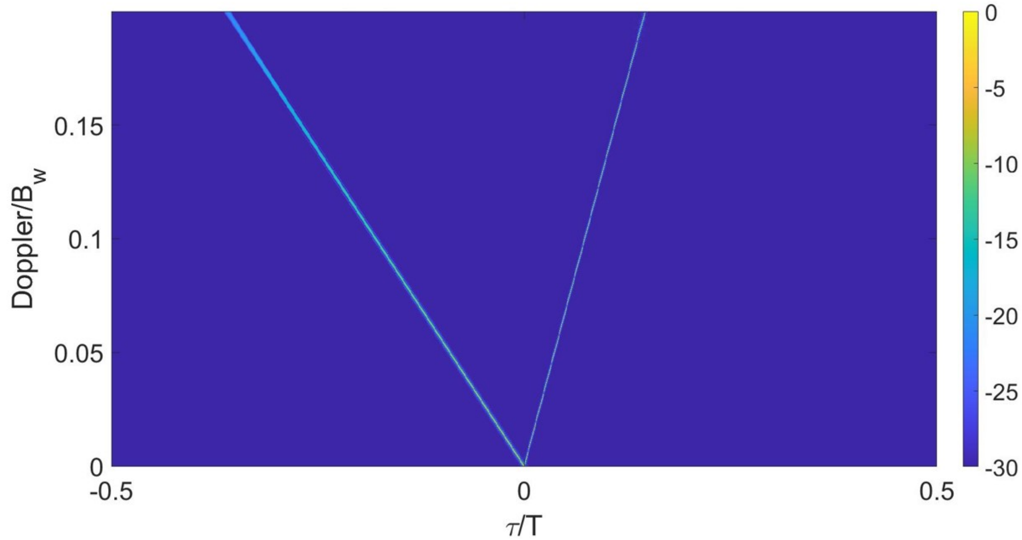

Figure 5.8: Auto AF of PPLFM waveform for $i = 3$ and $N = 3000$. The result given in dB

low at any delay and Doppler. For that purpose, cross AFs for $N = 500$ and $N = 3000$ are calculated.

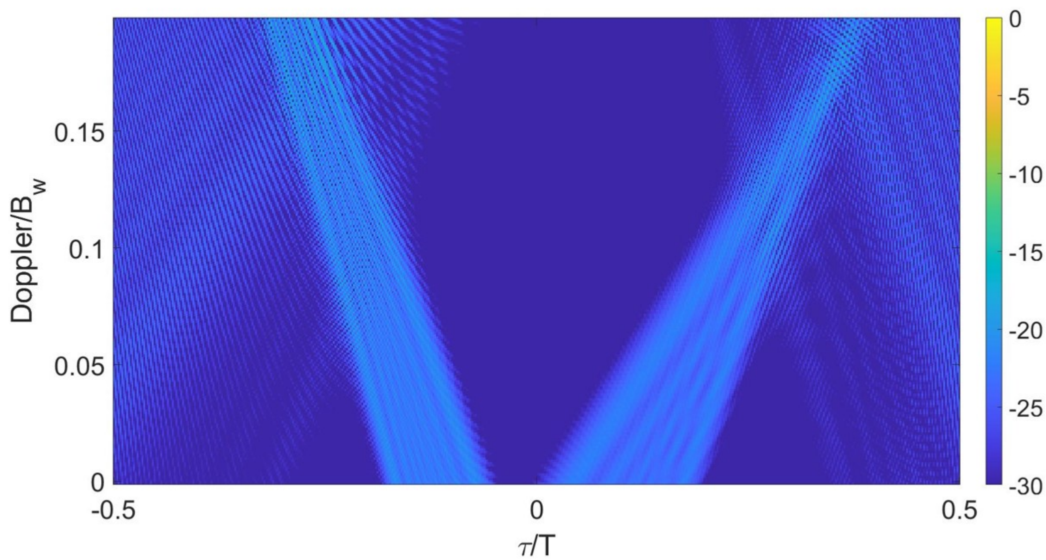

Figure 5.9: Cross AF of PPLFM waveforms $i = 1$ and $i = 2$ for $N = 500$. The result given in dB

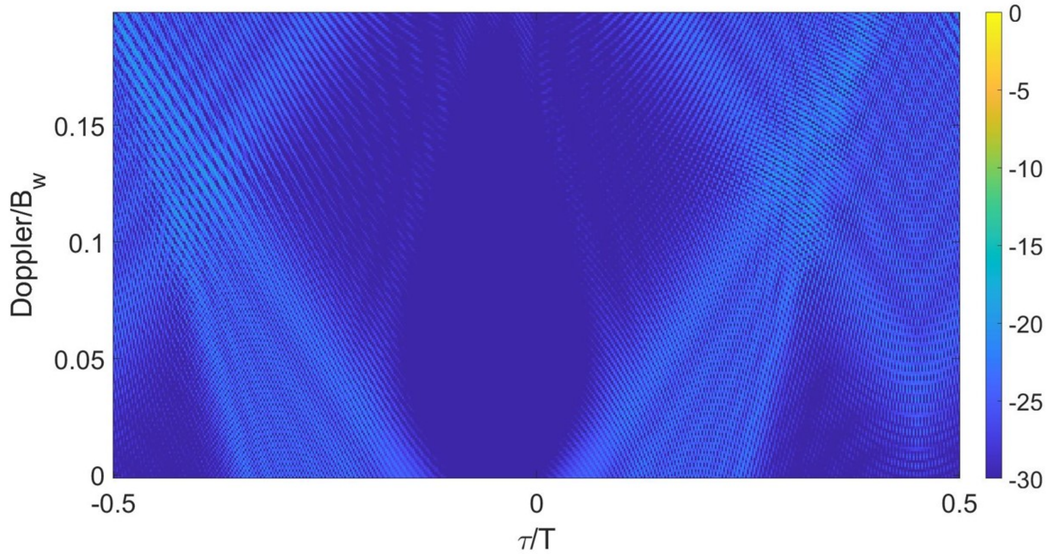

Figure 5.10: Cross AF of PPLFM waveforms $i = 1$ and $i = 3$ for $N = 500$. The result given in dB

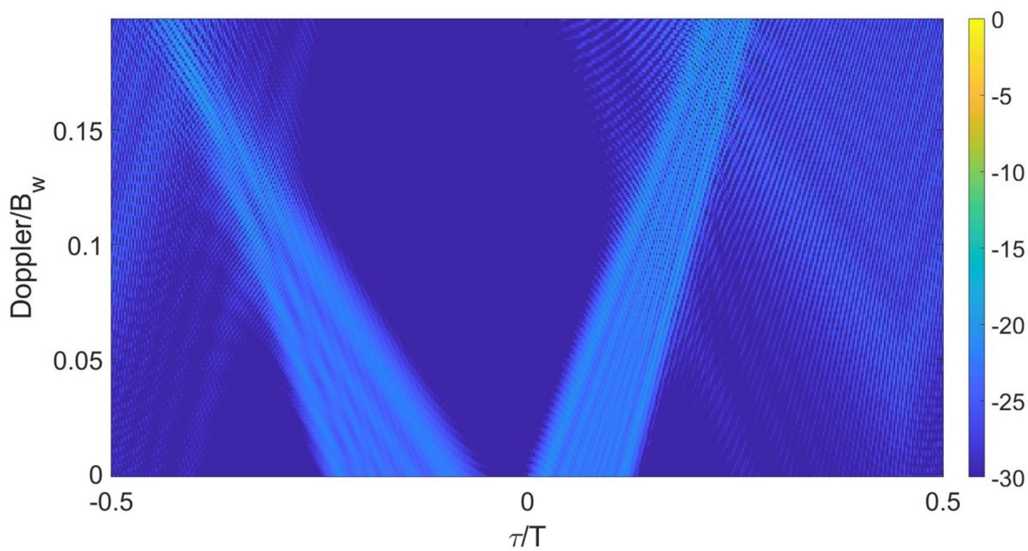

Figure 5.11: Cross AF of PPLFM waveforms $i = 2$ and $i = 3$ for $N = 500$. The result given in dB

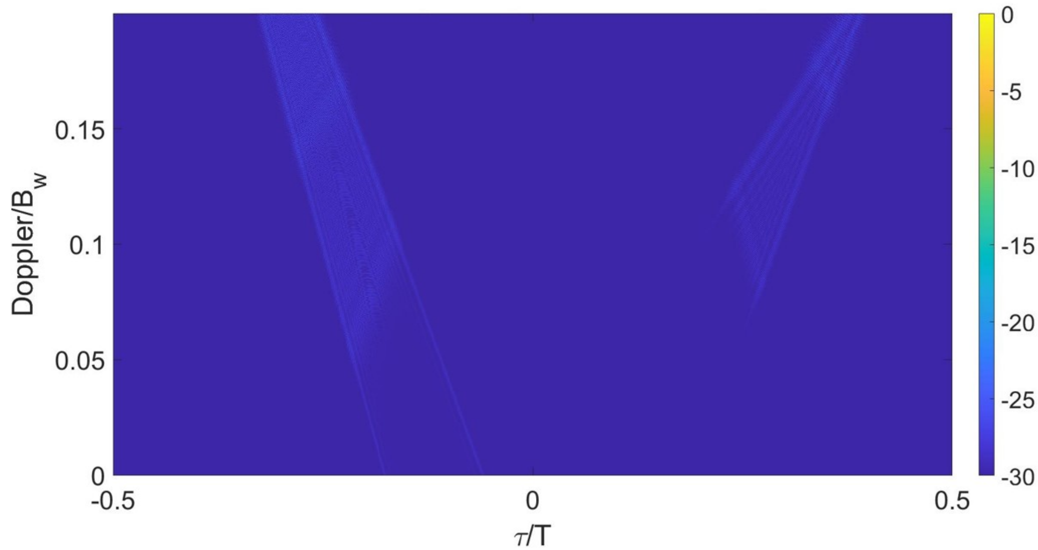

Figure 5.12: Cross AF of PPLFM waveforms $i = 1$ and $i = 2$ for $N = 3000$. The result given in dB

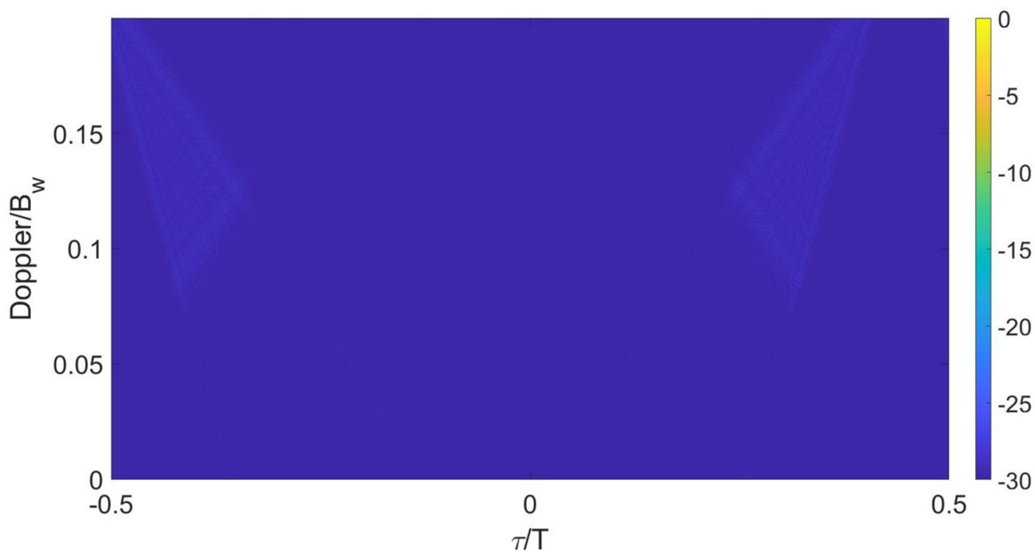

Figure 5.13: Cross AF of PPLFM waveforms $i = 1$ and $i = 3$ for $N = 3000$. The result given in dB

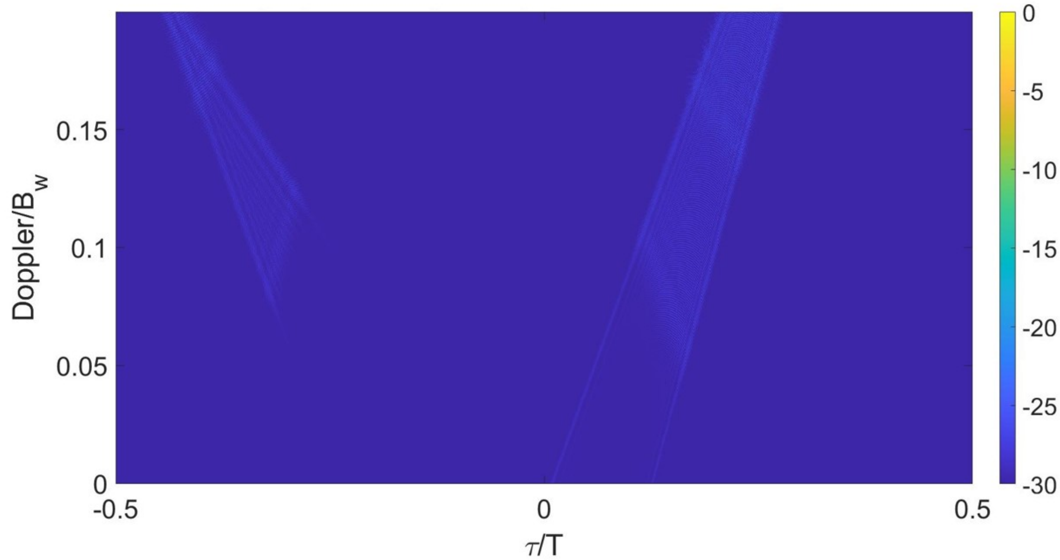

Figure 5.14: Cross AF of PPLFM waveforms $i = 2$ and $i = 3$ for $N = 3000$. The result given in dB

In addition, as can be seen from figures 5.9 to 5.14, increasing the N value decreases the correlation between different waveforms at each delay and Doppler value. As a result of this observation, we can say that N should be appropriately selected to decrease the interference between the signals from different transmitters at receiver.

Since we observe the effects of the number of chips on system performance, from this point, we will study the filter outputs, and delay and Doppler estimation from these filter outputs. Let us consider the case where PPLFM signals for all transmitters $i = 1, 2, 3$, the signal is received with $\tau = 0.1T$ and $f_d = 0.2B_w$ by a single receiver. The transmitters are assumed to generate signals continuously, which results in $PRI = T$. To see the benefits of extended matched filter, we generate and apply matched filter and extended matched filter and compare the outputs. After the generation of matched filters and extended matched filters with $p_{\text{xmf}} = 0.1$ for each signal, the received signal is filtered by all three filter for both filter type. The receiver is assumed to have same energy for each transmitter. The outputs are given in Fig. 5.15-5.20.

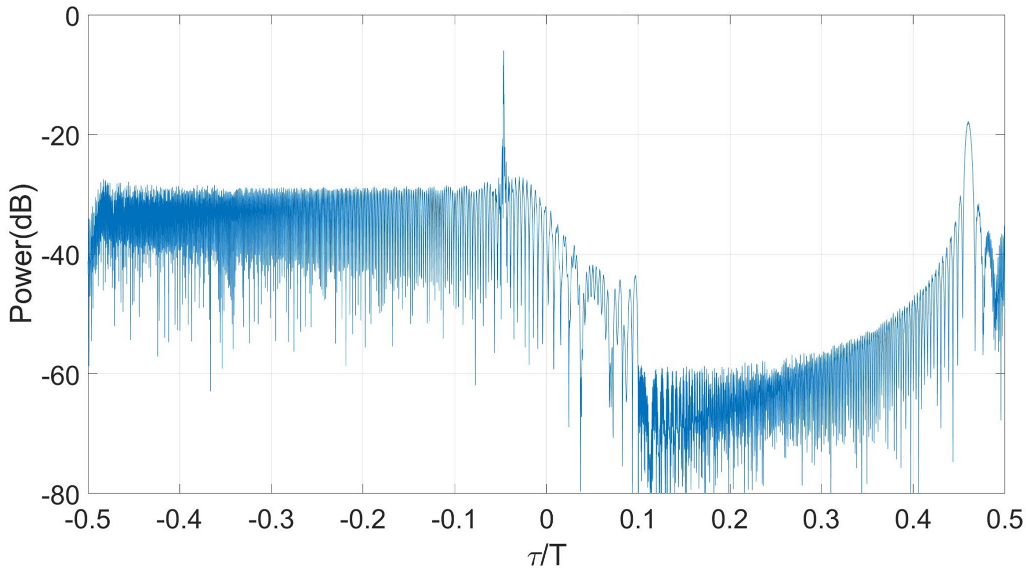

Figure 5.15: $i = 1$ matched filter output for received signal with $\tau = 0.1T$ and $f_d = 0.2B_w$

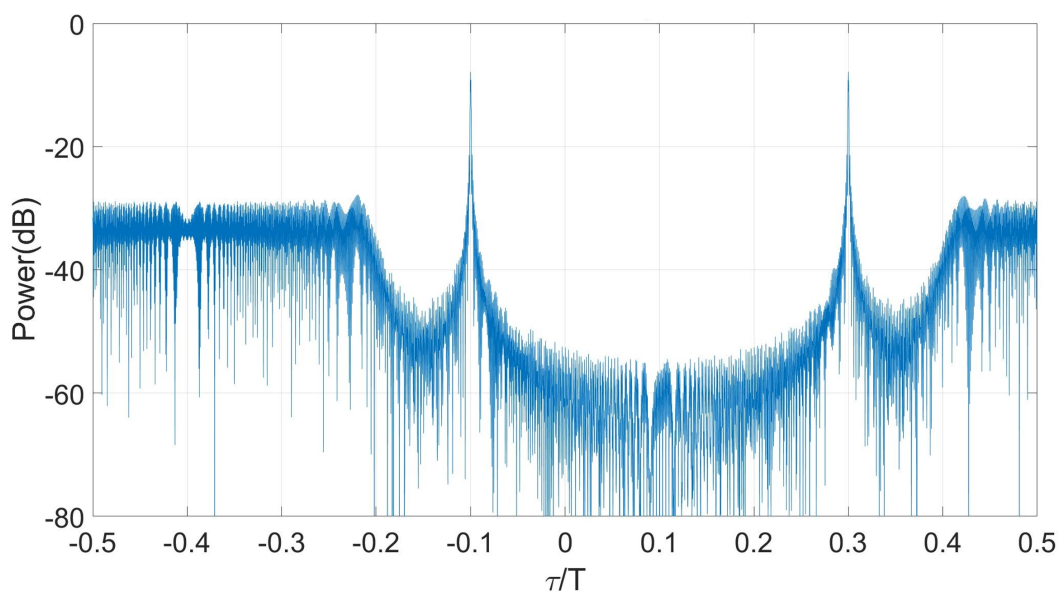

Figure 5.16: $i = 2$ matched filter output for received signal with $\tau = 0.1T$ and $f_d = 0.2B_w$

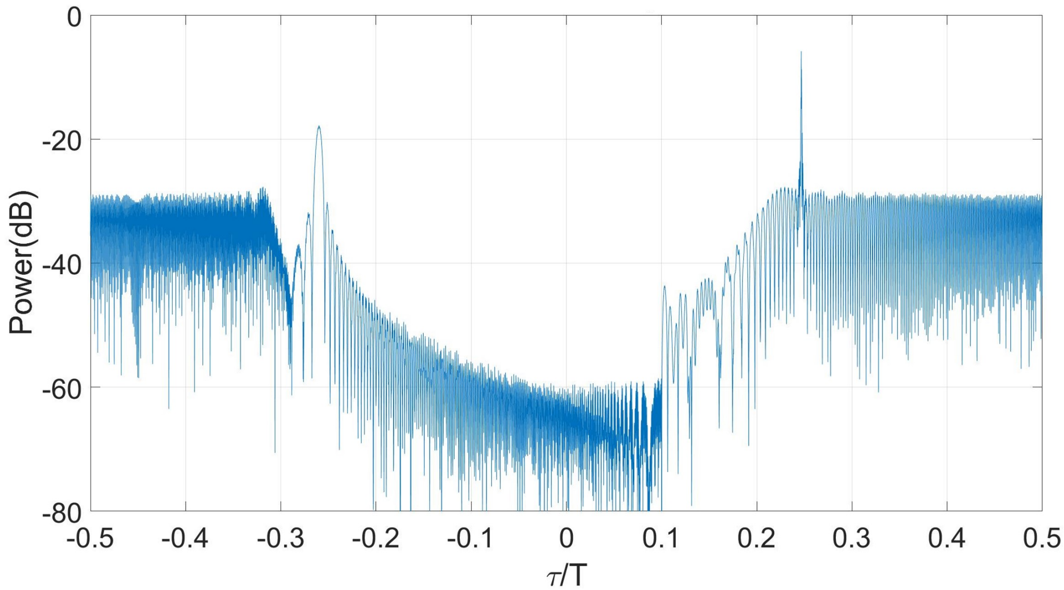

Figure 5.17: $i = 3$ matched filter output for received signal with $\tau = 0.1T$ and $f_d = 0.2B_w$

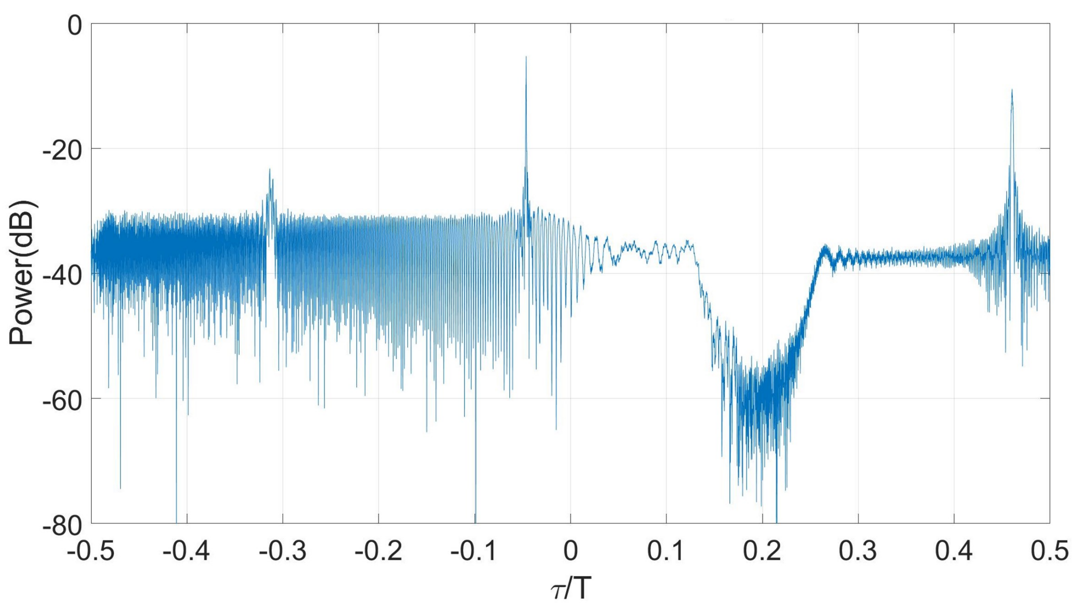

Figure 5.18: $i = 1$ extended matched filter output for received signal with $\tau = 0.1T$ and $f_d = 0.2B_w$

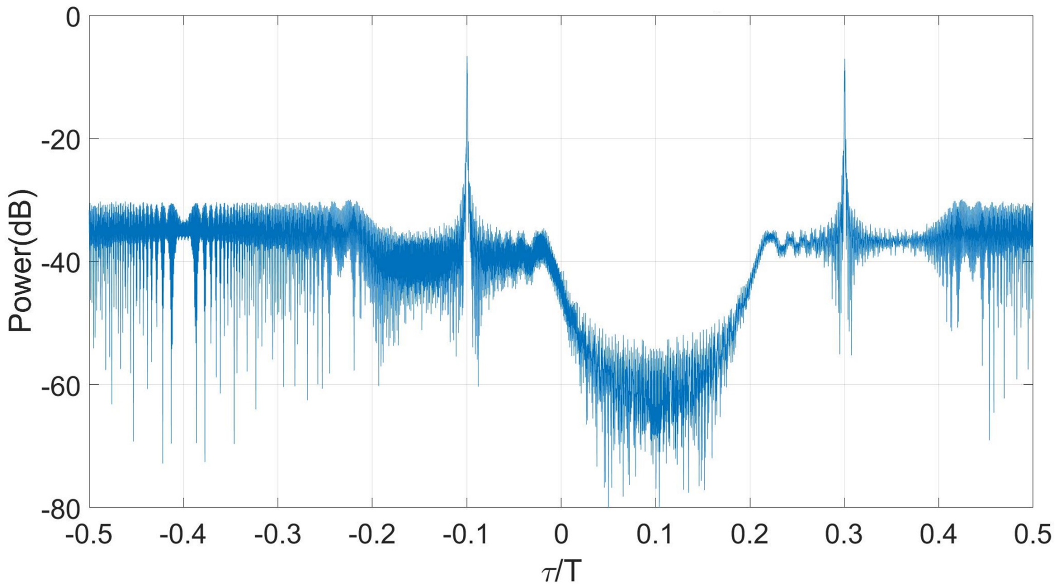

Figure 5.19: $i = 2$ extended matched filter output for received signal with $\tau = 0.1T$ and $f_d = 0.2B_w$

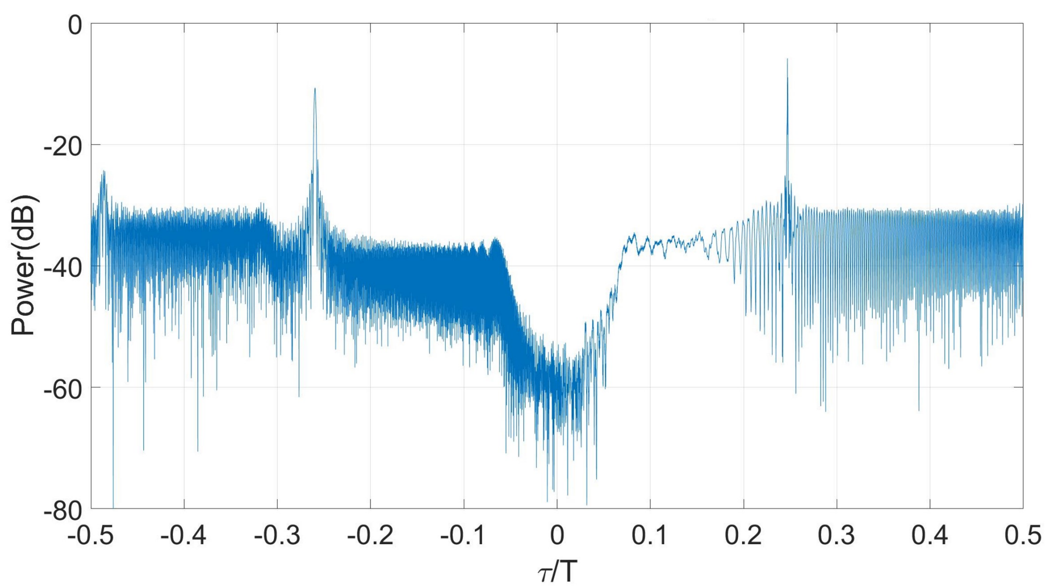

Figure 5.20: $i = 3$ extended matched filter output for received signal with $\tau = 0.1T$ and $f_d = 0.2B_w$

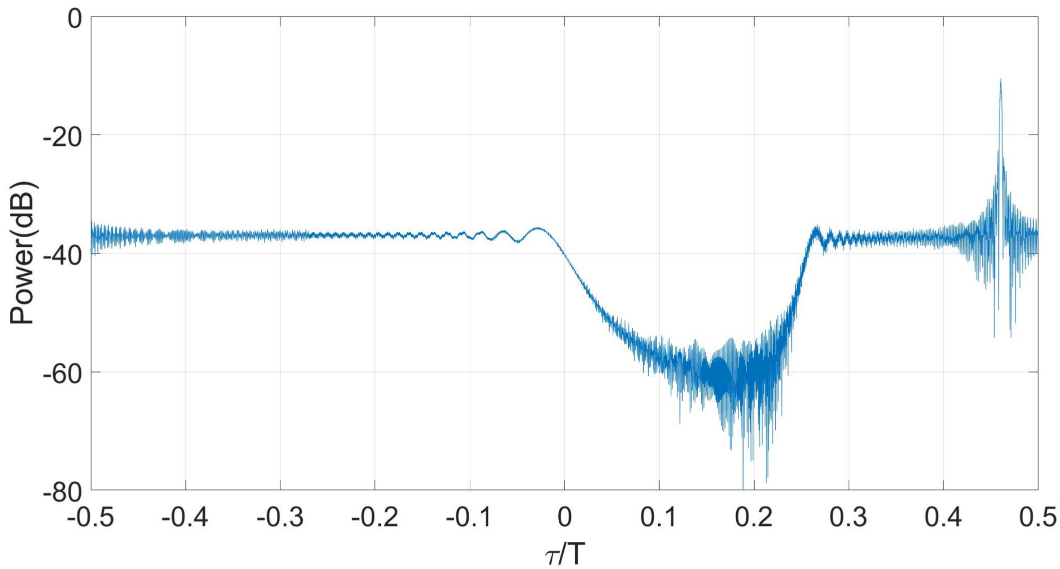

Figure 5.21: XMF $f^a_{1,\mathrm{xmf}}(t)$ output for received signal with $\tau = 0.1T$ and $f_d = 0.2B_w$

The filter outputs shown in Fig. 5.15-5.20 demonstrate that XMF provides approximately 7dB Doppler gain, especially in i=1 and i=3 codes. However, the use of XMF creates an increase in the side lobes. But, as a result of this increase, the side lobes can only reach -30 dB levels, so it does not pose a challenge to the system. Additionally, the width of the main lobes are smaller when XMF is used, which enhances range resolution. As a result, the usage of XMF is appropriate. Hence, we will only consider XMF from that point.

To estimate delay and Doppler, one must find T^a_i and T^b_i from the filter output by finding the two peaks. However, since there are two peaks XMF output, the peaks should be paired with T^a_i and T^b_i. In order to pair the values, the two parts of the filter output should be examined separately from each other as given in (3.15). In other words, XMF is applied seperately by $f^a_{i,xmf}(t)$ and $f^b_{i,xmf}(t)$. Here, $f^a_{i,xmf}(t)$ and $f^b_{i,xmf}(t)$ correspond to ascending and descending LFM parts respectively.

After the obtained filter outputs are thresholded, the target delay and Doppler are estimated by (3.19) and (3.16) respectively. In Table 5.1, the resulting estimations are given.

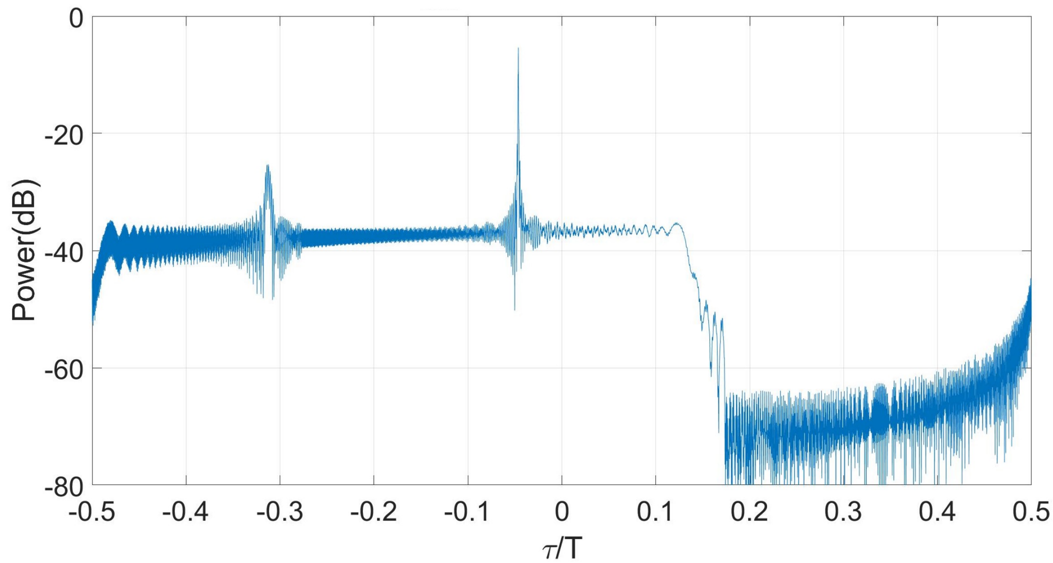

Figure 5.22: XMF $f^b_{1,\mathrm{xmf}}(t)$ output for received signal with $\tau = 0.1T$ and $f_d = 0.2B_w$

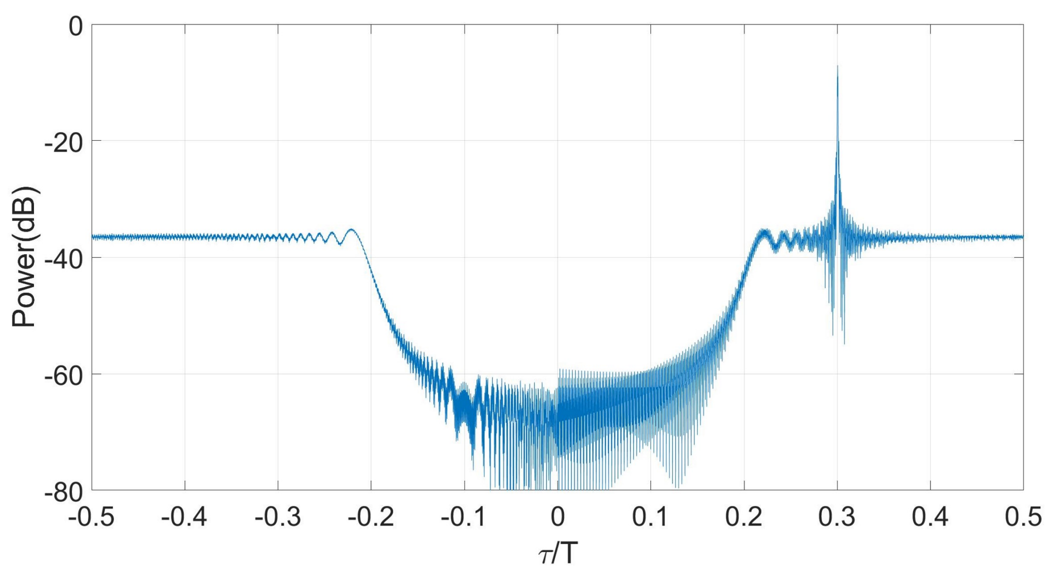

Figure 5.23: XMF $f^a_{2,\mathrm{xmf}}(t)$ output for received signal with $\tau = 0.1T$ and $f_d = 0.2B_w$

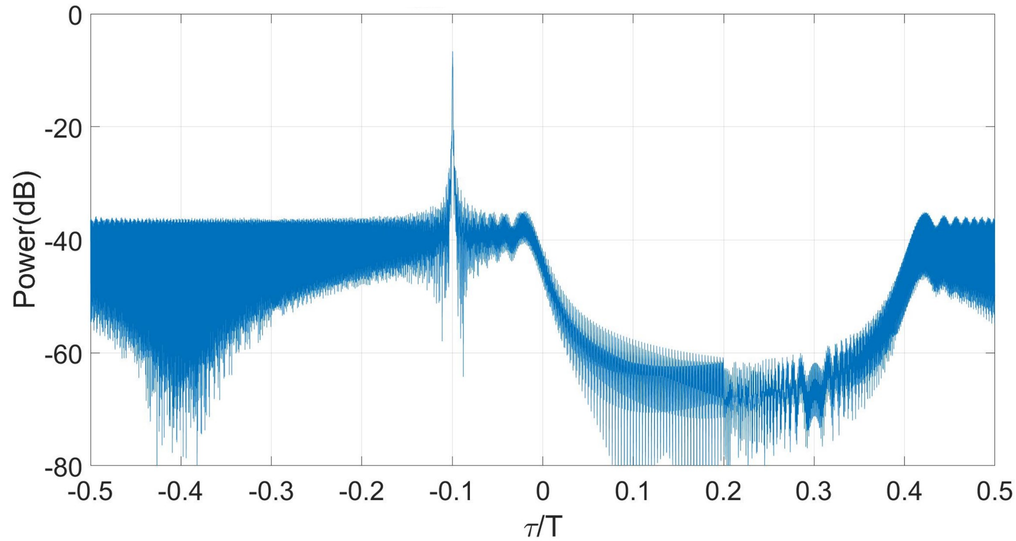

Figure 5.24: XMF $f^b_{2,\mathrm{xmf}}(t)$ output for received signal with $\tau = 0.1T$ and $f_d = 0.2B_w$

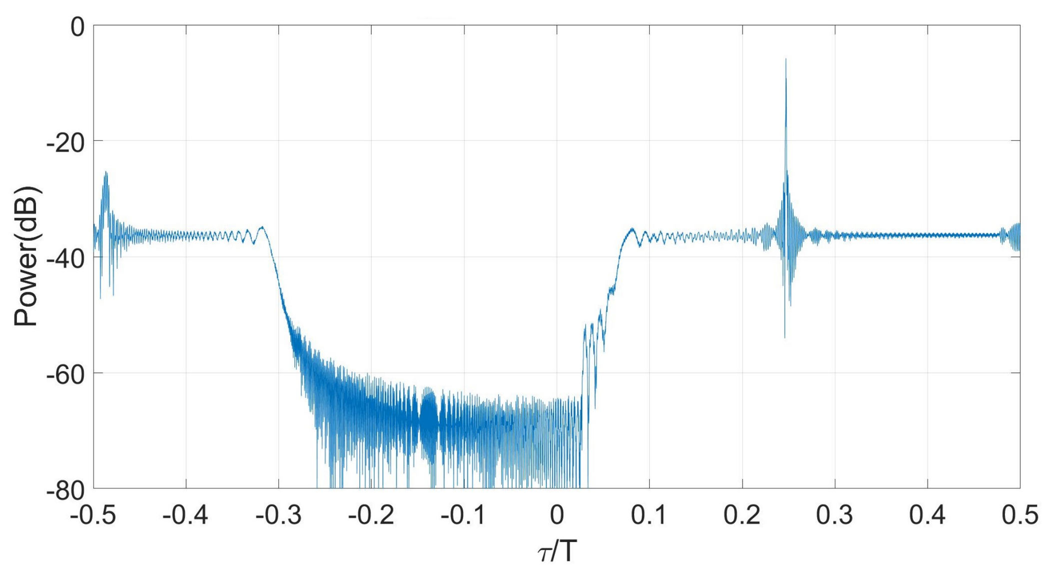

Figure 5.25: XMF $f^a_{3,\mathrm{xmf}}(t)$ output for received signal with $\tau = 0.1T$ and $f_d = 0.2B_w$

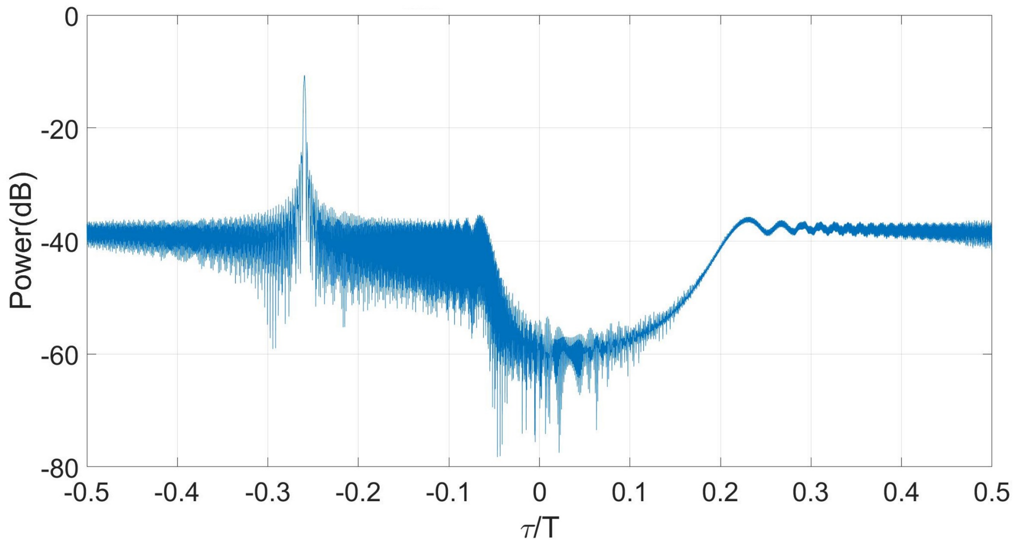

Figure 5.26: XMF $f^{b}_{3,\mathrm{xmf}}(t)$ output for received signal with $\tau = 0.1T$ and $f_d = 0.2B_w$

Table 5.1: Results of normalized delay and Doppler estimation.

i	$\hat{\tau}/T$	$\hat{f}_d/B_w$
1	0.1003	0.2
2	0.1003	0.2
3	0.1003	0.2

The results show that the estimation of delay and Doppler can be achieved properly. The error in delay estimation is the result of the sampling frequency. The errors from sampling will be addressed later.

Unlike [34] and [35], a continuous waveform is used here. Therefore, the filter outputs shift periodically according to the signal delay. Hence, the peaks inside the filter output can be related to the signal from the another period of signals. The resulting ambiguity is called range ambiguity for pulse Doppler radar systems. This ambiguity can cause errors in Doppler and range estimation. To see such effect, let us consider the case when $\tau = 0.4T$ and $f_d = 0.2B_w$. The XMF outputs of received signal is given in Fig. 5.27-5.32

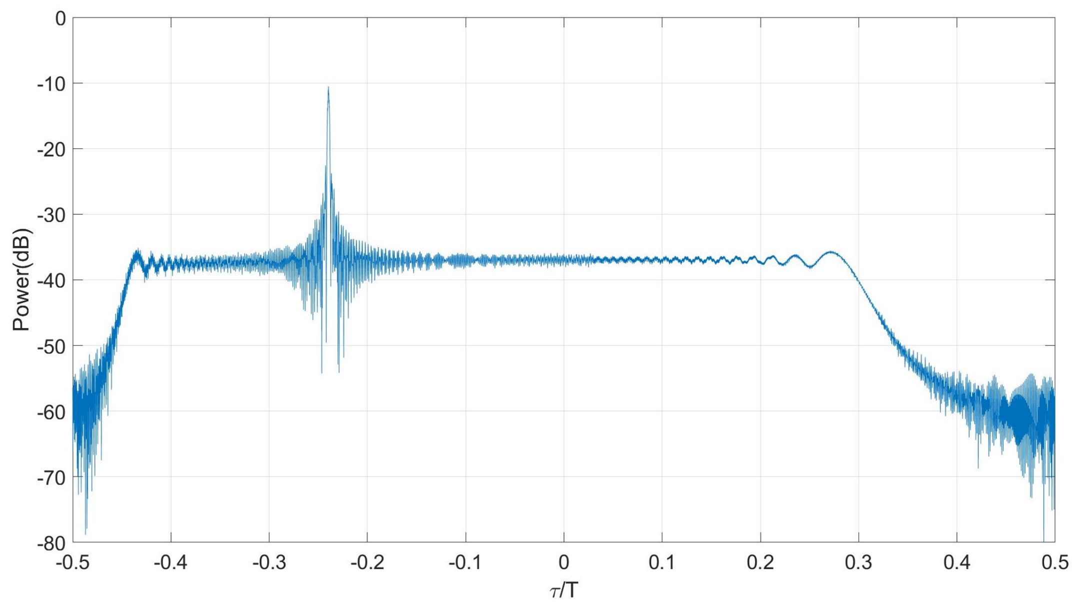

Figure 5.27: XMF $f^{a}_{1,\mathrm{xmf}}(t)$ output for received signal with $\tau = 0.4T$ and $f_d = 0.2B_w$

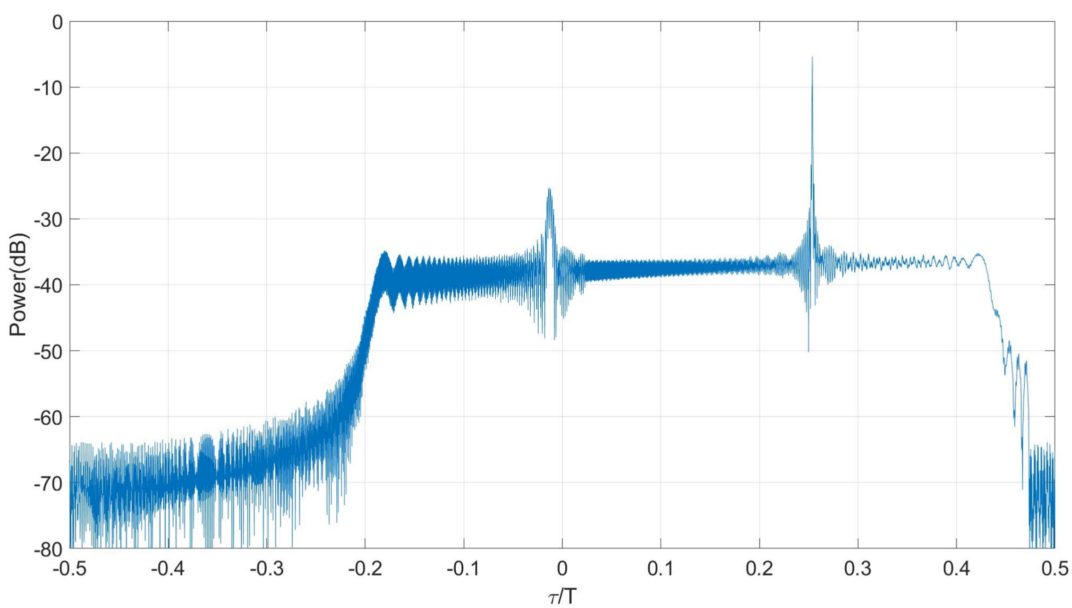

Figure 5.28: XMF $f^{b}_{1,\mathrm{xmf}}(t)$ output for received signal with $\tau = 0.4T$ and $f_d = 0.2B_w$

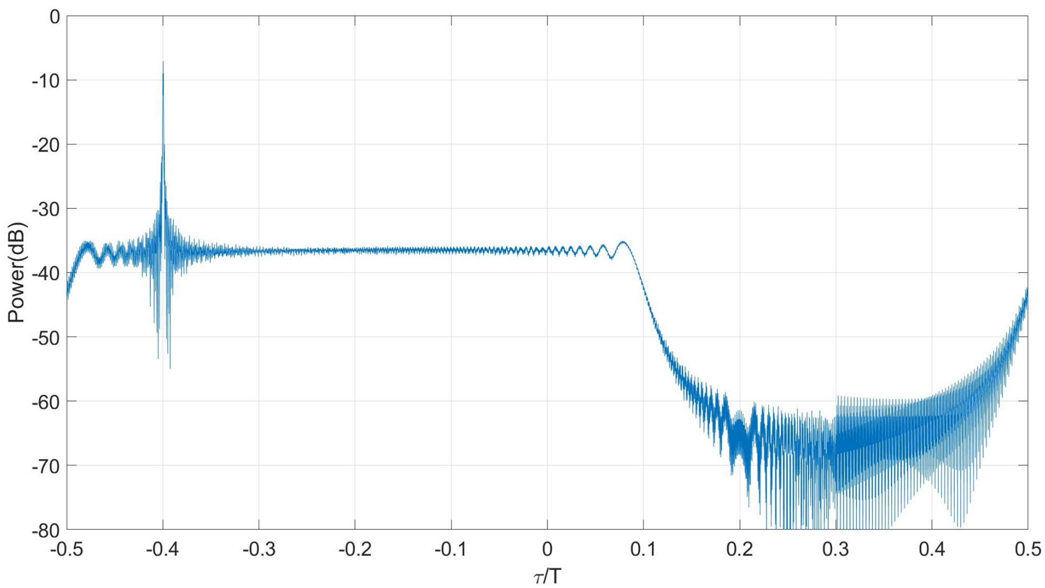

Figure 5.29: XMF $f^a_{2,\mathrm{xmf}}(t)$ output for received signal with $\tau = 0.4T$ and $f_d = 0.2B_w$

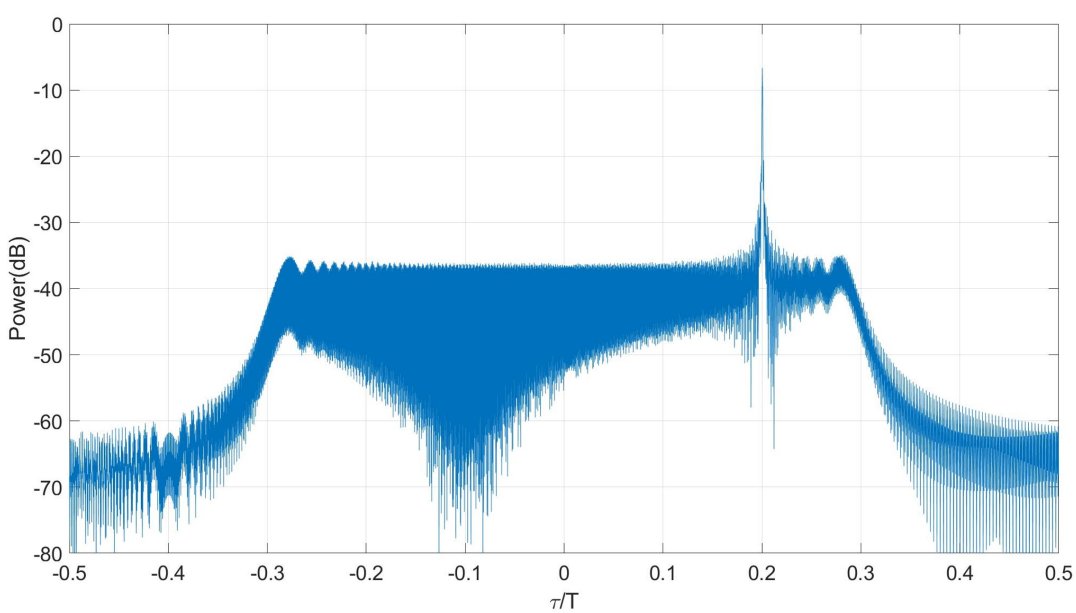

Figure 5.30: XMF $f^b_{2,\mathrm{xmf}}(t)$ output for received signal with $\tau = 0.4T$ and $f_d = 0.2B_w$

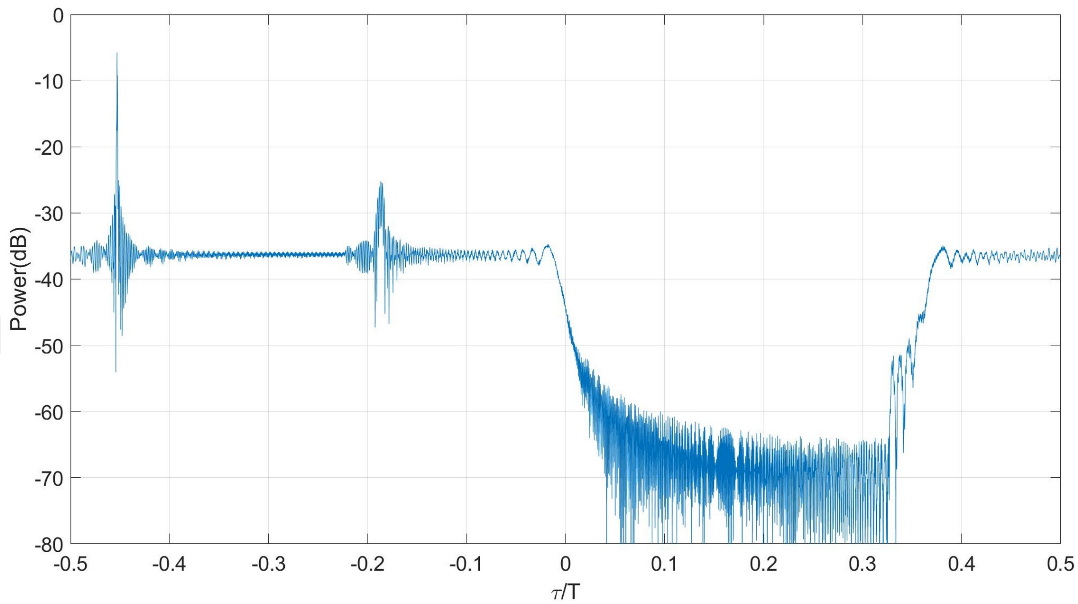

Figure 5.31: XMF $f^a_{3,\mathrm{xmf}}(t)$ output for received signal with $\tau = 0.4T$ and $f_d = 0.2B_w$

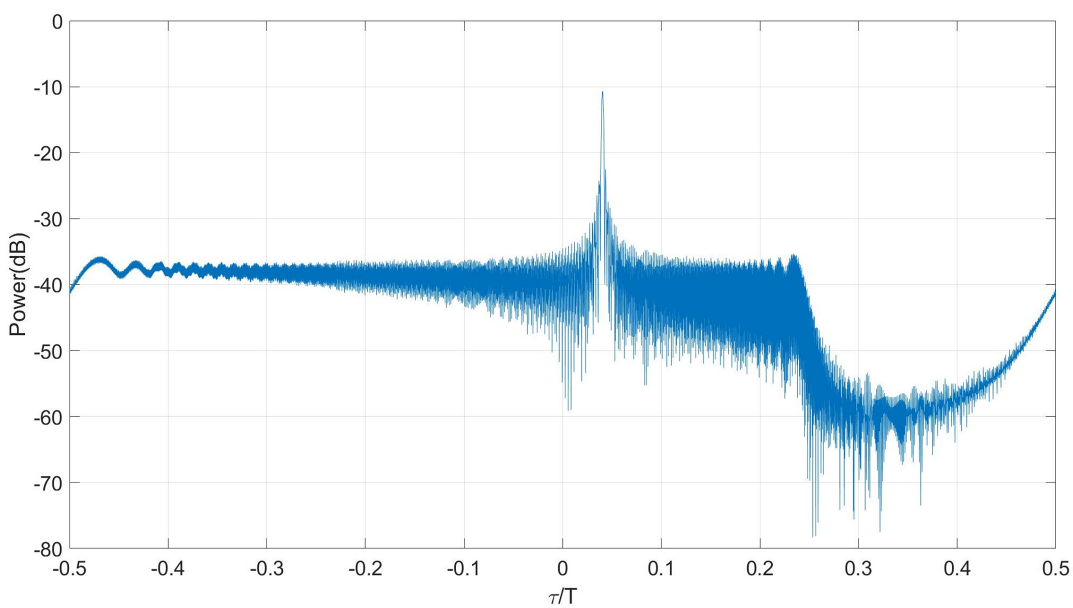

Figure 5.32: XMF $f^b_{3,\mathrm{xmf}}(t)$ output for received signal with $\tau = 0.4T$ and $f_d = 0.2B_w$

To understand the case better, let us examine the Fig. 5.29 and Fig. 5.30. Since the Doppler frequency is $f_d = 0.2B_w$, the outputs are circularly shifted version of Fig. 5.23 and Fig. 5.24. The delay difference is $0.3T$. Therefore, the peaks in Fig. 5.23 and Fig. 5.24 are circularly shifted, which results in Fig. 5.29 and Fig. 5.30. In Fig. 5.29, we can observe that the delay of the peak is at $-0.4T$ instead of $0.6T$. Hence, using (3.19) and (3.16), the target delay and Doppler are estimated. The resulting delay and Doppler are $\tau = -0.0997T$ and $f_d = -0.3B_w$. Hence, if the estimated peak points are $\hat{T_i^a} = T_i^a \mp T$ and/or $\hat{T_i^b} = T_i^b \mp T$. As we can see, the delay and Doppler estimation is severely affected by the ambiguity. As a result, the bandwidth and signal period should be selected carefully.

The cases mentioned so far have been studied for a single target. When more than one target is found, the detections observed in the matched filter outputs must be correctly associated with the targets. In Chapter 4, we propose a novel target parameter estimation in presence of multiple target using PPLFM which resolves this ambiguity. Let us consider the case when two targets are present to analyze the system. The received energy for each target and transmitter is normalized. It is assumed that the received signal from all transmitters $i = 1, 2$ and 3 with $\tau = 0T, f_d = 0.5B_w$ and $\tau = 0.3T, f_d = 0.1667B_w$ by first and second target respectively. The XMF outputs for received PPLFM from $i = 1$ is given in Fig. 5.33 and Fig. 5.34.

When Fig. 5.33 is examined, it is seen that there are two T_i^a values, and when Fig. 5.34 is examined, there are two T_i^b values. It is not known which combinations of these detections should be associated with targets. If there is a significant amplitude difference between these detections, the matching is determined by matching the detections with similar amplitudes. However, if the amplitude difference between detections is not selective enough, all possible matches should be considered. Therefore, Doppler and signal delay are estimated for each T_i^a and T_i^b mapping. In the case given as an example, since there are two targets, 4 targets are detected as can be seen in Fig. 3.9. Here, two unreal targets out of the 4 are called ghost targets. When the situation given as an example is examined, $T_i^a = 0.180T$ and $T_i^a = 0.360T$ as can be seen in Figure 38, $T_i^b = -0.073T$ and $T_i^b = 0.276T$ values are measured from Fig. 5.34. After matching the measured

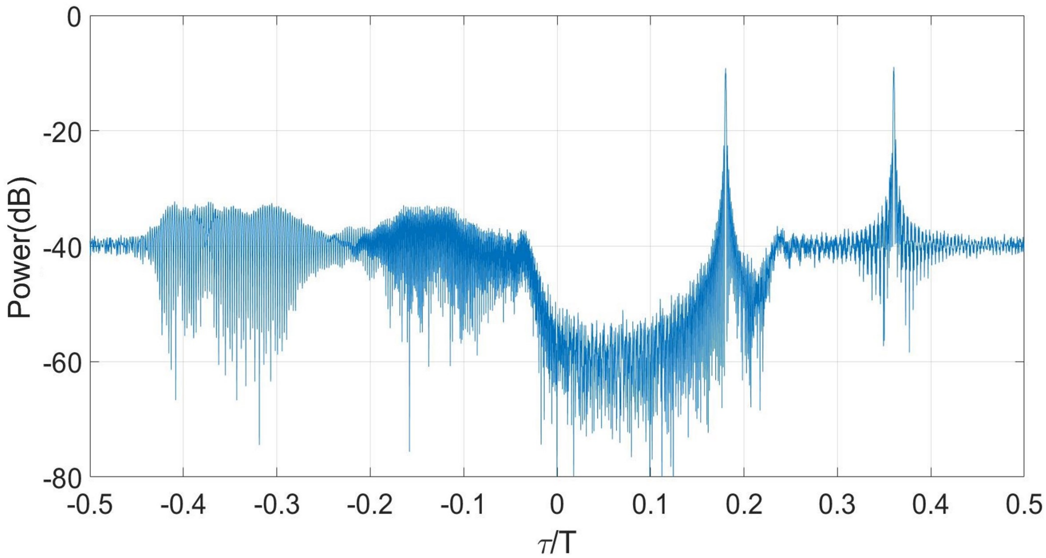

Figure 5.33: XMF $f^{a}_{1,\mathrm{xmf}}(t)$ output for received signal from targets with $\tau = 0T, f_d = 0.5B_w$ and $\tau = 0.3T, f_d = 0.1667B_w$

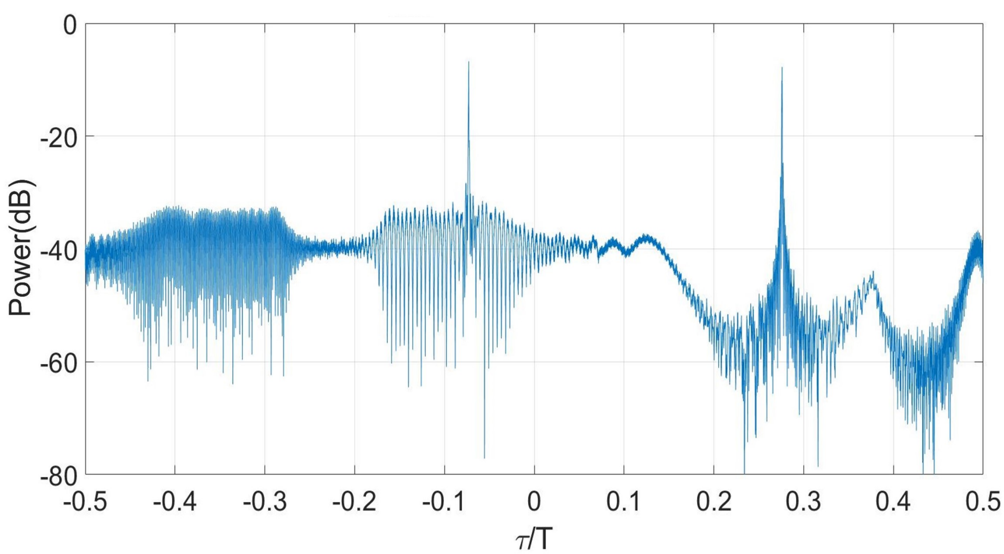

Figure 5.34: XMF $f^{b}_{1,\mathrm{xmf}}(t)$ output for received signal from targets with $\tau = 0T, f_d = 0.5B_w$ and $\tau = 0.3T, f_d = 0.1667B_w$

T_i^a and T_i^b values, signal delay and Doppler estimation are made using (3.19) and (3.16). The resulting estimations for each mapping is given in Table. 5.2.

Table 5.2: Results of delay and Doppler estimation.

T_i^a/T	T_i^b/T	$\hat{\tau}/T$	$\hat{f}_d/B_w$
0.180	-0.073	0	0.5
0.360	-0.073	0.524	0.855
0.180	0.276	0.248	0.188
0.360	0.276	0.3	0.166

Note that even there exist four possible target points, only two possible combinations are possible. The reason is that since there are two T_i^a and two T_i^b detections, there are only two permutations exist.

The results demonstrate that the range and Doppler estimation performance is promising. Despite that, the elimination of ghost targets cannot be applied easily. If any point estimation exceeds the limits, the system should perform detection for all points. But, the tracker can differentiate the ghost targets as detailed in chapter 4.

5.3 MIMO Radar System Bistatic Range Based Detection Performance Analysis

In this section, we will study the detection performance of the MIMO radar system using bistatic range measurements. A simulation environment created in 3D space. We create a scenario where there are two transmitters and six receivers that are widely separated in a region. The radars are positioned on the ground.

First, we will examine the case where two targets are flying straight in a diagonal manner. In this case, the trajectories of the targets are preferred to be in a low altitude. The reason is to study the affects of spatial diversity effectively. The mentioned scenario is shown in the Fig. 5.35.

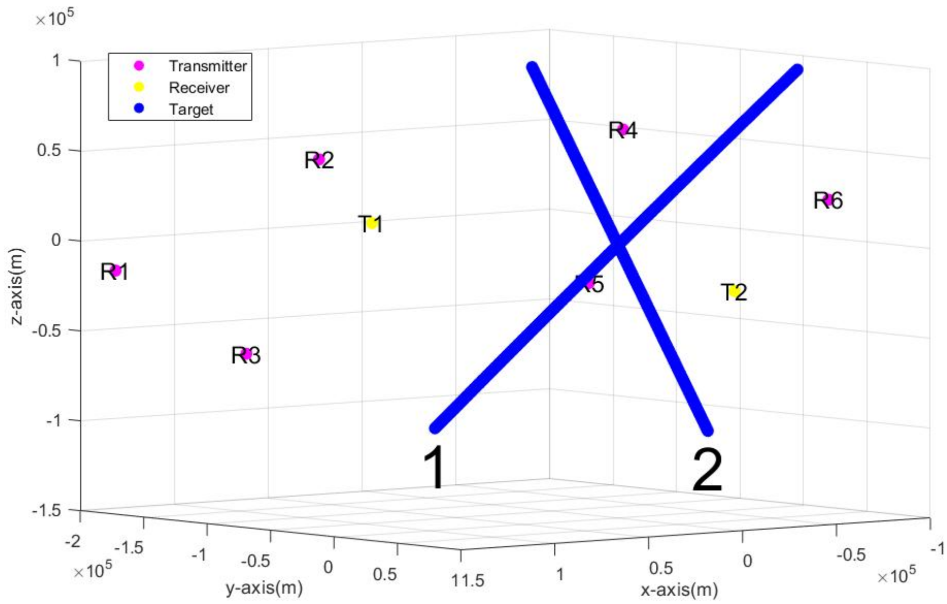

Figure 5.35: Two target crossing test scenario.

We have used F35 model as target. The F35 model is taken from [95] and the CAD model is enhanced. After that, the RCS of this enhanced model is calculated using MLFMA. The RCS values for each transmitter-receiver pair are given in Fig. 5.36 and Fig. 5.37.

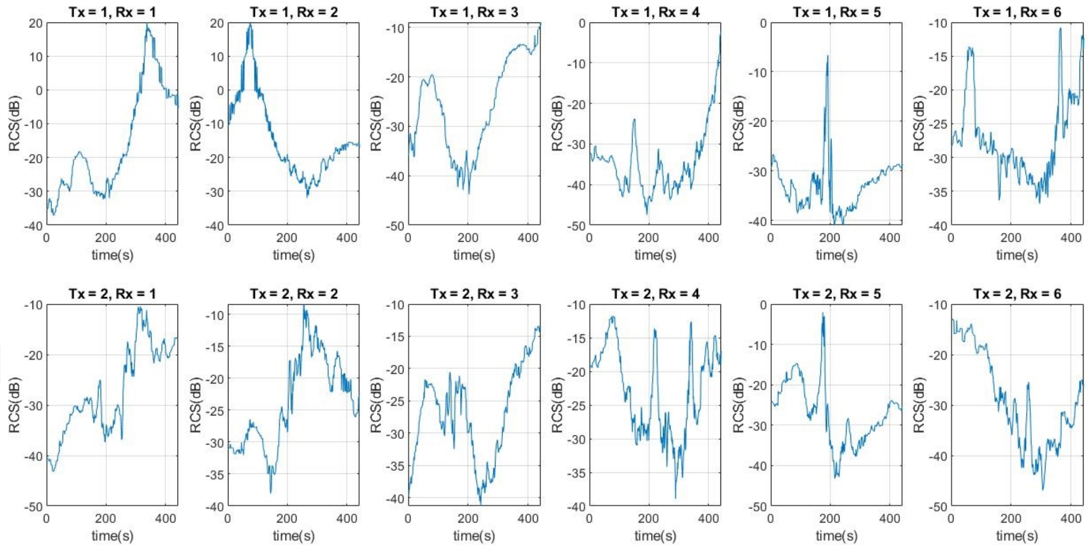

Figure 5.36: RCS of the first target for each transmitter-receiver pair over time

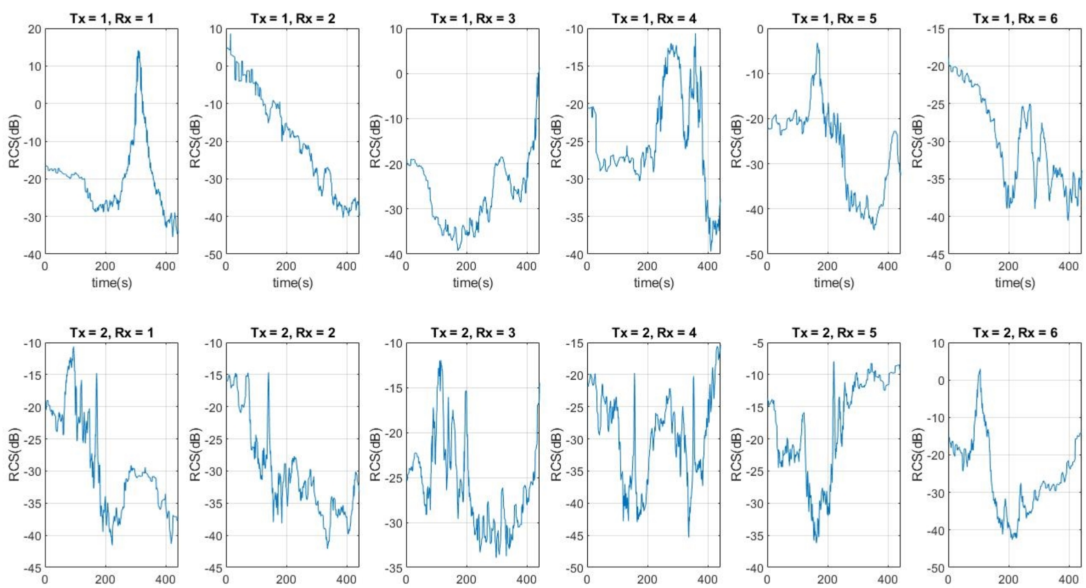

Figure 5.37: RCS of the second target for each transmitter-receiver pair over time

Besides the RCS, SNR depends on the distances of the target to the transmitter and receiver and the antenna gains. The SNR values for both targets are calculated using (4.74) which results in Fig. 5.38 and Fig. 5.39.

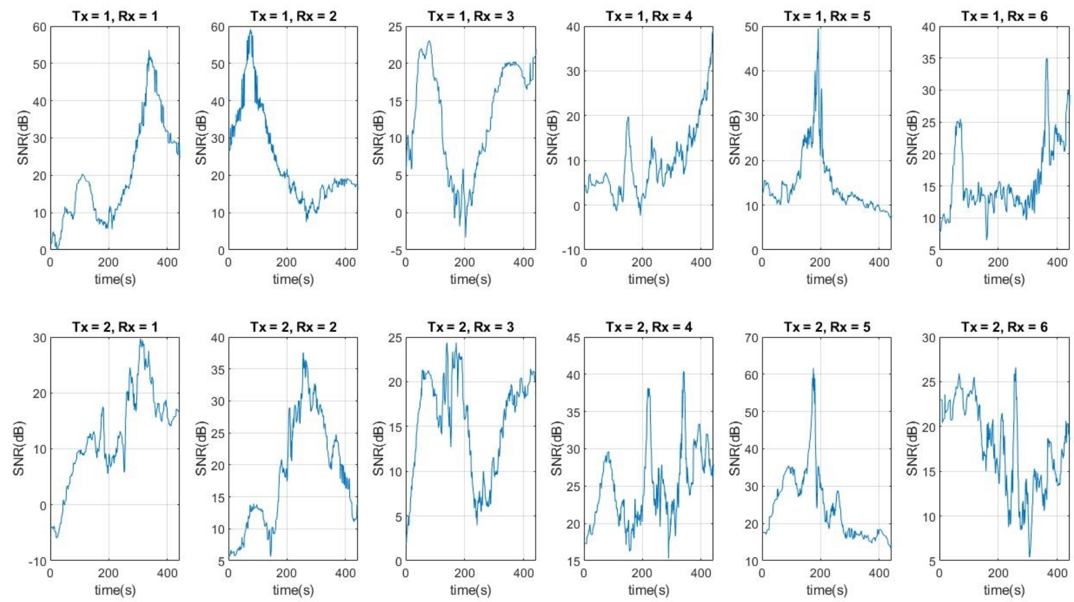

Figure 5.38: SNR of the first target for each transmitter-receiver pair over time

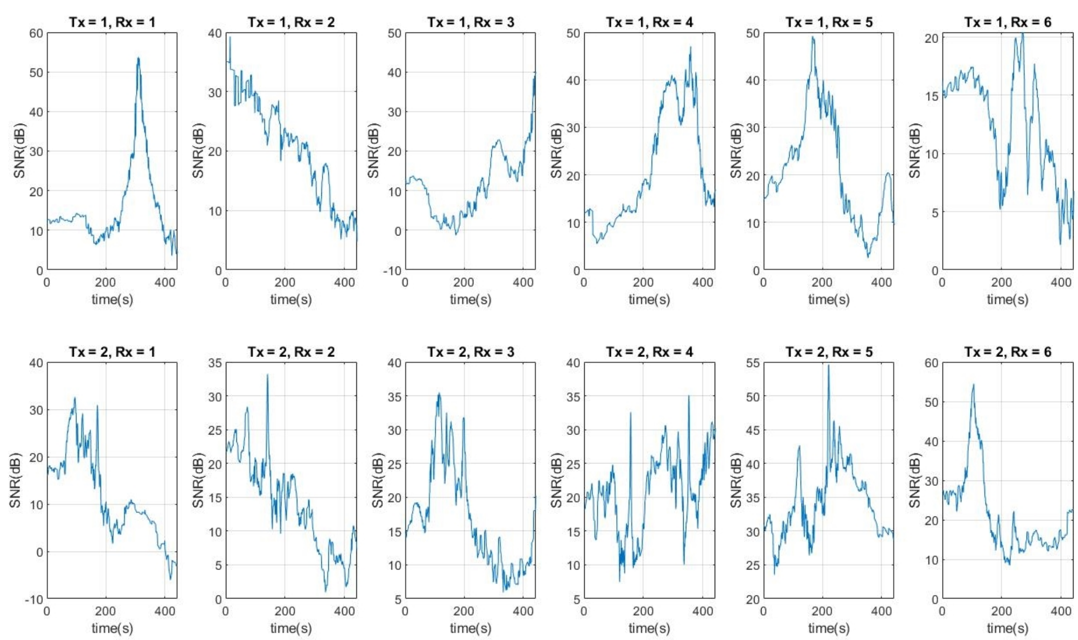

Figure 5.39: SNR of the second target for each transmitter-receiver pair over time

In simulation, receivers perform measurement with probability of detection. The Probability of detection for a radar system with coherent integration can be calculated as [51]:

$$P_D = \frac{1}{2}\text{erfc}\left(\text{erfc}^{-1}(2P_{FA}) - \sqrt{\text{SNR}/2}\right) \tag{5.2}$$

The resulting Probability of detection versus SNR for $P_{FA} = 10^{-6}$ and $P_{FA} = 10^{-8}$ is given in Fig. 5.40,

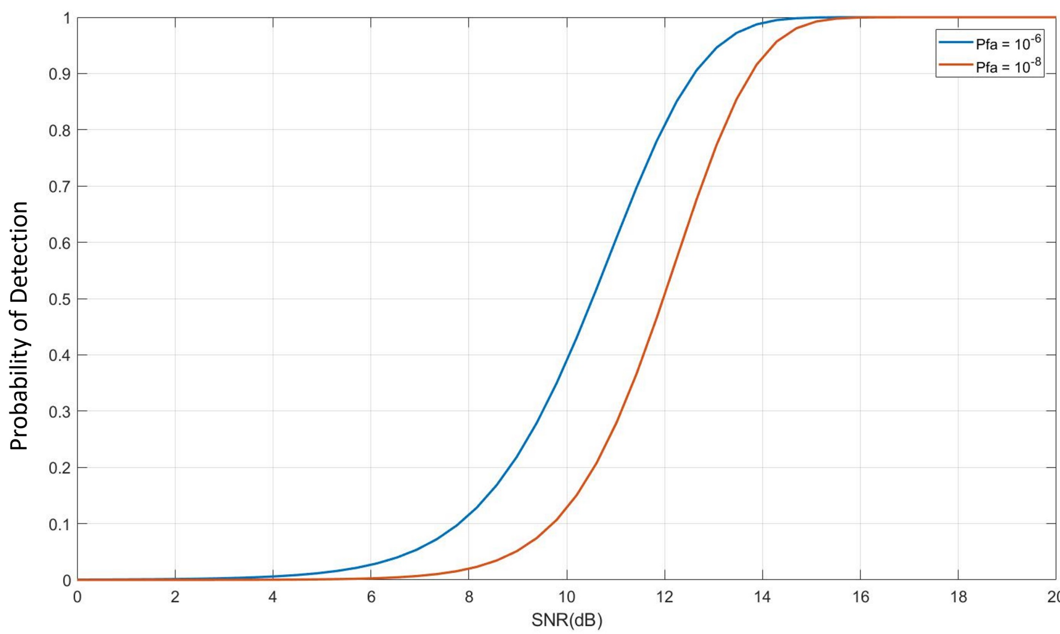

Figure 5.40: Probability of detection versus SNR for given probability of false alarms $P_{fa} = 10^{-6}$ and $P_{fa} = 10^{-8}$.

We can see from Fig. 5.40 that for $P_{FA} = 10^{-6}$, $P_D \approx 1$ where SNR > 14. Considering the SNR values given in Fig. 5.38 and Fig. 5.39, we choose $P_{FA} = 10^{-6}$ and will perform the test for that probability of detection.

Bistatic range based darget detection scheme which is presented in Sec. 4.4.1 is performed on the scenario shown in Fig. 5.35. To see the effect of γ_w, we will exhibit different results for $\gamma_w = 0.85$ and $\gamma_w = 0.7$. The results are shown in Fig. 5.41.

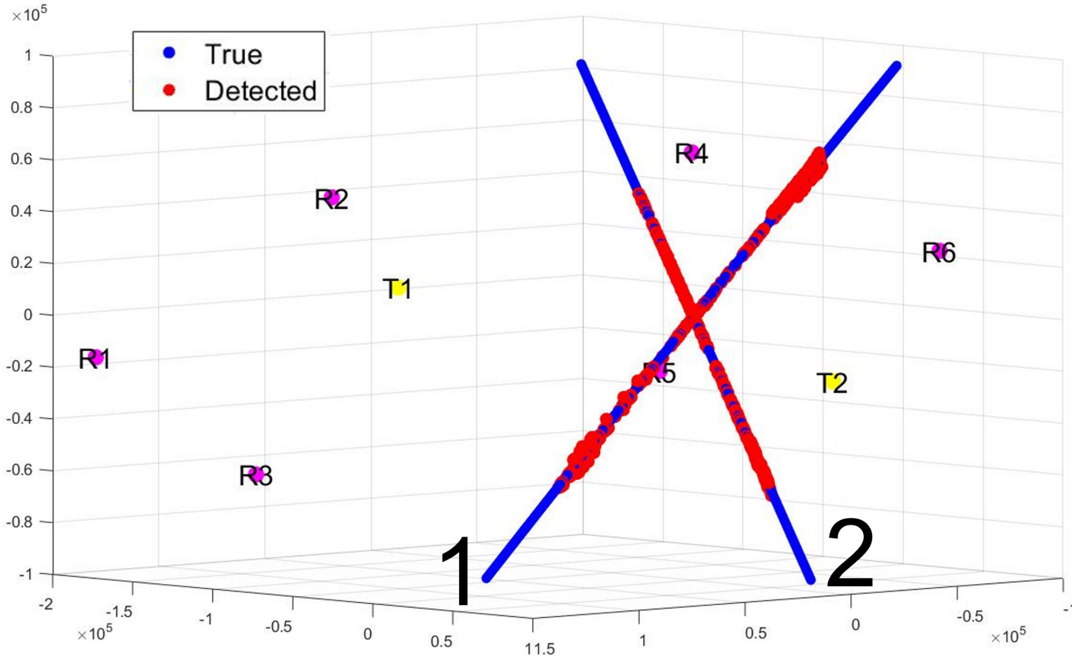

Figure 5.41: Scenario for the bistatic range based detection of targets with crossing trajectories.

We can see from Fig. 5.41 that the targets can be detected easily. However, the false alarms are made at almost every step. It is hard to evaluate the total performance and interpret the false alarms. For further investigation, we also plot and examine more figures. In Fig. 5.42, we show the number of detections over time.

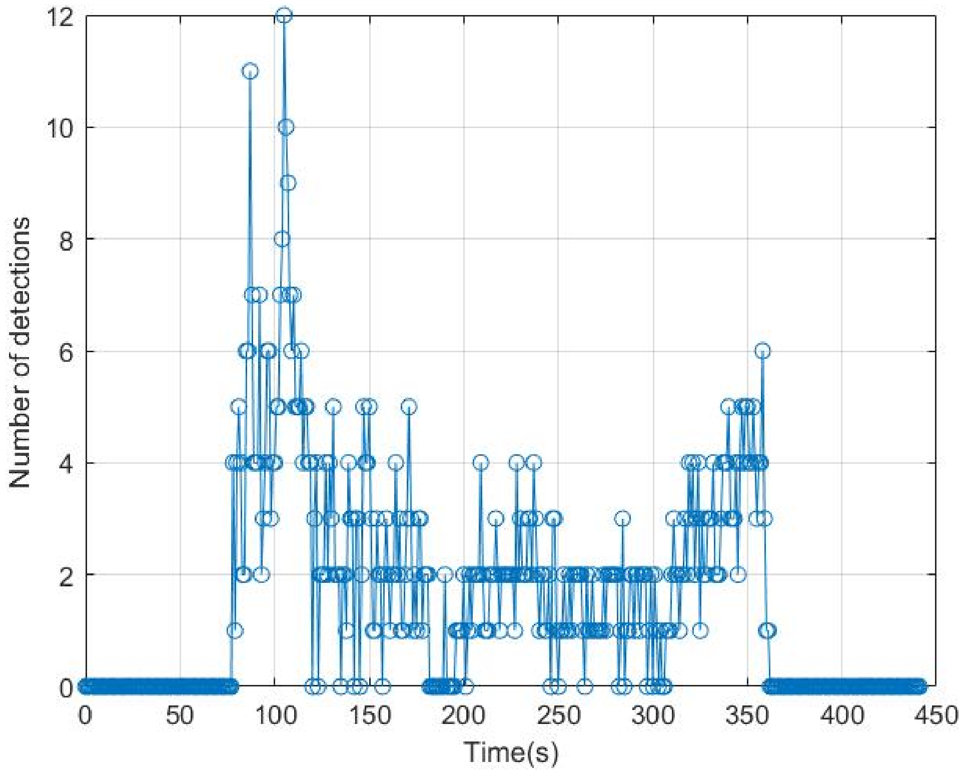

Figure 5.42: Number of detections over time for the bistatic range based detection of targets with crossing trajectories.

The results in Fig. 5.42 show us that the the number of false alarms can be even five times more than the number of targets present in the ROI. To investigate the detection performance, we have associate the detection points to the closest target and show the number of detection for each target in Fig. 5.43.

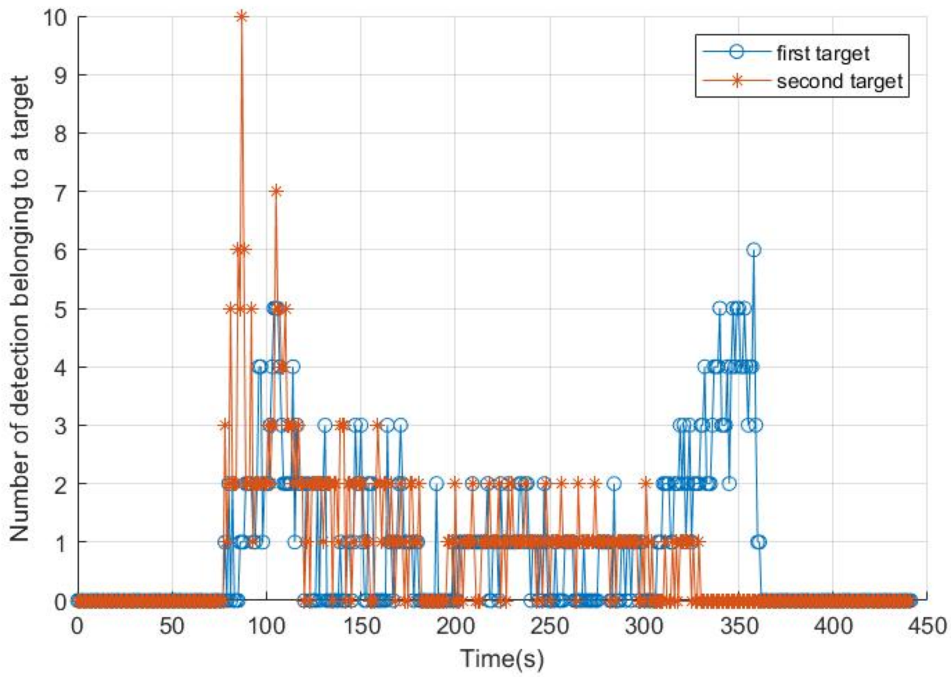

Figure 5.43: Number of detections that belong to each target over time for bistatic range based detection of targets with crossing trajectories.

Note that detection can only be performed for the time interval of 80-370s. Because targets are not in ROI except for this time interval, detection can only be achieved in ROI since we generate the grid inside ROI. The percentage of time that each target is detected, missed, and detected with any false alarm, which means that the number of detection belonging to a specific target is more than once, is given in Table 5.3. Note that the results are calculated from the 80-370s time interval.

	detection(%)	misses(%)	false alarms(%)
first target	30.8	33.7	35.5
second target	39.5	30.1	30.4

Table 5.3: For targets with crossing trajectories that are in the ROI of the MIMO detection system with $\gamma_w = 0.85$, percentage for detection and false alarms.

The results shown in Table 5.3 Shows that in 33.7% and 30.1% of time, the first and second target could not be detected respectively. As we discussed in Section 4.4.1, decreasing γ_w will increase the probability of detection and decrease probability of miss since $P_M = 1 - P_D$. Additionally, we assume that the false alarms does not effect the tracker since we can discard most of the false detections. However, it is difficult to track a target with missing detections. As a result, we also perform bistatic range based detection with $\gamma_w = 0.6$ on crossing trajectories scenario. The detection points are shown in Fig. 5.44.

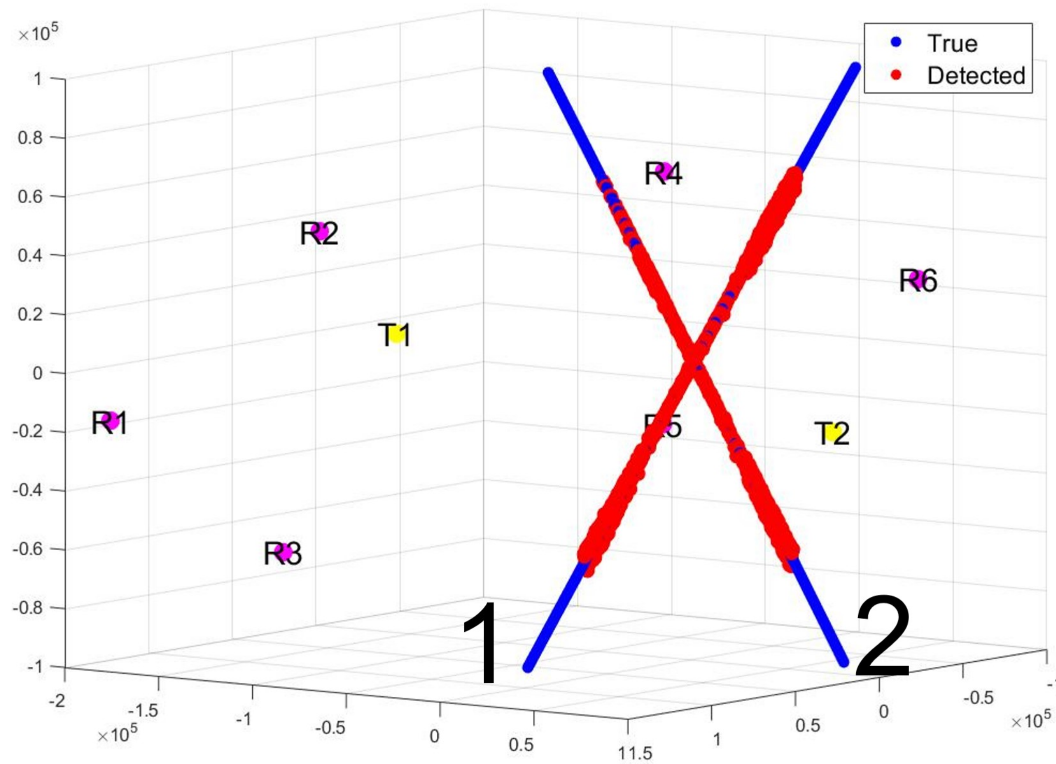

Figure 5.44: Scenario for the bistatic range based detection with $\gamma_w = 0.6$ of targets with crossing trajectories.

The number of detections associated to both targets over time is shown in Fig. 5.45 and the detection percentages are given in Table 5.4

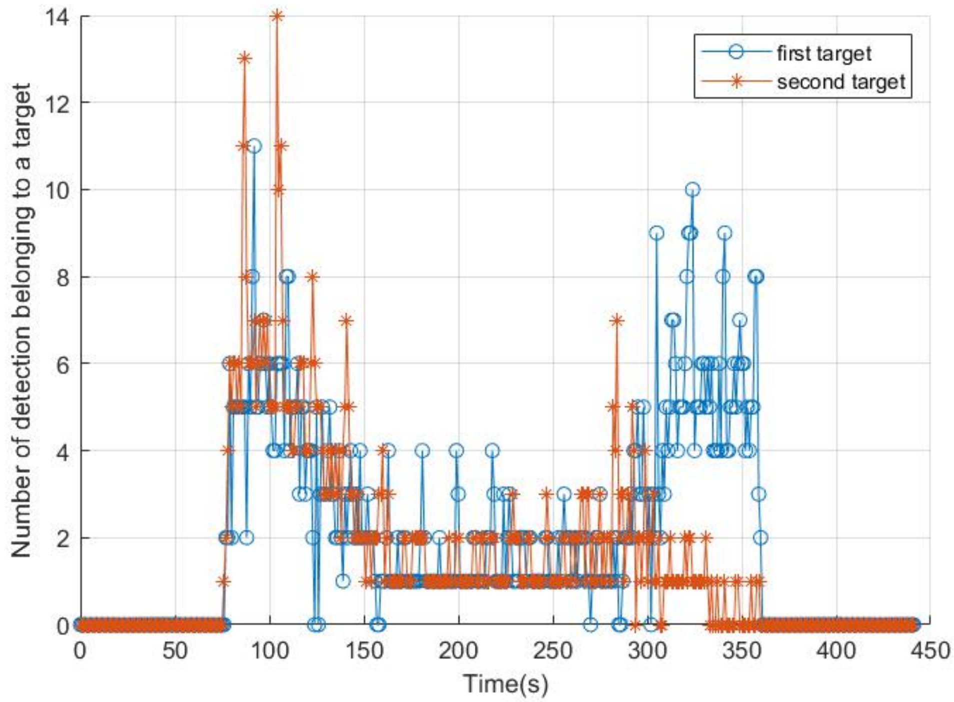

Figure 5.45: Number of detections that belong to each target over time for bistatic range based detection with $\gamma_w = 0.6$ of targets with crossing trajectories.

	detection(%)	misses(%)	false alarms(%)
first target	30.1	2.9	67
second target	37.7	7.2	55.1

Table 5.4: For targets with crossing trajectories that are in the ROI of the MIMO detection system with $\gamma_w = 0.6$, percentage for detection and false alarms.

The results given in Fig. 5.45 and Table 5.4 shows that the targets are detected properly. On the other hand, there are more than one detection is performed at almost two times more than the cases where only one detection is performed for a target.

5.4 MIMO Radar System Iterative Position and Velocity Performance Analysis

We will study position and velocity estimation performance of the system proposed in Section 4.5 on the detection points of the crossing trajectories scenario. First, the detection points are associated with bistatic measurement as explained in Section 4.5.2. Afterwards, the position and velocity of each detection point is estimated by using the proposed algorithm given in 1. The initial position is selected as the position of the interested detection point and the velocity is initialized as zero. The estimated and true positions are given in Fig. 5.46 and Fig. 5.47.

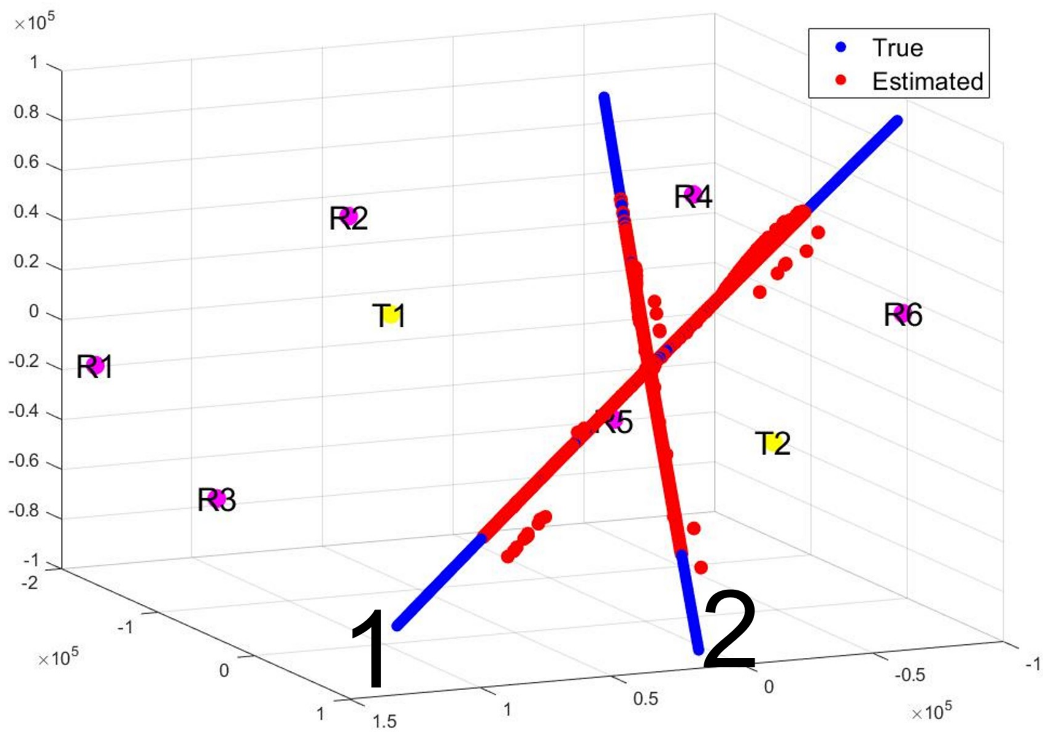

Figure 5.46: The iterative positioning results of targets with crossing trajectories with the detections points given in Fig. 5.46

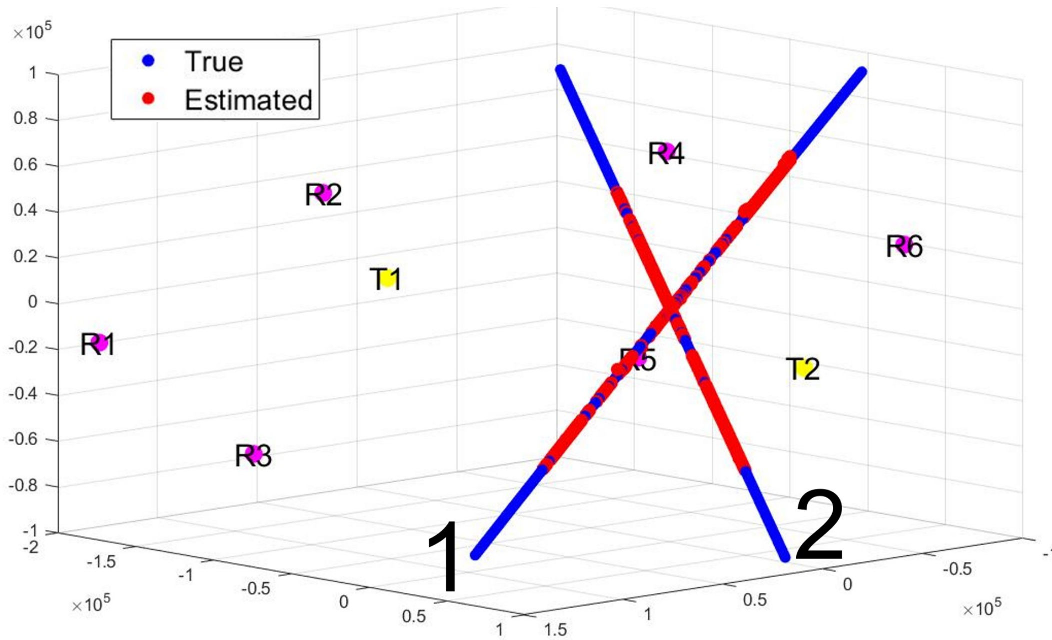

Figure 5.47: The iterative positioning results of targets with crossing trajectories with the detections points given in Fig. 5.41.

The position and velocity estimation error of these points are given in Table 5.5. The values in the table are calculated by associating each estimation point to the closest target and calculating the distance between the estimation and true positions that are given in Fig. 5.46 and Fig. 5.47. For the sake of simplicity, let us define $\mu_{\boldsymbol{P}} = E\left[\left\|\boldsymbol{P} - \hat{\boldsymbol{P}}\right\|\right]$ and $\mu_{\boldsymbol{V}} = E\left[\left\|\boldsymbol{V} - \hat{\boldsymbol{V}}\right\|\right]$ be the mean of the position and velocity estimation error over the full flight. Also let $\sigma_{\boldsymbol{P}} = E\left[\left\|\boldsymbol{P} - \hat{\boldsymbol{P}}\right\|\right]$ and $\sigma_{\boldsymbol{V}} = E\left[\left\|\boldsymbol{V} - \hat{\boldsymbol{V}}\right\|\right]$ be the standard deviation of the position and velocity estimation error over the full flight.

	$\mu_{\boldsymbol{P}}$(m) and $\mu_{\boldsymbol{V}}$(m/s)	$\sigma_{\boldsymbol{P}}$(m) and $\sigma_{\boldsymbol{V}}$(m/s)
first target	664.7, 27.6	2680.7, 36.8
second target	217.6, 32.8	1652.4, 52.7

Table 5.5: For the proposed iterative position and velocity estimation technique obtained position and velocity estimation errors for crossing trajectories.

By making further investigation, it is seen that in almost 87% of the time, the position estimation error is lower than 50m which is the range resolution. Furthermore, in almost 90% of the time, the error is lower than 200m. It is obvious from Fig. 5.46 and Fig. 5.47 that small number of estimations are considerably far from the true points. Additionally, the velocity estimation error is lower than 20m/s for more than 65% of the time. This means that the results given in Table 5.5 can lead to misunderstand the system performance.

In conclusion, MIMO radar multiple target policy-iteration-based position and velocity estimation performance is satisfying.

5.5 EMVS-MIMO Radar System Performance Analysis

In this section, we will study MIMO radar systems with widely separated antennas which are EMVA. To evaluate the performance, models for DOA estimation performance are investigated. In [60], CRBs for angle estimation errors are derived. MSE and covariance of error of angle estimations are given as:

$$\mathrm{MSAE}_{CRB} = \frac{180}{\pi}\frac{(1+\mathrm{SNR})(\sigma_E^2+\sigma_H^2)^2}{2\mathrm{SNR}^2\left[\sigma_E^2\sigma_H^2+\left(\sigma_E^2-\sigma_H^2\right)^2\sin^2\varphi\cos^2\varphi\right]}, \tag{5.3}$$

and covariance matrix of angle estimation error (CVAE) is a 3×3 diagonal matrix. The column and row order is θ, ϕ, ϑ respectively. The non-zero terms of the matrix are

$$[\mathrm{CVAE}_{CRB}]_{1,1} = \frac{180}{\pi}\frac{(1+\mathrm{SNR})}{2\mathrm{SNR}^2\cos^2 2\varphi}, \tag{5.4a}$$

$$[\mathrm{CVAE}_{CRB}]_{2,2} = \frac{180}{\pi}\frac{(1+\mathrm{SNR})(\sigma_E^2+\sigma_H^2)}{2\mathrm{SNR}^2[\sigma_H^2\sin^2\varphi+\sigma_H^2\cos^2\varphi]}, \tag{5.4b}$$

$$[\mathrm{CVAE}_{CRB}]_{3,3} = \frac{180}{\pi}\frac{(1+\mathrm{SNR})(\sigma_E^2+\sigma_H^2)}{2\mathrm{SNR}^2[\sigma_E^2\sin^2\varphi+\sigma_H^2\cos^2\varphi]}, \tag{5.4c}$$

where σ_E and σ_H are variances of noise in electric and magnetic field. Note that the total noise variance is

$$\sigma_n^2 = \frac{\sigma_E^2 \sigma_H^2}{\sigma_E^2 + \sigma_H^2}. \tag{5.5}$$

We consider the case that noise is AWGN and has equal variances in electric and magnetic field. We study the case for linearly polarized signals. The CRB for azimuth and elevation angle estimation error variance against SNR is given in Fig. 5.48.

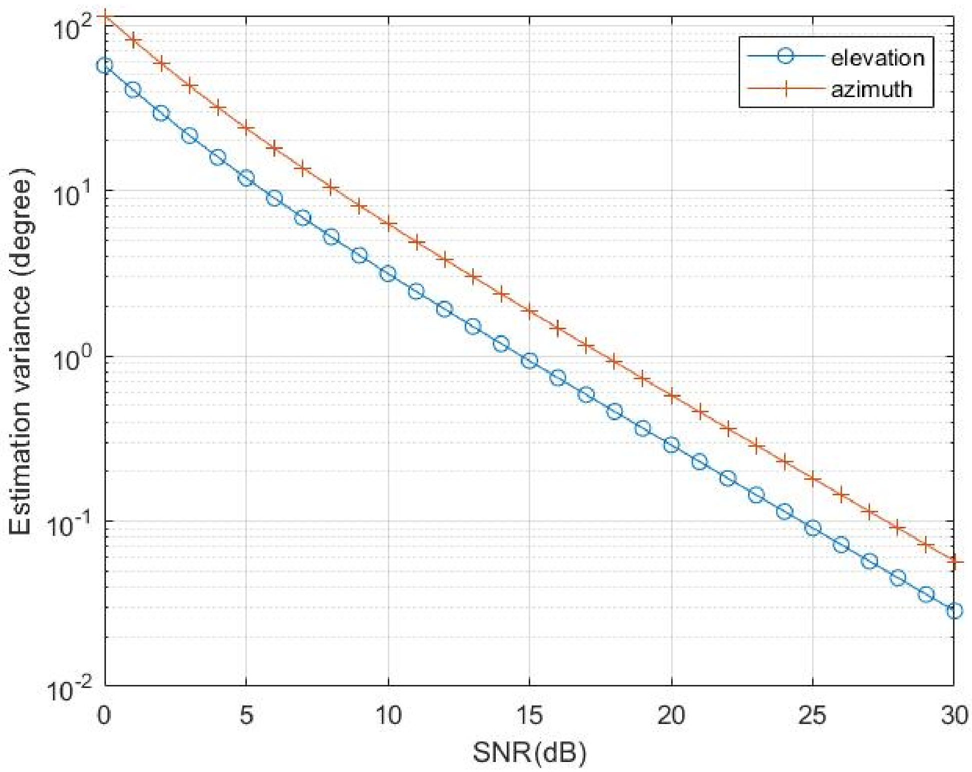

Figure 5.48: CRB for azimuth and elevation estimation error variance using an EMVA for linearly polarized signal.

In each simulation, we assume that the antenna gain of EMVA is 3dB in any direction. The assumption is made to show that even with a considerably small antenna gain, EMVA performs quite adequately. By using the aforementioned assumptions, we have studied the performance of proposed EMVS-MIMO radar system. The performance is tested on the scenario given in Fig. 5.35.

We will first study the effect of ψ_w in (4.82) on total detection performance of the system. In Fig. 5.49 and, 5.50 the detection performance of EMVS-MIMO Radar with $\psi_w = 0.5$ is shown.

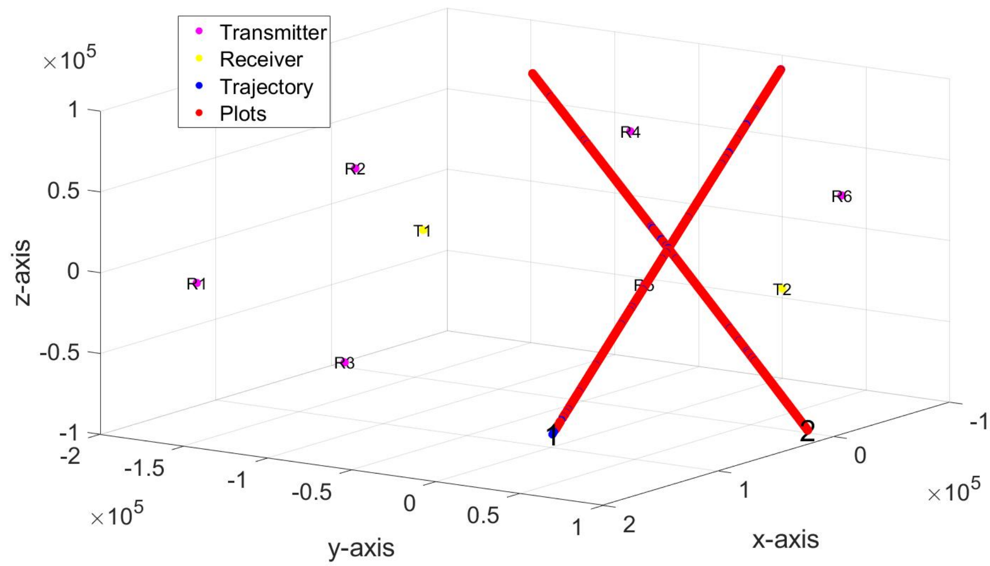

Figure 5.49: Detection performance of the EMVS-MIMO radar system using $\psi_w = 0.5$ in the scenario for targets with crossing trajectories. The target i.d.s are indicated below under the trajectories.

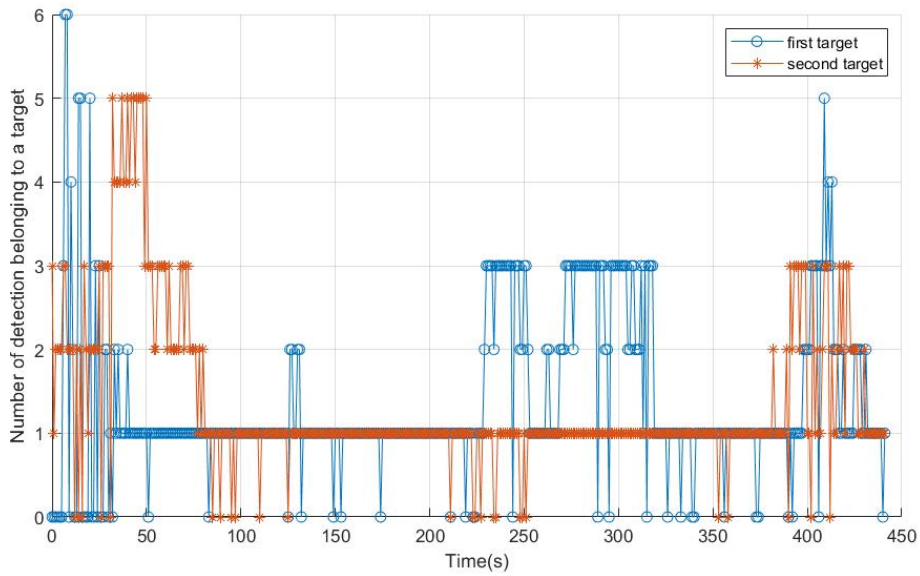

Figure 5.50: Number of detections of EMVS-MIMO radar with $\psi_w = 0.5$ on crossing trajectory scenario.

As seen, most of the time, both targets are detected. On the other hand, some regions have low detection performance. Before going into evaluation the effects of ψ_w, we will first explain other sources of missing target on the result given in Fig. 5.49.

At the beginning, the detection performance decreases due to the decrease in the SNR value. Let (k, l) be the transmitter and receiver indices. As seen in Fig. 5.38 and Fig. 5.39, the SNR of bistatic pairs (1,1), (1,3), (1,4), (2,1), (2,2), (2,3) for the first target is below 10dB at the beginning. Since we know from Fig. 5.40 that the probability of detection is lower than 0.4. Hence, signal reflected from the first target are probably cannot be detected by the bistatic pairs given above. As a result, there are inadequate number of measurements are obtained and the target detection are most probably cannot be performed in the time interval 0-30s.

There are several reasons causing low SNR. From the bistatic radar equation given in (4.74), we know that the SNR is propotional to the RCS and inversely proportional to the square of the distance to the transmitter times distance to the receiver. Since the transmitters and receivers are far from the target, SNR decreases considerably, so not enough measurement can be made to detect the target. Additionally, in Fig. 5.36 and Fig. 5.37, we can see that the RCS value of the first target for the bistatic pairs given above are around -30 and -40dB. As a result, the SNR is reduced significantly.

Note that the measurements are made probabilistically. To see the effect of ψ_w, we perform detection for several times and analyse the total performance. The for $\psi_w = 0, 0.5, 1$ values are given in 5.6.

	detection(%)	misses(%)	false alarm(%)
μ, σ^2 % for $\psi_w = 0$	90.84,0.91	4.80,0.88	4.36,0.08
μ, σ^2 % for $\psi_w = 0.5$	91.05,0.71	4.51,0.80	4.43,0.05
μ, σ^2 % for $\psi_w = 1$	90.80,0.87	4.80,0.84	4.40,0.04

Table 5.6: EMVS-MIMO radar detection performance for tested ψ_w values.

It is seen from Table 5.6 that the best performance is achieved for $\psi_w = 0.5$. In other words, using both bistatic range and DOA in weight calculation provides the best performance. Hence, we will analyze the weight function with $\psi_w = 0.5$. It was expected because using more than one type of measurement at the same time provides more information than using one type of measurement alone.

Another critic parameter is γ_d. As it is observed from Fig. 5.50, around 223s, where two targets pass close to each other, no target detection could be performed. The main reason for this is that only one set of intersection points is created in this region. Hence, we will examine the effects of the γ_d value causing this decrease in target detection performance.

In Fig. 5.49 and Table 5.6, $\gamma_d = 500m$. To enhance the target detection performance in the aforementioned region where the two targets pass close to each other, we performed the test again for different γ_d values. The test results are shown in Table 5.7.

	detection(%)	misses(%)	false alarms(%)
μ, σ^2 % for $\gamma_d = 200m$	91.09,0.56	4.52,0.52	4.39,0.09
μ, σ^2 % for $\gamma_d = 1000m$	90.30,0.82	5.33,0.75	4.38,0.09
μ, σ^2 % for $\gamma_d = 2000m$	89.68,0.63	5.90,0.68	4.41,0.07

Table 5.7: EMVS-MIMO radar detection performance for tested γ_d values.

The results given in Table 5.7 show a trade-off between missing the targets when they are close and missing the targets due to noisy measurements. For small values of γ_d, the measurements related to different targets can be easily distinguished. Thus, detection of targets which are close to each other is more likely to be achieved. However, when the measurements are obtained in a noisy environment, the measurements that are belong to one target will be clustered to different sets. As a result, the target may be missed if all regions created by each set will not include the regions or there may be more than one detection if the regions of the sets intersect. For high values of γ_d, it is more likely to avoid false alarms since only one grid is generated inside the region. On the other hand, target detection may not be performed if a noisy measurement confines the region from the wrong aspect.

Comparing the detection performance of the EMVS-MIMO radar system with the conventional MIMO radar system, it is clear that the EMVS-MIMO radar detection system outperforms conventional MIMO radar especially for the reduction of false alarm. The main reason is that DOA measurements offer a geometrically beneficial information to the system. It is desired that the weight values in the neighboring grid points to be small enough to prevent false alarm. The DOA measurements confines the possible target region and help system reduce the weight values of the neighboring points, hence reduces false alarms. We also see that EMVS-MIMO radar detects ≈ 90 faster than performing a grid search. The main reason is that instead of generating a vast amount of grid points and calculating a weight value for each, EMVS-MIMO generates a comparably and significantly small number of grid points. Also, the EMVS-MIMO provides unlimited ROI since it creates grid points around the measurement region. On the other hand, standard MIMO radar systems can only perform detection in the predefined ROI since it only creates the grid points inside of the ROI. As a result, EMVS-MIMO radar system is more beneficial than the standard MIMO radar systems.

5.6 MIMO Radar GLMB Filter Based Tracker Performance Analysis

In this section, we will perform GLMB filter based tracking that is proposed in Section 4.6 on the detection points that are given in Fig. 5.46 and Fig. 5.49 and analyse the performance. Note that the state vector includes a position and velocity estimation as given in (4.88). For that reason, the tracker uses position and velocity estimation results directly that are given in Fig. 5.46. On the other hand, position and velocity estimation is not performed for the EMVS-MIMO radar detection points. Hence, only the position information is used for tracking. In other words, the state vector is 6 dimensional while the observations are 3 dimensional.

First, we perform GLMB filter based tracker estimation point given in Fig. 5.46. The resulting tracking trace of the system and the cardinality are shown in Fig 5.51 and Fig. 5.52.

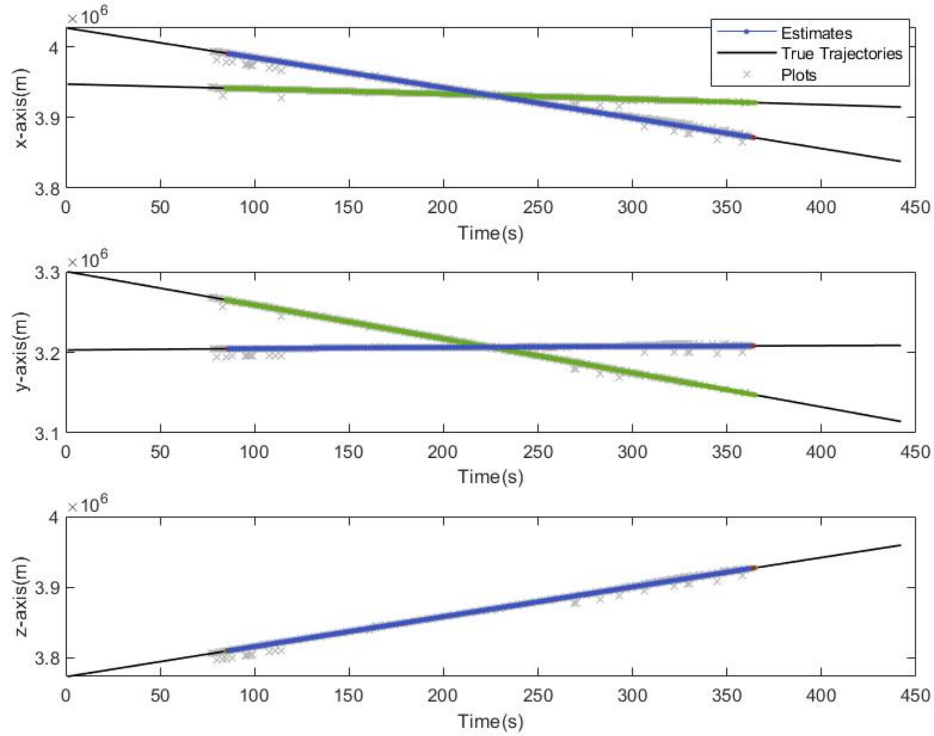

Figure 5.51: Tracking trace of the GLMB-based tracker on estimation points given in Fig. 5.46. Each color expresses unique target trace.

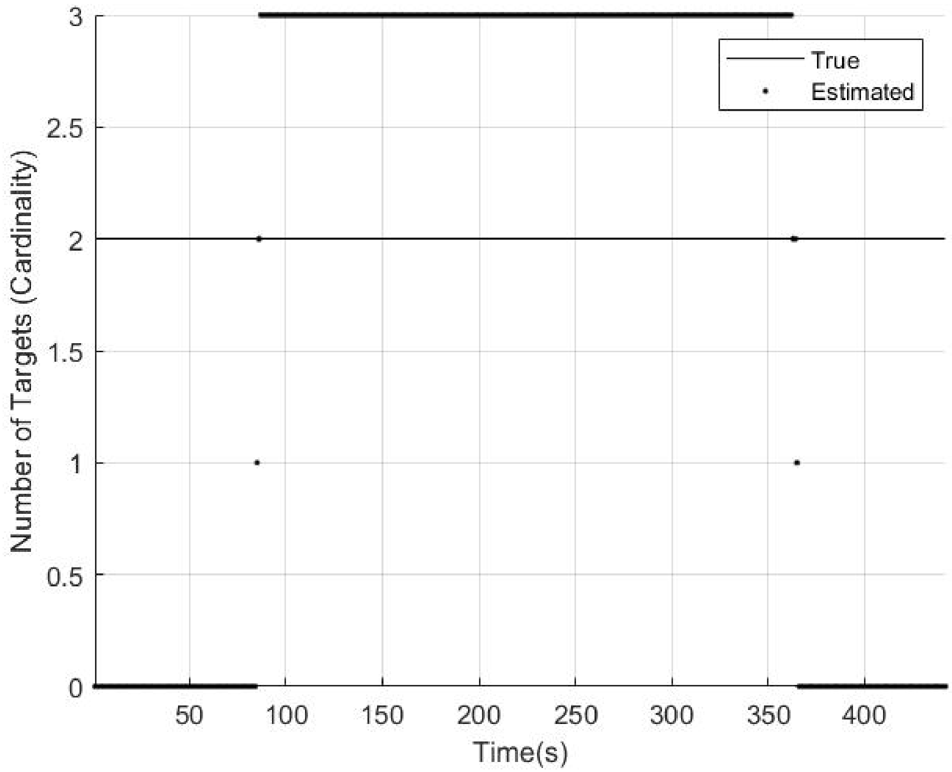

Figure 5.52: True and estimated cardinality over time for the estimations given in Fig. 5.46.

As it is seen, the tracking o a target can be performed adequately. However, the system has some imperfections.It is not clear from Fig. 5.51 that there are more than two target trace. However, Fig. 5.52 shows that the tracker also performs another target tracking which is a false alarm. This erroneous trace is shown with a red trace within the blue trace in Fig. 5.51. If the figure is examined more carefully, this trace can be seen around the 360s. The reason for the false alarm is the ghost targets obtained in the detection phase by false detection. The position and velocity of these ghost targets are enhanced and gets closer to the closest targets since the measurements that are close enough to the point are associated as explained in Section 4.5.2. As a result, there will be several detection points close to one target. If these ghost targets continue to be generated for a target, the system will detect these ghost targets as a different targets. To prevent false traces, the estimations that are very close to each other can be assembled.

Another difficulty the system encounters is the initializing of a target trace. In order start tracking, a target the system must calculate probability of existence of a target must exceed a specified value. The system creates possible trajectories by associating the plots for the next state and calculate probability of existence for each. To increase the probability of existence, the position and velocity of the plots inside a small time interval should be sufficiently close to the target. If not, the probability of existence will not be sufficient to start tracking. Additionally, the probability of birth is determined by the system and can be increased to start tracking by increasing it. However, increasing the probability of birth may increase the false alarm in the tracking.

Now, let us perform tracking for the EMVS-MIMO radar. The detection points given in Fig. 5.49 are used as plots. The GLMB-based tracking performance are given in Fig. 5.53 and Fig. 5.54.

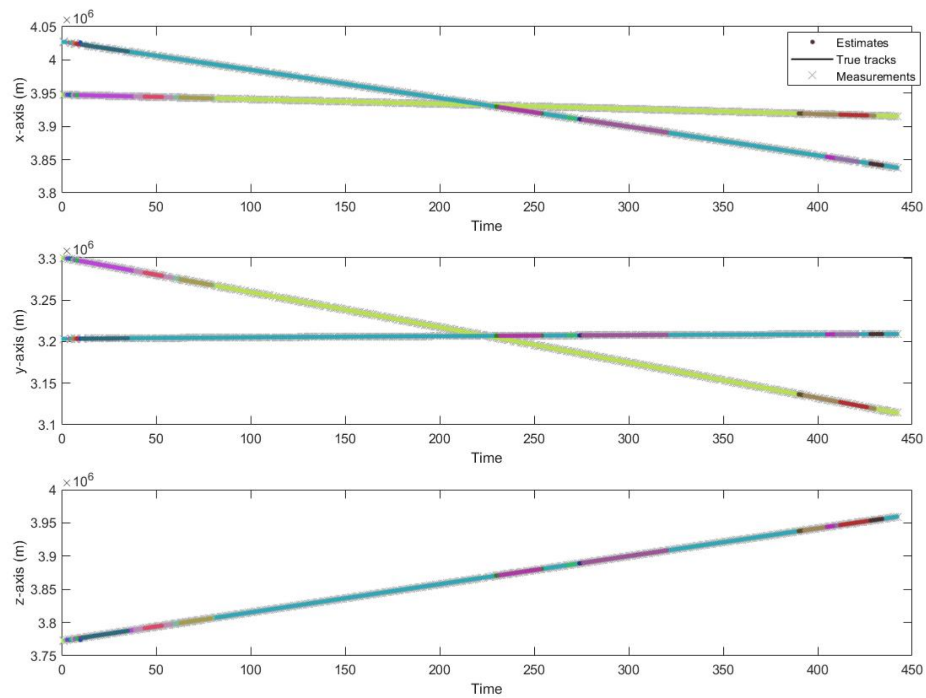

Figure 5.53: Trace of the GLMB based tracker on estimation points given in Fig. 5.49. Each color expresses a unique target trace.

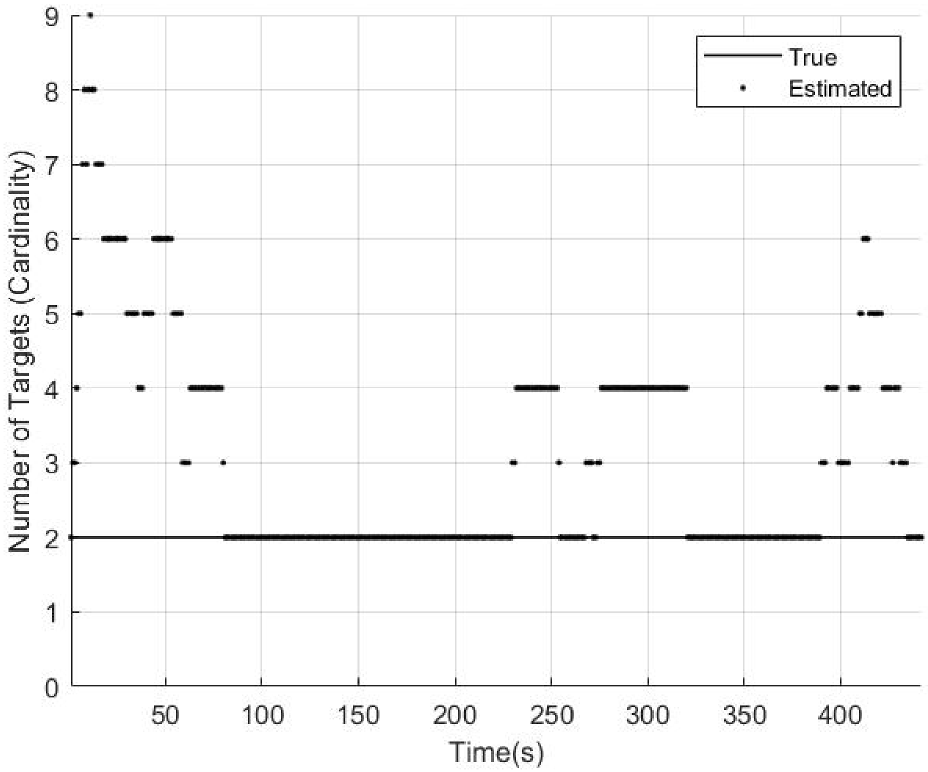

Figure 5.54: True and estimated cardinality over time for the estimations given in Fig. 5.49.

As we can see from Fig. 5.49 and Fig. 5.54, the cardinality increases inside the regions where false alarm appears. To reduce cardinality to two where it is more than two, we reduce the probability of birth. In the results given in Fig. 5.53 and Fig. 5.54, the probability of birth was selected as 0.4. We have also perform tracking for probability of birth equals to 0.25. The results are given in Fig. 5.55 and Fig. 5.56.

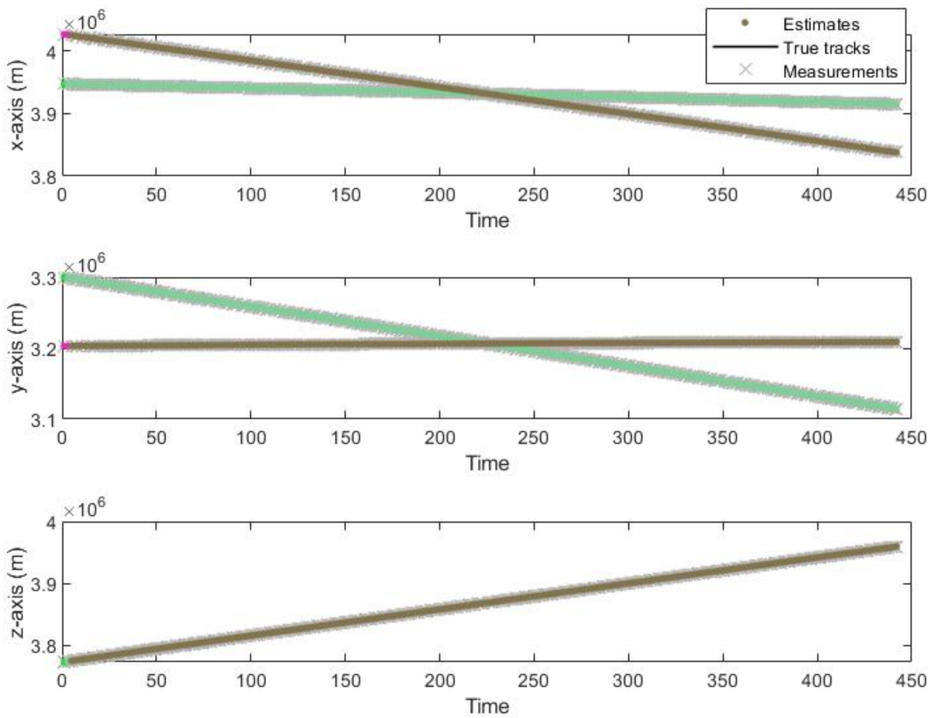

Figure 5.55: Trace of the GLMB based tracker with probability of birth set to 0.25 on the estimation points given in Fig. 5.49. Each color expresses a unique target trace.

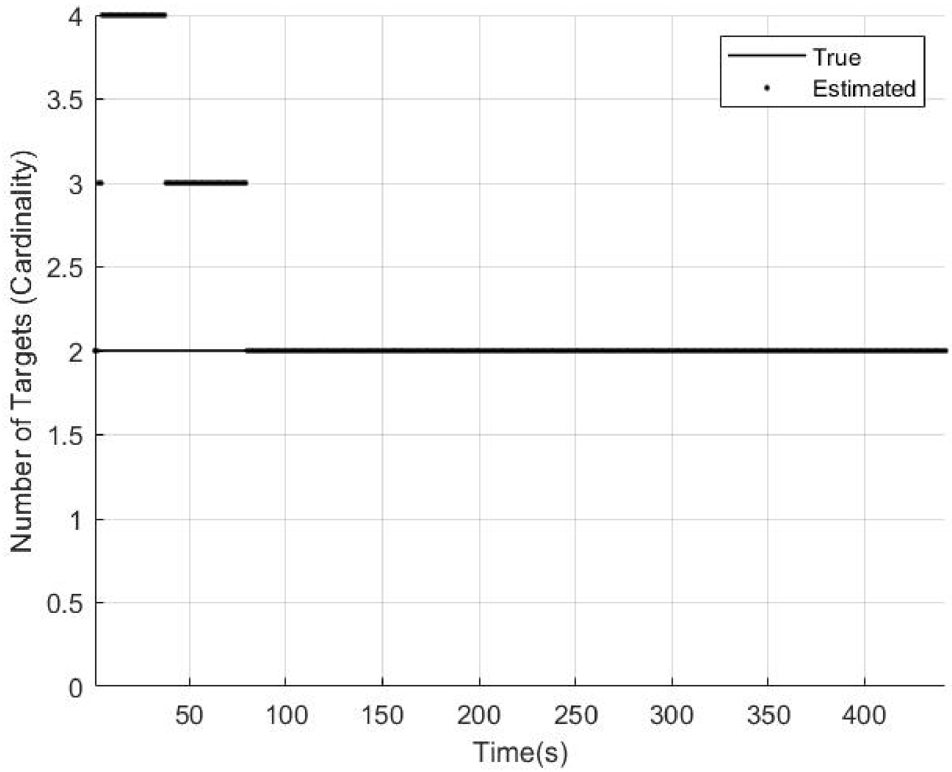

Figure 5.56: True and estimated cardinality over time of the GLMB based tracker with probability of birth set to 0.25 on the estimations given in Fig. 5.49.

The results show that false alarm can still occur. However, the results for low probability of birth can be satisfying. In addition, the results shown in Fig. 5.55 and Fig. 5.56 are comparably better than the results for standard MIMO radar whose performance is given in Fig. 5.51 and Fig. 5.52.

To summarize, the GLMB-based MIMO radar tracking system is suitable to use and performs sufficiently. The tracker performs better for EMVS-MIMO radar than for the standard MIMO radar system. Nevertheless, one should tune the system parameters adequately.

5.7 Conclusions

In this chapter, we have studied the performances of the novel techniques that are proposed in chapter 4. Examining the results, we can say that the performances of all systems are satisfying. However, we should note that the system parameters must be tuned for interested applications.

In Section 5.2, we have studied ambiguity functions and matched filter outputs of the PLFM and PPLFM waveforms. We have observed that the ambiguity function of both signals are Doppler tolerant. In addition, the Doppler cut of a PPLFM waveform has two main lobes of the signal at known points as we know the slope of the two main lines. In other words, the ambiguity function of a PPLFM waveform has two lines with known slopes. The delay and Doppler estimation performance is examined for single and multiple target case. The results are promising.

In Section 5.3, we have studied the performance of the detection algorithm using bistatic range measurements. We observe that the effect of SNR, hence RCS on detection performance is more than we expected. In the regions where the SNR is greater than 14dB for many of the bistatic pairs, false alarm rate increases and the probability of miss decreases considerably. On the other hand, probability of miss increases in the regions where adequate number of bistatic pairs has SNR more than 14dB. It was expected since the probability of detection is directly proportional to the number of measurements obtained for the target. Another factor that is affecting the probability of false alarm is the geometry. If the ellipsoids passes closer to each other, the probability of false alarm increases. As a result, the radar positions affect the detection performance considerably.

In Section 5.4, we show that the performance of the proposed position and velocity estimation is adequate to be used in real life applications. For about 85 to 95% of the time, the positioning and velocity estimation error are lower than the range and Doppler resolution. It is also shown that the positioning error can be considerably high for some test points.

In Section 5.5, we have studied the performance of the EMVS-MIMO radar for target detection. The effects of some system parameters are studied. For example, it is observed that for the case that the weight function uses bistatic range and DOA measurements equally, which means that $\psi_w = 0.5$, The system performance is in the obtimum in the context of choosing ψ_w. The results show that the detection performance of the EMVS-MIMO radar is quite better than the performance of the detection scheme that is discussed in Section 5.3.

The GLMB based tracker performance is studied in the Section 5.6. The tracking results for both conventional MIMO and EMVS-MIMO radar are promising. However, it is shown that the performance of the tracker for EMVS-MIMO radar is better. Additionally, it is shown that the effect of probability of birth on system performance is considerably high. As a result, the system can easily track both targets.

Chapter 6

Concluding Remarks and Contributions

The main goal of this thesis is to design a radar system to detect and track targets with stealth property. For that purpose, we have first study the concept of bistatic radar and its geometry in chapter 2. Additionally, we have studied a technique called ”pulse chasing” and explained its difficulties and limitation. Pulse chasing becomes almost impossible for multistatic systems with great number of transmitter and receiver. For that reason, we have turned our focus on MIMO radar systems.

In chapter 3, we have studied the difficulties and solutions to MIMO radar systems in the literature. The literature mainly focuses on Doppler-fragile waveform designs and detection systems without considering their system's high computational complexity. After finding the difficulties of MIMO radar system, we have developed some novel techniques to overcome such difficulties.

In chapter 4, we have proposed several novel techniques to be used in MIMO radar systems. First, we have proposed a method to estimate range and Doppler of several number of targets using PPLFM waveforms. The simulation results show that increasing the number of chips N will enhance the Doppler tolerance, increase the resolution, reduce the sidelobes and decrease the cross correlation for all delay and Doppler interval. Also we have discussed the benefits of using extended matched filter. Additionally, we have also studied the performance of PPLFM waveform filtering for multiple target cases and find the limitations of the system.

We have studied some alternative antennas for MIMO radar systems. One of the most promising antenna is EMVA. The EMVA provides spatial diversity. As a result, EMVA can be used to estimate DOA and polarization of the impinging wave.

Furthermore, we have also studied on MIMO radar detection and propose some novel techniques. The goal of our designs was to develop high performance and fast algorithms. To this end, we have developed three main algorithms based on different measurements.

The first one is based on bistatic range measurements. The system generates a grid of possible target points in the ROI. We proposed an exponential weight function for detection. The system performs detection by thresholding the weight values. We have also discussed ways to reduce high computational complexity. We have proposed generating the grid points for several levels. For example, we have given an two-level grid generation. First, we generate a course grid. For the points that exceed a threshold, we generate a fine grid inside of the regions around the coarse grid points that exceed the threshold.

The second algorithm depends on the bistatic range and Doppler measurements. We also define a weighting function for that case. The idea is to extend the bistatic range-based detection system to bistatic range and Doppler based detection system. For this purpose, grid is generated for both spatial and velocity domain. The weight function is extended as a function of bistatic range and Doppler dependent. However, the computational complexity increases as the problem dimension is doubled and is found unsuitable for implementation.

The last proposed detection system uses bistatic range and DOA measurements which are obtained by EMVAs. In other words, a detection algorithm for EMVS-MIMO radar is proposed. Again, the weighting function is updated and a specific grid generation algorithm is created. For each algorithm, the system performance is analyzed and the results demonstrate that the best detection algorithm is the bistatic range and DOA based algorithm.

For position and velocity estimation of a detected target, a policy-iteration-based estimation algorithm is proposed. In addition, a data association algorithm is also proposed to perform estimation with the correct measurements. We discussed how to perform data association by comparing the advantages and disadvantages of the techniques. The simulation results are promising.

Finally, we have proposed a GLMB-based MIMO radar tracking algorithm. The advantages of GLMB filters and their feasibility on MIMO radar systems are studied. We have performed detection for different cases and analyzed the performance dependencies.

To summarize, we have developed some novel techniques to be applied on MIMO radar systems with widely separated antennas. Using the proposed techniques, a complete MIMO radar system can be created.

Our future research will be focused on enhancing the proposed methods and developing new techniques and solutions for specific problems in the MIMO radar literature. From now on, we have several ideas and problem definitions to study.

The PPLFM waveform is a linear frequency modulated signal for MIMO radar usage with Doppler-tolerance property. Since there is little interest in Doppler-tolerant waveforms, we will study optimal Doppler-tolerant MIMO radar waveform design.

We will enhance the range and Doppler association using PPLFM waveforms proposed in Section 4.2. We will design our receiver to have autocorrelation at two Doppler cuts instead of one. Hence, it will be possible to associate the points with each other and eliminate ghost targets.

In the literature, EMVS-MIMO radar estimation assumes that the number of targets in the same range bin is known. To this end, we will try to design a DOA and polarization estimator, which also detects the number of targets in the same range bin.

The proposed GLMB filter-based MIMO tracker uses target position and velocity estimations as measurements. Additionally, the GLMB filter uses linear measurements. However, bistatic range, bistatic Doppler, and DOA measurements are nonlinear. Therefore, we will study the development of an extended GLMB filter for MIMO radar detection and tracking.

Bibliography

[1] E. Hanle, “Survey of bistatic and multistatic radar,” *IEE Proceedings F Communications, Radar and Signal Processing*, vol. 133, no. 7, p. 587, 1986.

[2] M. G. Parent and W. Lee, *Electromagnetic Vector Sensor (EMVS)*. No. US20170363705A1, Dec. 2017.

[3] N. J. Willis, *Bistatic radar.* Edison, NJ: SciTech Publishing, 2005.

[4] E. Daddio, A. Farina, M. Longo, and E. Conte, “Optimum and suboptimum processors for multistatic radar systems,” *1982 Selenia*, Jan. 1982.

[5] E. Conte, E. D’Addio, A. Farina, and M. Longo, “Multistatic radar detection: synthesis and comparison of optimum and suboptimum receivers,” *IEE Proceedings F - Communications, Radar and Signal Processing*, vol. 130, pp. 484–494, Oct. 1983.

[6] E. D’Addio and A. Farina, “Overview of detection theory in multistatic radar,” *IEE Proceedings F - Communications, Radar and Signal Processing*, vol. 133, pp. 613–623, Dec. 1986.

[7] A. Hassanien and S. A. Vorobyov, “Phased-MIMO Radar: A Tradeoff Between Phased-Array and MIMO Radars,” *IEEE Transactions on Signal Processing*, vol. 58, pp. 3137–3151, June 2010. Conference Name: IEEE Transactions on Signal Processing.

[8] I. Bilik, O. Bialer, S. Villeval, H. Sharifi, K. Kona, M. Pan, D. Persechini, M. Musni, and K. Geary, "Automotive MIMO radar for urban environments," in *2016 IEEE Radar Conference (RadarConf)*, pp. 1–6, May 2016. ISSN: 2375-5318.

[9] R. Boyer, "Performance Bounds and Angular Resolution Limit for the Moving Colocated MIMO Radar," *IEEE Transactions on Signal Processing*, vol. 59, pp. 1539–1552, Apr. 2011. Conference Name: IEEE Transactions on Signal Processing.

[10] P. Stoica, J. Li, and Y. Xie, "On probing signal design for mimo radar," *IEEE Transactions on Signal Processing*, vol. 55, no. 8, pp. 4151–4161, 2007.

[11] J. Li and P. Stoica, "MIMO Radar with Colocated Antennas," *IEEE Signal Processing Magazine*, vol. 24, pp. 106–114, Sept. 2007. Conference Name: IEEE Signal Processing Magazine.

[12] A. M. Haimovich, R. S. Blum, and L. J. Cimini, "MIMO Radar with Widely Separated Antennas," *IEEE Signal Processing Magazine*, vol. 25, no. 1, pp. 116–129, 2008.

[13] S. S. Chung, Y.-H. Chou, and C. Yu-Chou, "Radar Cross Section Analysis of Stealth Fighter Design," in *International journal of electrical engineering vol.23, No.6*, Nov. 2015.

[14] M. I. Skolnik, *Introduction to Radar Systems*. McGraw-Hill, 2001.

[15] V. S. Chernyak, *Fundamentals of Multisite Radar Systems : Multistatic Radars and Multistatic Radar Systems*. Routledge, May 2018.

[16] R. Viswanathan and P. K. Varshney, "Distributed detection with multiple sensors Part I. Fundamentals," *Proceedings of the IEEE*, vol. 85, pp. 54–63, Jan. 1997.

[17] R. S. Blum, S. A. Kassam, and H. V. Poor, "Distributed detection with multiple sensors II. Advanced topics," *Proceedings of the IEEE*, vol. 85, pp. 64–79, Jan. 1997.

[18] R. S. Blum, “Distributed detection for diversity reception of fading signals in noise,” *IEEE Transactions on Information Theory*, vol. 45, pp. 158–164, Jan. 1999.

[19] D. W. Bliss and K. W. Forsythe, “Multiple-input multiple-output (MIMO) radar and imaging: degrees of freedom and resolution,” in *The Thrity-Seventh Asilomar Conference on Signals, Systems Computers, 2003*, vol. 1, pp. 54–59 Vol.1, Nov. 2003.

[20] D. J. Rabideau and P. Parker, “Ubiquitous MIMO multifunction digital array radar,” in *The Thrity-Seventh Asilomar Conference on Signals, Systems Computers, 2003*, vol. 1, pp. 1057–1064 Vol.1, Nov. 2003.

[21] F. C. Robey, S. Coutts, D. Weikle, J. C. McHarg, and K. Cuomo, “MIMO radar theory and experimental results,” in *Conference Record of the Thirty-Eighth Asilomar Conference on Signals, Systems and Computers, 2004.*, vol. 1, pp. 300–304 Vol.1, Nov. 2004.

[22] I. Bekkerman and J. Tabrikian, “Target Detection and Localization Using MIMO Radars and Sonars,” *IEEE Transactions on Signal Processing*, vol. 54, pp. 3873–3883, Oct. 2006.

[23] E. Fishler, A. Haimovich, R. S. Blum, L. J. Cimini, D. Chizhik, and R. A. Valenzuela, “Spatial Diversity in Radars—Models and Detection Performance,” *IEEE Transactions on Signal Processing*, vol. 54, pp. 823–838, Mar. 2006.

[24] N. H. Lehmann, A. M. Haimovich, R. S. Blum, and L. Cimini, “High Resolution Capabilities of MIMO Radar,” in *2006 Fortieth Asilomar Conference on Signals, Systems and Computers*, pp. 25–30, Oct. 2006.

[25] H. D. Griffiths, “From a different perspective: principles, practice and potential of bistatic radar,” in *2003 Proceedings of the International Conference on Radar (IEEE Cat. No.03EX695)*, pp. 1–7, Sept. 2003.

[26] E. Grossi, M. Lops, and L. Venturino, “Robust Waveform Design for MIMO Radars,” *IEEE Transactions on Signal Processing*, vol. 59, pp. 3262–3271, July 2011. Conference Name: IEEE Transactions on Signal Processing.

[27] B. Liu, "Orthogonal Discrete Frequency-Coding Waveform Set Design with Minimized Autocorrelation Sidelobes," *IEEE Transactions on Aerospace and Electronic Systems*, vol. 45, pp. 1650–1657, Oct. 2009. Conference Name: IEEE Transactions on Aerospace and Electronic Systems.

[28] B. Liu, Z. He, and J. Li, "Mitigation of autocorrelation sidelobe peaks of orthogonal discrete frequency-coding waveform for MIMO radar," in *2008 IEEE Radar Conference*, pp. 1–6, May 2008. ISSN: 2375-5318.

[29] H. Deng, "Discrete frequency-coding waveform design for netted radar systems," *IEEE Signal Processing Letters*, vol. 11, pp. 179–182, Feb. 2004. Conference Name: IEEE Signal Processing Letters.

[30] B. Liu, Z. He, and Q. He, "Optimization of Orthogonal Discrete Frequency-Coding Waveform Based on Modified Genetic Algorithm for MIMO Radar," in *2007 International Conference on Communications, Circuits and Systems*, pp. 966–970, July 2007.

[31] Z. Cheng, B. Liao, Z. He, Y. Li, and J. Li, "Spectrally Compatible Waveform Design for MIMO Radar in the Presence of Multiple Targets," *IEEE Transactions on Signal Processing*, vol. 66, pp. 3543–3555, July 2018.

[32] H. Sun, F. Brigui, and M. Lesturgie, "Analysis and comparison of MIMO radar waveforms," in *2014 International Radar Conference*, (Lille, France), pp. 1–6, IEEE, Oct. 2014.

[33] X. Yu, G. Cui, J. Yang, L. Kong, and J. Li, "Wideband MIMO Radar Waveform Design," *IEEE Transactions on Signal Processing*, vol. 67, pp. 3487–3501, July 2019.

[34] F. A. Qazi and A. T. Fam, "Doppler detection capable good polyphase code sets based on Piecewise Linear FM," in *2014 IEEE Radar Conference*, pp. 0212–0217, May 2014. ISSN: 2375-5318.

[35] F. A. Qazi and A. T. Fam, "Doppler tolerant and detection capable polyphase code sets," *IEEE Transactions on Aerospace and Electronic Systems*, vol. 51, pp. 1123–1135, Apr. 2015. Conference Name: IEEE Transactions on Aerospace and Electronic Systems.

[36] E. Fishler, A. Haimovich, R. Blum, D. Chizhik, L. Cimini, and R. Valenzuela, "MIMO radar: an idea whose time has come," in *Proceedings of the 2004 IEEE Radar Conference (IEEE Cat. No.04CH37509)*, pp. 71–78, Apr. 2004.

[37] Q. He and R. S. Blum, "Diversity Gain for MIMO Neyman–Pearson Signal Detection," *IEEE Transactions on Signal Processing*, vol. 59, pp. 869–881, Mar. 2011.

[38] A. A. Gorji, R. Tharmarasa, and T. Kirubarajan, "Widely Separated MIMO versus Multistatic Radars for Target Localization and Tracking," *IEEE Transactions on Aerospace and Electronic Systems*, vol. 49, pp. 2179–2194, Oct. 2013.

[39] A. Noroozi, M. A. Sebt, and A. H. Oveis, "Efficient Weighted Least Squares Estimator for Moving Target Localization in Distributed MIMO Radar With Location Uncertainties," *IEEE Systems Journal*, vol. 13, pp. 4454–4463, Dec. 2019. Conference Name: IEEE Systems Journal.

[40] R. Amiri, F. Behnia, and H. Zamani, "Asymptotically Efficient Target Localization From Bistatic Range Measurements in Distributed MIMO Radars," *IEEE Signal Processing Letters*, vol. 24, pp. 299–303, Mar. 2017. Conference Name: IEEE Signal Processing Letters.

[41] R. Amiri, F. Behnia, and M. A. Maleki Sadr, "Efficient Positioning in MIMO Radars With Widely Separated Antennas," *IEEE Communications Letters*, vol. 21, pp. 1569–1572, July 2017. Conference Name: IEEE Communications Letters.

[42] Y. Du and P. Wei, "An Explicit Solution for Target Localization in Noncoherent Distributed MIMO Radar Systems," *IEEE Signal Processing Letters*, vol. 21, pp. 1093–1097, Sept. 2014. Conference Name: IEEE Signal Processing Letters.

[43] Y. Bar-Shalom, T. E. Fortmann, and P. G. Cable, "Tracking and Data Association," *The Journal of the Acoustical Society of America*, vol. 87, pp. 918–919, Feb. 1990.

[44] S. B. Popoli, *Design and Analysis of Modern Tracking Systems*. Boston: Artech House, Aug. 1999.

[45] R. P. S. Mahler, *Statistical Multisource-Multitarget Information Fusion*. USA: Artech House, Inc., 2007.

[46] R. P. S. Mahler, *Advances in Statistical Multisource-Multitarget Information Fusion*. Artech House, Aug. 2014. Google-Books-ID: zPBaBAAAQBAJ.

[47] M. Tobias and A. D. Lanterman, "Probability hypothesis density-based multitarget tracking with bistatic range and Doppler observations," *IEE Proceedings - Radar, Sonar and Navigation*, vol. 152, pp. 195–205, June 2005. Publisher: IET Digital Library.

[48] F. Papi, V. Kyovtorov, R. Giuliani, F. Oliveri, and D. Tarchi, "Bernoulli Filter for Track-Before-Detect using MIMO Radar," *IEEE Signal Processing Letters*, vol. 21, pp. 1145–1149, Sept. 2014. Conference Name: IEEE Signal Processing Letters.

[49] M. Cherniakov, ed., *Bistatic radar: principles and practice*. Southern Gate (Chichester): John Wiley & Sons, 2007. OCLC: 928663229.

[50] F. A. Qazi and A. T. Fam, "Good code sets based on Piecewise Linear FM," in *2012 IEEE Radar Conference*, pp. 0522–0527, May 2012. ISSN: 2375-5318.

[51] M. A. Richards, *Fundamentals of Radar Signal Processing*. McGraw Hill Professional, July 2005. Google-Books-ID: j91oJ22ldoQC.

[52] Q. He, N. H. Lehmann, R. S. Blum, and A. M. Haimovich, "MIMO Radar Moving Target Detection in Homogeneous Clutter," *IEEE Transactions on Aerospace and Electronic Systems*, vol. 46, pp. 1290–1301, July 2010.

[53] A. Tajer, G. H. Jajamovich, X. Wang, and G. V. Moustakides, "Optimal Joint Target Detection and Parameter Estimation by MIMO Radar," *IEEE Journal of Selected Topics in Signal Processing*, vol. 4, pp. 127–145, Feb. 2010.

[54] P. Wang, H. Li, and B. Himed, "Moving Target Detection Using Distributed MIMO Radar in Clutter With Nonhomogeneous Power," *IEEE Transactions on Signal Processing*, vol. 59, pp. 4809–4820, Oct. 2011.

[55] A. Khawar, A. Abdelhadi, and C. Clancy, "Target Detection Performance of Spectrum Sharing MIMO Radars," *IEEE Sensors Journal*, vol. 15, pp. 4928–4940, Sept. 2015.

[56] S. Maresca, A. Bogoni, and P. Ghelfi, "CFAR Detection applied to MIMO Radar in a Simulated Maritime Surveillance Scenario," in *2019 16th European Radar Conference (EuRAD)*, pp. 157–160, Oct. 2019. ISSN: null.

[57] W. Yi, T. Zhou, Y. Ai, and R. S. Blum, "Suboptimal Low Complexity Joint Multi-Target Detection and Localization for Non-Coherent MIMO Radar With Widely Separated Antennas," *IEEE Transactions on Signal Processing*, vol. 68, pp. 901–916, 2020. Conference Name: IEEE Transactions on Signal Processing.

[58] S. Fortunati, L. Sanguinetti, F. Gini, M. S. Greco, and B. Himed, "Massive MIMO Radar for Target Detection," *IEEE Transactions on Signal Processing*, vol. 68, pp. 859–871, 2020. Conference Name: IEEE Transactions on Signal Processing.

[59] Q. He, N. H. Lehmann, R. S. Blum, and A. M. Haimovich, "MIMO Radar Moving Target Detection in Homogeneous Clutter," *IEEE Transactions on Aerospace and Electronic Systems*, vol. 46, pp. 1290–1301, July 2010.

[60] A. Nehorai and E. Paldi, "Vector-sensor array processing for electromagnetic source localization," *IEEE Transactions on Signal Processing*, vol. 42, no. 2, pp. 376–398, 1994.

[61] S. Ellingson, *Electromagnetics.* VT Publishing, 1 ed., Aug. 2018.

[62] J. J. Morales and Z. M. Kassas, "Tightly Coupled Inertial Navigation System With Signals of Opportunity Aiding," *IEEE Transactions on Aerospace and Electronic Systems*, vol. 57, pp. 1930–1948, June 2021. Conference Name: IEEE Transactions on Aerospace and Electronic Systems.

[63] D. Giuli, "Polarization diversity in radars," *Proceedings of the IEEE*, vol. 74, pp. 245–269, Feb. 1986. Conference Name: Proceedings of the IEEE.

[64] D. K. Cheng, *Fundamentals of Engineering Electromagnetics*. Reading, Mass: Pearson, 1st edition ed., Nov. 2019.

[65] A. R. Relay, *The A.R.R.L. Antenna Book*. The League, 1949. Google-Books-ID: 2Y1RAAAAMAAJ.

[66] C. Gu, J. He, H. Li, and X. Zhu, "Target localization using MIMO electromagnetic vector array systems," *Signal Processing*, vol. 93, pp. 2103–2107, July 2013.

[67] "Closed-form estimation algorithm for EMVS-MIMO radar with arbitrary sensor geometry | Elsevier Enhanced Reader."

[68] F. Wen and J. Shi, "Fast direction finding for bistatic EMVS-MIMO radar without pairing," *Signal Processing*, vol. 173, p. 107512, Aug. 2020.

[69] Y. Yang, N. Ruan, G. Huang, J. Shi, and F. Wen, "A Propagator Method for Bistatic Coprime EMVS-MIMO Radar," *Mathematical Problems in Engineering*, vol. 2021, pp. 1–11, May 2021.

[70] C. Mao, J. Shi, and F. Wen, "Target Localization in Bistatic EMVS-MIMO Radar Using Tensor Subspace Method," *IEEE Access*, vol. 7, pp. 163119–163127, 2019. Conference Name: IEEE Access.

[71] C. Mao, K. Wang, J. Shi, and X. Wang, "Cramér-Rao Bounds on Angle Estimating in Bistatic MIMO Radar With Non-Orthogonal Waveforms," *IEEE Access*, vol. 8, pp. 62639–62649, 2020. Conference Name: IEEE Access.

[72] T. Liu, H. Xu, J. Shi, and F.-Q. Wen, "Fast Logistics Vehicle Localizing Based on EMVS-MIMO Radar and Edge Computing," *IEEE Access*, vol. 8, pp. 200705–200713, 2020. Conference Name: IEEE Access.

[73] K. Wong and M. Zoltowski, "Uni-vector-sensor esprit for multisource azimuth, elevation, and polarization estimation," *IEEE Transactions on Antennas and Propagation*, vol. 45, no. 10, pp. 1467–1474, 1997.

[74] G. Deschamps, "Techniques for Handling Elliptically Polarized Waves with Special Reference to Antennas: Part II - Geometrical Representation of the Polarization of a Plane Electromagnetic Wave," *Proceedings of the IRE*, vol. 39, pp. 540–544, May 1951. Conference Name: Proceedings of the IRE.

[75] R. Calderbank, S. D. Howard, and B. Moran, "Waveform Diversity in Radar Signal Processing," *IEEE Signal Processing Magazine*, vol. 26, pp. 32–41, Jan. 2009. Conference Name: IEEE Signal Processing Magazine.

[76] S. Chintagunta and P. Ponnusamy, "2D-DOD and 2D-DOA estimation using the electromagnetic vector sensors," *Signal Processing*, vol. 147, pp. 163–172, June 2018.

[77] B. Yang, P. Zhang, H. Wang, and W. Hong, "Electromagnetic Vector Antenna Array-Based Multi-Dimensional Parameter Estimation for Radio Propagation Measurement," *IEEE Wireless Communications Letters*, vol. 8, pp. 1608–1611, Dec. 2019. Conference Name: IEEE Wireless Communications Letters.

[78] B. Yang, P. Zhang, H. Wang, and W. Hong, "Efficient Delay and AoA Estimation Using Vector Antenna for Radio Propagation Measurements," in *2019 IEEE International Symposium on Antennas and Propagation and USNC-URSI Radio Science Meeting*, pp. 2125–2126, July 2019. ISSN: 1947-1491.

[79] P. Pal and P. P. Vaidyanathan, "Coprime sampling and the music algorithm," *2011 Digital Signal Processing and Signal Processing Education Meeting (DSP/SPE)*, pp. 289–294, 2011.

[80] T. Ahmed, Z. Xiaofei, and Z. Wang, "Doa estimation for coprime emvs arrays via minimum distance criterion based on parafac analysis," *IET Radar, Sonar & Navigation*, vol. 13, no. 1, pp. 65–73, 2019.

[81] X. Wang, M. Huang, and L. Wan, "Joint 2D-DOD and 2D-DOA Estimation for Coprime EMVS–MIMO Radar," *Circuits, Systems, and Signal Processing*, vol. 40, pp. 2950–2966, June 2021.

[82] M. Cherniakov and A. Moccia, eds., *Bistatic radar: emerging technology.* Chichester: Wiley, 2008. OCLC: 254483447.

[83] H. Yang and J. Chun, "An Improved Algebraic Solution for Moving Target Localization in Noncoherent MIMO Radar Systems," *IEEE Transactions on Signal Processing*, vol. 64, pp. 258–270, Jan. 2016. Conference Name: IEEE Transactions on Signal Processing.

[84] J. C. Lagarias, J. A. Reeds, M. H. Wright, and P. E. Wright, "Convergence Properties of the Nelder–Mead Simplex Method in Low Dimensions," *SIAM Journal on Optimization*, vol. 9, pp. 112–147, Jan. 1998.

[85] E. Levitin and B. Polyak, "Constrained minimization methods," *USSR Computational Mathematics and Mathematical Physics*, vol. 6, pp. 1–50, Jan. 1966.

[86] J. Hu, H. Chen, Y. Li, H. Li, and J. Xie, "Moving target parameter estimation for MIMO radar based on the improved particle filter," *Multidimensional Systems and Signal Processing*, vol. 29, pp. 1–17, Jan. 2018.

[87] H. Godrich, A. Tajer, and H. V. Poor, "Distributed target tracking in multiple widely separated radar architectures," in *2012 IEEE 7th Sensor Array and Multichannel Signal Processing Workshop (SAM)*, (Hoboken, NJ, USA), pp. 153–156, IEEE, June 2012.

[88] R. Mahler, "Multitarget Bayes filtering via first-order multitarget moments," *IEEE Transactions on Aerospace and Electronic Systems*, vol. 39, pp. 1152–1178, Oct. 2003. Conference Name: IEEE Transactions on Aerospace and Electronic Systems.

[89] R. Mahler, "PHD filters of higher order in target number," *IEEE Transactions on Aerospace and Electronic Systems*, vol. 43, pp. 1523–1543, Oct. 2007. Conference Name: IEEE Transactions on Aerospace and Electronic Systems.

[90] A.-A. Saucan, M. J. Coates, and M. Rabbat, "A Multisensor Multi-Bernoulli Filter," *IEEE Transactions on Signal Processing*, vol. 65,

pp. 5495–5509, Oct. 2017. Conference Name: IEEE Transactions on Signal Processing.

[91] B.-T. Vo and B.-N. Vo, "Labeled Random Finite Sets and Multi-Object Conjugate Priors," *IEEE Transactions on Signal Processing*, vol. 61, pp. 3460–3475, July 2013. Conference Name: IEEE Transactions on Signal Processing.

[92] B.-N. Vo, B.-T. Vo, and D. Phung, "Labeled Random Finite Sets and the Bayes Multi-Target Tracking Filter," *IEEE Transactions on Signal Processing*, vol. 62, pp. 6554–6567, Dec. 2014. Conference Name: IEEE Transactions on Signal Processing.

[93] C. Fantacci and F. Papi, "Scalable Multisensor Multitarget Tracking Using the Marginalized δ-GLMB Density," *IEEE Signal Processing Letters*, vol. 23, pp. 863–867, June 2016. Conference Name: IEEE Signal Processing Letters.

[94] J. Wang, B. Zhang, and P. Lei, "Ambiguity function analysis for OFDM radar signals," in *2016 CIE International Conference on Radar (RADAR)*, pp. 1–5, Oct. 2016.

[95] "F35 3D Models - 3D CAD Browser."

[96] A. Budiyono, "Principles of GNSS, Inertial, and Multi-sensor Integrated Navigation Systems," *Industrial Robot: An International Journal*, vol. 39, p. ir.2012.04939caa.011, Apr. 2012.

[97] J. Zhu, "Conversion of Earth-centered Earth-fixed coordinates to geodetic coordinates," *IEEE Transactions on Aerospace and Electronic Systems*, vol. 30, pp. 957–961, July 1994. Conference Name: IEEE Transactions on Aerospace and Electronic Systems.

[98] J. Sudano, "An exact conversion from an Earth-centered coordinate system to latitude, longitude and altitude," in *Proceedings of the IEEE 1997 National Aerospace and Electronics Conference. NAECON 1997*, vol. 2, pp. 646–650 vol.2, July 1997.

[99] A. Noureldin, T. B. Karamat, and J. Georgy, *Fundamentals of Inertial Navigation, Satellite-based Positioning and their Integration.* Berlin, Heidelberg: Springer Berlin Heidelberg, 2013.

[100] M. Ligas and P. Banasik, "Conversion between Cartesian and geodetic coordinates on a rotational ellipsoid by solving a system of nonlinear equations," *Geodesy and Cartography*, 2011. Publisher: Commitee on Geodesy PAS.

Appendix A

Coordinate Frames and Coordinate Conversions

In this chapter of the thesis, we make the definitions of coordinate systems used in the thesis and explain the relations and transformations between these coordinate systems. Defined coordinate systems play an essential role in explaining the geometries created by radar systems.

Before starting, let us define a point in a coordinate frame $\{m\}$

$$\boldsymbol{P}^{\{m\}} = \begin{bmatrix} x^{\{m\}} \\ y^{\{m\}} \\ z^{\{m\}} \end{bmatrix}.$$

Note that the point is defined in a 3D Cartesian frame. In the following Section, we will define some coordinate frames. After that, we will explain how a position in any frame can be converted to any other frame.

A.1 Coordinate Frames

A coordinate system is a subspace of $\mathbb{R}^N$ defined by an origin and basis vectors where N is the number of dimensions [96]. Here, we will only study on 3D space. In the following, we will define some coordinate frames that are used in this thesis.

A.1.1 Earth-Centered Earth-Fixed (ECEF) Frame

ECEF is a Cartesian-defined coordinate frame to define any position around, inside, and on the Earth. The origin is defined at the center of the Earth, and the x-axis passes through the zero latitude and the zero longitude, which is the intersection of the equator and prime meridian, y-axis through the zero latitude and 90-degree longitude, and z-axis through the north pole [97]. We will refer to the ECEF frame as {e}

A.1.2 Latitude-Longitude-Altitude (LLA) Frame

LLA is a non-linearly defined coordinate frame. It is called Latitude-Longitude-Altitude, it is a definition by latitude and longitude angles, and the altitude from the surface. There are several units that can be used. For latitude and longitude, unit of angles, radian or degree, and for altitude, unit of lengths such as meter can be used.

Note that the LLA position also related to the Earth surface model. The Earth can be modelled as a sphere or an ellipsoid. LLA coordinate system using a spherical model is called Geocentric coordinate system, which is the spherical coordinate frame version of ECEF. On the other hand, LLA coordinate frame using an ellipsoid model is defined in a different way. LLA coordinate frame on an ellipsoid World model is called geodetic frame. In geodetic frame, the latitude angle is defined at the foci point as the angle between the equator plane and the normal vector to the ground passing through the specified point [98]. Note that there are infinite number of foci points creating a circle around the origin, and the aforementioned foci point at the intersection of equator plane and normal vector to the ellipsoid.

One of the most important things to consider is the parameters of the ellipsoid model, which will be considered as the World's surface. In most of the application, WGS84 model is used since it has the most realistic constant parameters [99, 97]. The most important parameters are the semimajor, semiminor axes and eccentritricity of the World. In WGS84, the semimajor axis, semiminor axis, and the eccentricity equal to $a = 6378137m$, $b = 6356752.3142m$ and $e = \sqrt{0.00669437999}$ respectively. For the consistency of the results obtained, the WGS84 model is used in this thesis. We will refer to LLA frame as {g}, since "g" is the first letter of geodetic.

A.1.3 East-North-Up (ENU) Local Frame

ENU is a Cartesian-defined coordinate frame which is used to define a location relative to a point on Earth. ENU frame is defined by a point and the tangent plane that is parallel to the Earth's surface at that specific point. The origin is defined on a specific point. Its x, y and z axis pointing towards east, north, and up respectively. Note that the x and y axes are on (parallel to) the local tangent plane and z-axis perpendicular to the plane. For the sake of simplicity, the basis vectors will be called as $\vec{e}$, $\vec{n}$ and $\vec{u}$ referring to east north and up directions respectively

ENU frame is generally used for base devices on Earth, such as radar antennas, to define a point relative to the base point's surface. It should be noted that there are infinite number of ENU frames can be defined since it depends on the reference point. ENU frame also referred as Local-Level frame [99]. We will refer to ENU frame as {l}.

A.1.4 Azimuth-Elevation-Range (AER) Local Frame

AER is the spherical coordinate frame that is defined on ENU frame. But, the angles are defined different to the general spherical coordinate frames. Azimuth angle is defined as the clockwise angle from the North to East, and the elevation angle is defined as the angle between the surface plane and the direction vector where it increases towards the Up vector from the surface plane. Lastly, the range is simply the distance between the specified point and the origin. The geometry of ENU and AER frames is depicted in Fig. A.1.

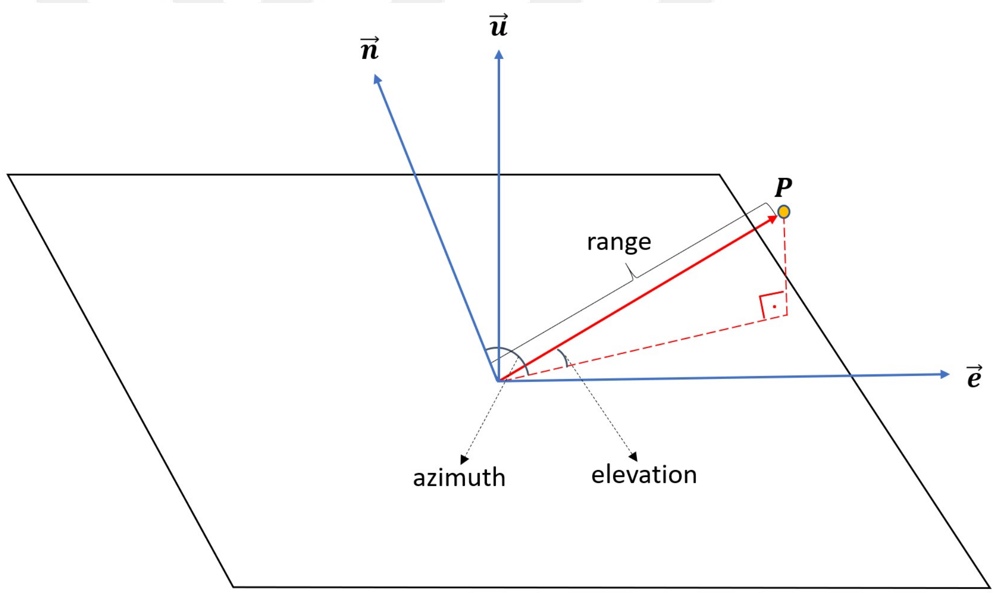

Figure A.1: The geometry of ENU and AER coordinate frames.

A.2 Conversions Between Coordinate Frames

A point $\boldsymbol{P}^{\{m\}}$ which is defined as a Cartesian coordinate in $\{n\}$-frame can be transformed into another frame in two or three steps. To transform $\boldsymbol{P}^{\{m\}}$ into another Cartesian coordinate frame $\{n\}$, the point should be rotated and moved to a point in $\{n\}$-frame since $\{m\}$ and $\{n\}$ can have different centers and different basis vectors. For non-Cartesian coordinate systems, further calculations are needed. In the light of this information, we can calculate the transformations between predefined coordinate frames.

Rotation between cartesian coordinate frames $\{m\}$ and $\{n\}$ can be performed by a matrix called "Rotation matrix":

$$\boldsymbol{P}^{\{m\}} = \mathbf{R}^{\{m\}}_{\{n\}} \boldsymbol{P}^{\{n\}},$$

where $\mathbf{R}^{\{m\}}_{\{n\}}$ is the rotation matrix from $\{n\}$ to $\{m\}$. This matrix operation is feasible since the basis vectors of both frames are orthogonal. Additionally, $\mathbf{R}^{\{n\}}_{\{m\}} = (\mathbf{R}^{\{m\}}_{\{n\}})^{-1}$ from the orthogonality property, and $(\mathbf{R}^{\{m\}}_{\{n\}})^{-1} = (\mathbf{R}^{\{m\}}_{\{n\}})^{T}$ since $\{m\}$ and $\{n\}$ are also mutually orthogonal.

A.2.1 Conversion Between ECEF and LLA

It is convenient to consider the transformation in two parts. First, we will give the conversion from LLA to ECEF frame. Then, the ways to convert ECEF to LLA will be studied and compared since its computational load is high. The geometry of ECEF and LLA frame is depicted in Fig. A.2.

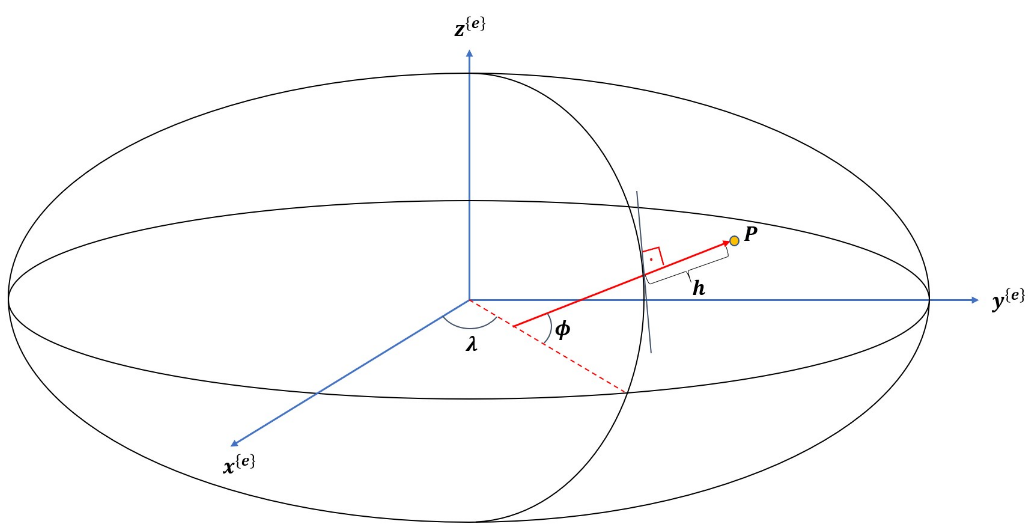

Figure A.2: The geometry of ECEF and LLA coordinate frames.

Any position in LLA frame $\boldsymbol{P}^{\{g\}} = [\phi, \lambda, h]^T$ can be converted to ECEF frame easily by given formulas [97, 98]:

$$x^{\{e\}} = (R + h)\cos\phi\cos\lambda, \tag{A.1}$$

$$y^{\{e\}} = (R + h)\cos\phi\sin\lambda, \tag{A.2}$$

$$z^{\{e\}} = (R + h - e^2 R)\sin\phi, \tag{A.3}$$

where

$$R = \frac{a}{\sqrt{1 - e^2\sin^2\phi}}.$$

To convert a position in ECEF frame to LLA frame, there are several solutions available in the literature. Some of the most attracted works are [98, 97, 100]. The main reason why this subject has been studied so much in the literature is that the transformation is not straightforward. The conversion can be performed by iterative and non-iterative way.

The calculation of longitude can be performed by using a simple equation [100]:

$$\lambda = \tan^{-1}\frac{y^{\{e\}}}{x^{\{e\}}}.$$

On the other hand, to avoid errors, a more stable version can be used:

$$\lambda = 2\tan^{-1}\frac{y^{\{e\}}}{x^{\{e\}} + \sqrt{{x^{\{e\}}}^2 + {y^{\{e\}}}^2}}. \tag{A.4}$$

To find the latitude and altitude, a number of equations must be calculated [97]:

$$
\begin{aligned}
r &= \sqrt{x^{\{e\}^2} + y^{\{e\}^2}} \\
A &= \frac{ar + (a^2 - b^2)}{b|z|} \\
B &= \frac{ar - (a^2 - b^2)}{b|z|} \\
C &= (4/3)(AB + 1) \\
Q &= 2(A^2 - B^2) \\
D &= C^3 + Q^2 \\
v &= \sqrt[3]{\sqrt{D} - Q} - \sqrt[3]{\sqrt{D} + Q} \\
G &= \frac{\sqrt{A^2 + v} + A}{2} \\
T &= \sqrt{G^2 + (B - vG)/(2G - A)} - G
\end{aligned}
$$

Using the calculated T, latitude ϕ and altitude h can be calculated:

$$\phi = \operatorname{sign}(z)\tan^{-1}\left(\frac{2aT}{b(1 - T^2)}\right) \tag{A.5}$$

$$h = (r - a)\cos\phi + (|z| - bT)|\sin\phi| \tag{A.6}$$

Note that there are more closed form solutions for transforming ECEF coordinates into LLA frame coordinates. A comparison between some of the most significant works in literature is also given in [100].

A.2.2 Conversion Between ECEF and ENU

As it is stated in previous section, ENU coordinate frame is defined by a reference point and a point of interest. The relation is depicted in Fig. A.3.

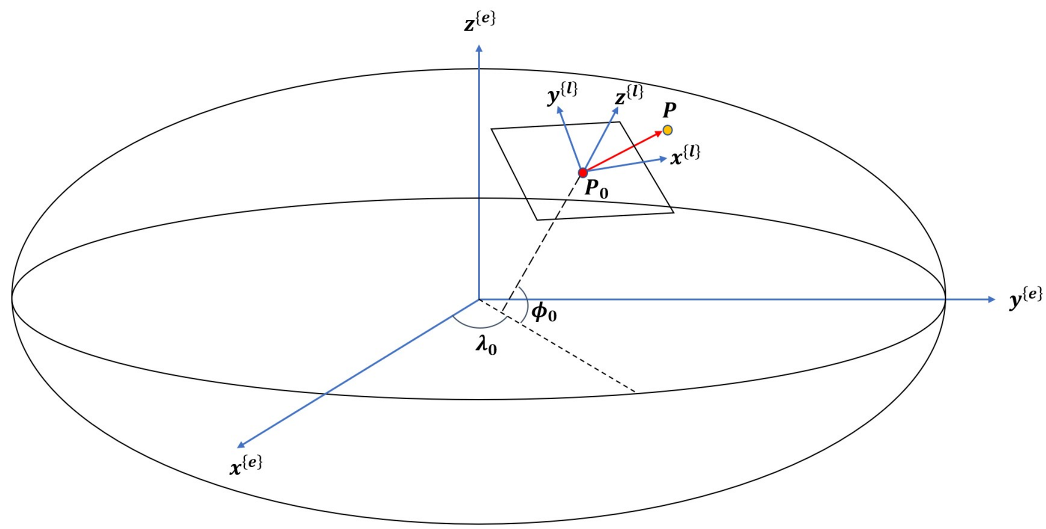

Figure A.3: The geometry of ECEF and ENU coordinate frames.

There are two main steps to perform conversion between ECEF and ENU coordinate frames. The first thing to consider is that the rotation between basis vectors of ECEF and ENU frames. The second thing is the origin point.

Let us define the reference point of the ENU frame as $\boldsymbol{P}_0^{\{e\}}$, which equals to the origin of the ENU frame, and the point of interest as $\boldsymbol{P}$ which can be any arbitrary position. Since we can convert ECEF frame into LLA frame, we can simply calculate the rotation matrix $\mathbf{R}_{\{l\}}^{\{e\}}$ by using the LLA definition of the reference point $\boldsymbol{P}_0^{\{g\}} = [\phi_0, \lambda_0, h_0]^T = \boldsymbol{P}_0^{\{e\}}$, [99]:

$$\mathbf{R}_{\{l\}}^{\{e\}} = \begin{bmatrix} -\sin\lambda_0 & -\sin\phi_0\cos\lambda_0 & \cos\phi_0\cos\lambda_0 \\ \cos\lambda_0 & -\sin\phi_0\sin\lambda_0 & \cos\phi_0\sin\lambda_0 \\ 0 & \cos\phi_0 & \sin\phi_0 \end{bmatrix}. \tag{A.7}$$

By using (A.7), a position defined in ENU frame can be converted to ECEF frame:

$$\boldsymbol{P}^{\{e\}} = \mathbf{R}_{\{l\}}^{\{e\}}\boldsymbol{P}^{\{l\}} + \boldsymbol{P}_0^{\{e\}}. \tag{A.8}$$

Note that we moved the origin from ENU reference point to center of mass of the Earth by adding the ECEF position of the center of the ENU frame $\boldsymbol{P}_0^{\{e\}}$. On the other hand, since we know that $\mathbf{R}_{\{e\}}^{\{l\}} = (\mathbf{R}_{\{l\}}^{\{e\}})^T$, we can convert a position defined in ECEF frame into ENU frame:

$$\boldsymbol{P}^{\{l\}} = (\mathbf{R}_{\{l\}}^{\{e\}})^T(\boldsymbol{P}^{\{e\}} - \boldsymbol{P}_0^{\{e\}}). \tag{A.9}$$

A.2.3 Conversion Between ENU and AER

The conversion between ENU and AER frames can be deduced by Fig. A.1. Given the position in ENU frame, $\boldsymbol{P}^{\{l\}} = \begin{bmatrix} x^{\{l\}} \\ y^{\{l\}} \\ z^{\{l\}} \end{bmatrix}$, the azimuth angle ϕ^l, elevation angle θ^l, and range r^l can be calculated by given formulas:

$$\phi^{\{l\}} = \tan^{-1}(x^{\{l\}}/y^{\{l\}}) \tag{A.10}$$

$$\theta^{\{l\}} = \tan^{-1}\left(\frac{z^{\{l\}}}{\sqrt{x^{\{l\}^2} + y^{\{l\}^2}}}\right) \tag{A.11}$$

$$r^{\{l\}} = \left\|\boldsymbol{P}^{\{l\}}\right\| \tag{A.12}$$